UNIVERSITÀ DEGLI STUDI DI TRIESTE

Sede Amministrativa del Dottorato di Ricerca

XXII CICLO DEL
DOTTORATO DI RICERCA IN
INGEGNERIA DELL'INFORMAZIONE

Multimodal functional neuroimaging: new insights from novel head modeling methodologies

Settore scientifico disciplinare: ING-INF/06 – *Bioingegneria Elettronica e Informatica*

DOTTORANDO:
Fabio MENEGHINI

RESPONSABILE DOTTORATO DI RICERCA
Chiar.mo Prof. Roberto VESCOVO

RELATORE
Dott. Ing. Federica VATTA (Università di Trieste)

CORRELATORE
Chiar.mo Prof. Francesco DI SALLE (Università di Salerno)

ANNO ACCADEMICO 2009-10

Dentro di me vivono la mia identica vita dei microrganismi che non sanno di appartenere al mio corpo... Io a quale corpo appartengo?

(Franco Battiato)

Acknowledgments

The present work, as a result of four years spent researching and investigating the physical mechanisms underlying the brain phenomena, is almost entirely based on the analysis of data acquired at the Maastricht Brain Imaging Center (M-BIC), Faculty of Psycology and Neuroscience, Department of Cognitive Neuroscience of the University of Maastricht (Maastricht, NL). This is why my first sincerest gratitude goes to the M-BIC Directors, prof. Francesco Di Salle and prof. Rainer Goebel, and to all the scientists, research and technical staff that introduced me in the latest cutting-edge advancements in data acquisition and processing technologies.

"Those were the days" so the title of an old popular song reads. This is the literal expression that usually comes in my mind whenever I recall anyone of the single day from the last four years. Four years dense of expectations, emotions, and life.

I will always be grateful to my wife for supporting me from the very first day this journey -that we call *PhD* -started from, especially for her lovable patience during my experience at the Maastricht University, where the most significant part of my studies –and one of the most exciting parts of my life-took place.

Thanks to Tommaso, Matteo e Michele, for being there sharing their thoughts, their life with mine, always making me feel at the right moment in the right place, even (and especially) when everything seemed to go wrong. Thanks al-

so to Barbara, Claudia and Rosy, because in many of the funniest moments I will ever remember there are their beautiful smiles.

Eventually my special thanks go to prof. Francesco Di Salle and Federica Vatta, who always believed in me from the very first moment, because without their wise support nothing of this would have ever happened.

Last, but not least, thanks to my sons, just for coming into existence, thus making our lives brighter and worthier day by day.

List of contents

List of abbreviations

CNS: Central Nervous System
PET: Positron Emission Tomography
fMRI: Functional Magnetic Resonance Imaging
DWI: Diffusion Weighted Imaging
DTI: Diffusion Tensor Imaging
MRI: Magnetic Resonance Imaging
EEG: ElectroEncephaloGraphy
MEG: MagnetoEncephaloGraphy
ECD: Equivalent Current Dipole
DECD: Distributed Equivalent Current Dipole
HCM: Head Conductor Model
FDM: Finite Difference Method
BEM: Boundary Elements Method
FEM: Finite Element Method
WMN: Weighted Minimum Norm
PSF: Point Spread Function
dSPM: Dynamic Statistical Parametric Maps
BOLD: Blood Oxygen Level Dependent (signal)
VBM: Voxel-based Morphometry
TBSS: Tract based Spatial Statistics
GLM: General Linear Model

1 Introduction

1.1 Motivation of the study

Localization of neural brain sources is important in several areas of research of basic neuroscience, such as cortical organization and integration, and in some areas of clinical neuroscience such as preoperative planning [1] and epilepsy [2].

Neuroimaging techniques, aimed to the visualization of the cerebral activity, can be grouped into two main categories: those based on the variation of hemodynamic parameters, such as blood flux, volume, oxygen and or glucose consumption, that are implicitly related to the neural activity, and those based on direct measurement of the neuronal bioelectricity.

The former includes techniques such as Positron Emission Tomography (PET) and Functional Magnetic Resonance Imaging (fMRI) which, thanks to its non-invasiveness, it results the most widely used in neuroimaging. The fMRI exhibits a high spatial resolution, in the order of 2-4 mm, but temporal resolution is limited by the typical hemodynamic response timings, which are about 1-2 seconds, far from being able to track neuronal events, as they occur in few milliseconds.

Techniques based on the direct measurements of the bioelectric activity include ElectroEncephaloGraphy (EEG) and MagnetoEncephaloGraphy (MEG), followed by three dimensional source reconstruction algorithms. Although EEG and MEG can offer a very high temporal resolution on the order of fraction of milliseconds, still the spatial resolution reached by the reconstruction algorithms is severely limited by the intrinsic uncertainty margins. Focal sources can be affordably detected and described from EEG and MEG data by means of dipolar localization techniques, while non-linear methods for parametric modelling must be used to describe distributed activity.

Both the approaches imply the definition of models of neuronal source, usually described as a patch of Equivalent Current Dipole (ECD), as well as the definition of a volume conductor model, which can be realistic or approximated.

The two kinds of approaches thus have complementary features in terms of spatio-temporal resolution, from here the idea to combine the two data analysis in the so-called *multimodal integration.* Thanks to these advanced analysis methods, it is now possible to derive 4-D cerebral maps of neural activation-deactivation patterns, that exhaustively describe cerebral activities arising from a specific task execution, starting from simple motor tasks to more complex cognitive and behavioural processes. In this perspective, EEG was preferred instead of MEG because of the possibility to acquire EEG and fMRI data simultaneously [3]. Up to now, EEG-fMRI has been mainly seen as an fMRI technique in which the synchronously acquired EEG is used to characterize brain activity across time allowing to map, through statistical parametric mapping for example, the associated hemodynamic changes [4]. Outside the field of epilepsy, EEG-fMRI has been used to study event-related (triggered by external stimuli) brain responses and provided important new insights into baseline brain activity in during resting wakefulness and sleep [5]

Nonetheless, it must be taken into account that different cerebral regions supposed to run different tasks can be no longer considered as independent, but rather as a synchronized team cooperating to successfully execute each task. This leads to the importance of studying the organized behaviour among the specific cerebral regions basing on their functional connectivity.

The present dissertation is aimed to introduce a novel approach to the multimodal functional imaging of neural sources of activity, by means of integration of MRI, EEG and fMRI data analysis.

1.2 Overview

The present dissertation begins with a review of the current state-of-the-art in the major neuroimaging techniques. Particular attention has been devoted to EEG modelling since it represents the main player of our studies, also because it is one of the most promising techniques in neural sources analysis.
The literature regarding EEG/fMRI multimodal integration is quite extensive even if it comes as a very recent approach; a summary of the main and commonly used algorithm is presented.
Moreover a brief overview of Diffusion Weighted Imaging and Diffusion Tensor Imaging is also given, as their application in modelling refinement is enormously increasing the accuracy and the complexity of the models.
In chapter 3 we will discuss the accomplished comparative analysis, which required the introduction of some kind of measurements in order to address the target.
Chapter 4 deals with a case study and the proposal of an EEG and fMRI data processing pipeline that leads to a robust and effective neural source reconstruction.

The results presented in chapter 3 have been first published in [6], and later in [7] where a further algorithm has been involved in a deeper investigation about how different numeric techniques perform in the EEG forward problem solution.
The experiments described in chapter 4 as well as the presented results suggest further investigations, mainly focused on the optimal tuning of the many parameters involved in the source imaging application described. However, due to their relevance, they will be soon submitted for a methodology study to *Neuroimage* journal.

Besides, two more papers had been previously published, focusing on the implementation, validation [8] and application [9] of the algorithm described in section 2.2.3.3, in a High Performance Computing environment.

2 *State of the art in functional neuroimaging*

In this section a synthetic overview of the currently most widely used techniques in functional neuroimaging is presented.

Magnetoencephalography (MEG) and Electroencephalography (EEG) provide a unique window on the human brain. Both modalities measure the electromagnetic signals produced by electrical activity in the brain. It is widely believed that the primary source of these signals is current flow in the apical dendrites of pyramidal cells in the cerebral cortex. Coherent activation of a large number of pyramidal cells small areas of cortex can be modelled as an equivalent current dipole (ECD), which, because of the columnar organization of cortex, is oriented normally to its surface. The current dipole is therefore the basic element used to represent neural activation in EEG and MEG based inverse methods, and these dipoles are often constrained to lie within cortical gray matter.

Current technologies provide EEG acquisition systems fully compatible with the conventional MRI environment, i.e. high static magnetic field and strong RF electromagnetic pulses gradients.

As these new features make possible the contemporary measurements of both hemodynamic response and neuronal electrical activity, we are focusing on EEG, rather than MEG signal processing to accomplish an effective multimodal integration, which will be described in the last paragraph of this chapter.

2.1 Diffusion Weighted Imaging

Diffusion-weighted magnetic resonance imaging (MRI) is an emerging neuroimaging technique which has been boosted by established successes in clinical neurodiagnostics and by powerful new applications for studying the brain in vivo.

Measurement of signal attenuation from water diffusion is one of the most important issues for operating diagnosis in the central nervous system (CNS). In particular, diffusion tensor imaging (DTI) may be used to map and characterize the three-dimensional diffusion of water as a function of spatial location. The diffusion tensor thus obtained describes the magnitude, the degree of anisotropy, and the orientation of diffusion anisotropy.

Many developmental, aging, and pathologic processes of the CNS influence the microstructural composition and architecture of the affected tissues. In the above cited conditions, the diffusion of water within tissues results to be altered by changes in the tissue microstructure and organization; consequently, diffusion-weighted (DW) MRI methods, including DTI, are extremely powerful probes for characterizing the effects of disease and aging on microstructure.

2.1.1 Physiological diffusion

Diffusion is a random transport phenomenon, which describes the transfer of material from one spatial location to other locations over time. In three dimensions, the Einstein diffusion equation is:

$$D = \frac{< \Delta r^2 >}{2n\Delta t}$$

where the diffusion coefficient D (in mm^2/s) is proportional to the mean squared displacement $<\Delta r^2>$ divided by the number of dimensions, n , and the diffusion time, t. The diffusion coefficient of water at 37°C is roughly 3.0x10^{-9} mm^2/s and increases at higher temperatures. In absence of boundaries, molecular water displacement is described by a Gaussian probability density:

$$P(\Delta r, \Delta t) = \frac{1}{\sqrt{(2\pi D\Delta t)^3}} \exp\left(\frac{-\Delta r^2}{4D\Delta t}\right)$$

The spread in this distribution increases with the diffusion time, t. The diffusion of water in biological tissues occurs through cellular structures. Water diffusion is primarily caused by random thermal fluctuations. The behaviour is further modulated by the interactions with cellular membranes, and subcellular and organelles. Cellular membranes hinder the diffusion of water, causing water to take more tortuous paths, thereby decreasing the mean squared displacement. In fibrous tissues, including white matter, water diffusion is relatively unimpeded in the direction parallel to the fibres orientation. Conversely, water diffusion is highly restricted and hindered in directions perpendicular to the fibres. Thus, the diffusion in fibrous tissues is anisotropic. The application of the diffusion tensor to describe anisotropic diffusion behaviour was introduced by Basser [10], [11]. In this model, diffusion is described by a multivariate normal distribution:

$$P(\Delta\vec{r}, \Delta\vec{t}) = \frac{1}{\sqrt{(2\pi\Delta t)^3 |D|}} \exp\left(\frac{-\Delta\vec{r}^{\,T} D^{-1} \Delta\vec{r}}{4\Delta t}\right)$$

where the diffusion tensor D is a 3x3 covariance matrix:

$$D = \begin{bmatrix} D_{xx} & D_{xy} & D_{xz} \\ D_{yx} & D_{yy} & D_{yz} \\ D_{zx} & D_{zy} & D_{zz} \end{bmatrix}$$

which describes the covariance of diffusion displacements in three dimensions normalized by the diffusion time. The diagonal elements (D_{ii}>0) are the diffusion variances along the axes x ,y , and z, and the off-diagonal elements are the covariance terms and are symmetric about the diagonal ($D_{ij}=D_{ji}$). Diagonalization of the diffusion tensor yields the eigenvalues ($\lambda_1,\lambda_2,\lambda_3$) and corresponding eigenvectors ($\mathbf{e}_1,\mathbf{e}_2,\mathbf{e}_3$) of the diffusion tensor, which describe the directions and apparent diffusivities along the axes of principal diffusion.

Moreover, a tensor represents a physical state and it is a geometric object that has invariant properties when the coordinate system is rotated. A scalar for instance does not change with the rotation, a vector can be represent as an arrow in space with direction and magnitude and even if the components might change during rotation of coordinate system the direction and magnitude are invariant. As a consequence, the complete set of tensor's element can be computed by

$$D = \boldsymbol{S}\begin{bmatrix}\lambda_1 & 0 & 0\\ 0 & \lambda_2 & 0\\ 0 & 0 & \lambda_3\end{bmatrix}\boldsymbol{S}^{-1}$$

where S is orthogonal matrix of unit length eigenvectors of the measured diffusion tensor.

The diffusion tensor may be visualized as an ellipsoid, with the eigenvectors defining the directions of the principal axes and the ellipsoidal radii defined by the eigenvalues (Figure 2-1). Diffusion is considered isotropic when the eigenvalues are nearly equal ($\lambda_1\sim\lambda_2\sim\lambda_3$). Conversely, the diffusion tensor is anisotropic when the eigenvalues are significantly different in magnitude ($\lambda_1>\lambda_2>\lambda_3$). The eigenvalue magnitudes may be affected by changes in local tissue microstructure with many types of tissue injury, disease, or normal physiological changes. Thus, the diffusion tensor is a sensitive probe for characterizing both normal and abnormal tissue microstructure.

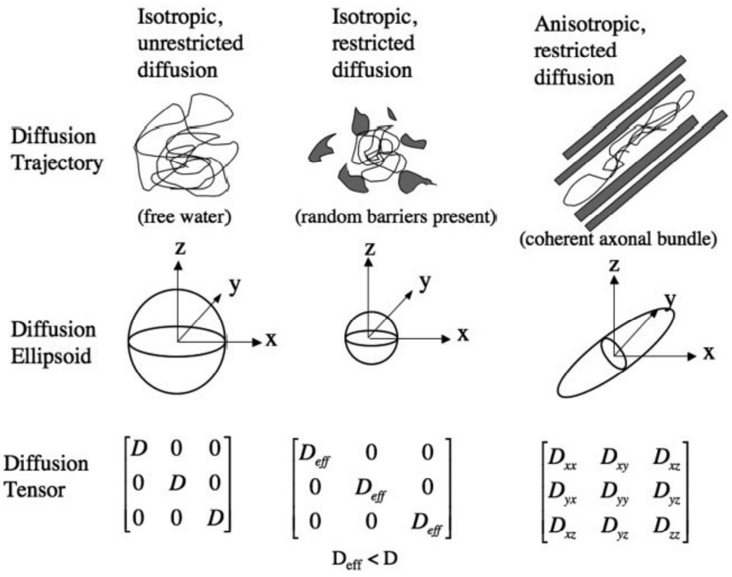

*Figure 2-1*The diffusion ellipsoids and tensors for isotropic unrestricted diffusion, isotropic restricted diffusion, and anisotropic restricted diffusion are shown.

In the CNS, water diffusion is usually more anisotropic in white matter regions and isotropic in both grey matter and cerebrospinal fluid (CSF). The major diffusion eigenvector ($\mathbf{e}_1$, direction of greatest diffusivity) is assumed to be parallel to the tract orientation in regions of homogeneous white matter. This directional relationship is the basis for estimating the trajectories of white matter pathways with tractography algorithms.

The diffusion tensor model performs well in regions where there is only one fibres population (fibres are aligned along a single axis), where it gives a good depiction of the fibres orientation. However, it fails in regions with several fibres populations aligned along intersecting axes because it cannot be used to map several diffusion maxima at the same time. In such areas, imaging techniques that provide higher angular resolution are needed.

2.1.2 Diffusion Tensor Imaging

Maps of DTI measures are estimated from the raw DW images. The first step in the calculation of the diffusivities tensor is to estimate the apparent diffusivity maps, $D_{i,app}$, for each encoding direction. The following equation describes the signal attenuation for anisotropic diffusion with the diffusion tensor:

$$S_i = S_0 \exp\left(-b\hat{g}_i^T D\hat{g}_i\right) = S_0 \exp\left(-b_i D_{i,app}\right)$$

where S_i is the DW signal, the index *i* corresponds to a unique encoding direction, is the unit vector describing the DW encoding direction, and b_i is the amount of diffusion weighting. In the case of single diffusion weighting (b - value) and an image with very little or no diffusion weighting (S_0), the apparent diffusivity maps are estimated via:

$$D_{i,app} = \frac{\ln(S_i) - \ln(S_0)}{b_i}$$

Subsequently, the six independent elements of the diffusion tensor (D_{xx}, D_{yy}, D_{zz}, $D_{xy}=D_{yx}$, $D_{xz}=D_{zx}$, and $D_{yz}=D_{zy}$) may be estimated from the apparent diffusivities using multiple linear least squares methods [11], [12] or nonlinear modelling [13].

The display, meaningful measurement, and interpretation of 3D image data with a 3x3 diffusion matrix at each voxel is a challenging or impossible task without simplification of the data. Consequently, it is desirable to distil the image information into simpler scalar maps. The two most common measures are the trace and anisotropy of the diffusion tensor. The trace of the tensor, or sum of the diagonal elements of D, is a measure of the magnitude of diffusion and is rotationally invariant. The MD (also called the apparent diffusion coefficient, or ADC) has been used in many published studies and is simply the trace divided by 3 (MD=Tr/3), which is equivalent to the average of the eigenvalues. The degree to which the diffusivities are a function of the DW encoding direction is represented by measures of diffusion anisotropy. Many measures of anisotropy have been described, most of which are rotationally invariant. Currently, the most widely used invariant measure of anisotropy is the fractional anisotropy (FA) described originally by Basser and Pierpaoli [13]:

$$FA = \sqrt{\frac{3}{2}}\sqrt{\frac{(\lambda_1 - MD)^2 + (\lambda_2 - MD)^2 + (\lambda_3 - MD)^2}{(\lambda_1^2 + \lambda_2^2 + \lambda_3^2)}}$$

Note that the FA does not describe the full tensor shape or distribution. This is because different eigenvalues combinations can generate the same values of FA [14]. Although FA is likely to be adequate for many applications and appears to be quite sensitive to a broad spectrum of pathological conditions, the full tensor shape cannot be simply described using a single scalar measure [14]. The tensor shape can, however, be described completely using a combination of spherical, linear, and planar shape measures [14], [15].

In general, it is important to consider alternative quantitative methods when trying to interpret DTI measurements. Another important measure is the tensor orientation described by the major eigenvector direction. For diffusion tensors with high anisotropy, the major eigenvector direction is generally assumed to be parallel to the direction of white matter tract, which is often represented using a red–green–blue (RGB) color map to indicate the eigenvector orientations [16], [17].

The local eigenvector orientations can be used to identify and parcellate specific WM tracts; thus, DT-MRI has an excellent potential for applications that require high anatomical specificity. The ability to identify specific white matter tracts on the eigenvector color maps has proven useful for mapping white matter anatomy relative to lesions for preoperative planning [18] and postoperative follow-up [19].

Maps of the MD, FA, major eigenvector direction, and eigenvalues are shown as examples in Figure 2-2.

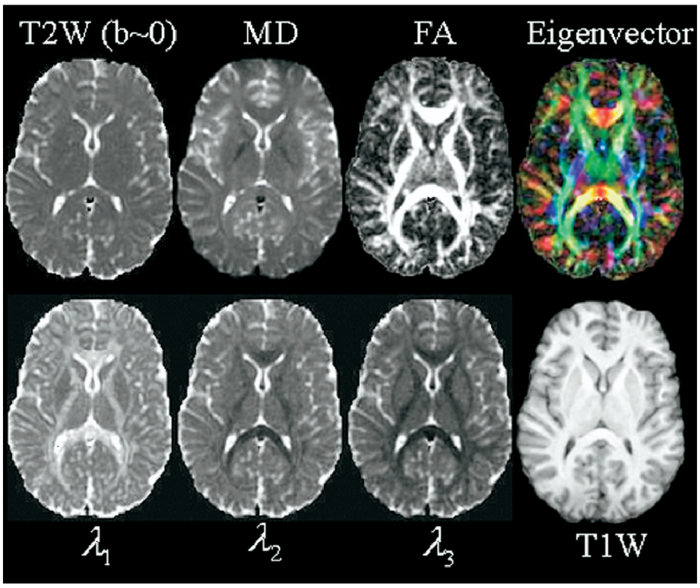

Figure 2-2 Quantitative maps from a diffusion tensor imaging (DTI) experiment

2.2 EEG-based source imaging

EEG data are measurements of potential differences on the scalp resulting from ohmic currents induced by electrical brain activity. Instrumentation for EEG consists of a set of scalp electrodes coupled to high-impedance amplifiers and a digital data acquisition system.

In EEG a detailed reconstruction of the electrical sources in the brain is usually performed by solving the so-called EEG inverse problem, the purpose of which is to find the locations and distributions of the neural sources responsible for the measured activity. Any possible model formulation of the inverse problem relies on an available solution for the companion forward problem. A forward model defines how the surface potentials at given positions on the scalp can be predicted by known sources inside the cranium, typically on the cortex surface. Running the forward problem iteratively, it is possible to solve the inverse problem by searching for the particular bioelectric source that best fits the potential distribution measured at the scalp electrodes. As an alternative, distributed source localization approaches based on imaging (e.g., minimum norm) or beamformer inverse solution [20] are also able to recover extended sources of activated cortex with different spatial extent.

Before getting into the details of the EEG source analysis, it's convenient to take a brief introduction at what the neural sources actually are, as in the following paragraph.

2.2.1 Basics of neurophysiology

The human brain is the most important organ in the central nervous system. In the brain, different regions can be designated according to their motor or higher cognitive function. For example, a specific region in the brain is responsible for hand movement, while another region processes the information concerning language. The main task of the brain is the processing and communication of information. This information can be sent to or received from parts of the human body or other designated regions of the human brain. The brain is situated inside the skull and scalp, which act as a protective layer against shock and impact. Moreover, it floats in the ventricular system which is drained with the cerebro-spinal fluid (CSF). The CSF provides essential substances for the metabolism of the brain and some protection to shock.

Concerning tissue types, the actual brain tissues can be divided in three parts: white matter, gray matter and the ventricles. The white matter mainly consists of connections from and to different parts of the gray matter. An important connection contained in the white matter is the *corpus callosum* which connects the right and left hemisphere.

The actual brain activity is generated in the gray matter. The gray matter at the edge of the brain has a folded structure to increase the surface so complex connections can be made. The outer layer is also called the *cortex* or *cortical* *gray matter* (GM). In the GM many structures can be identified according to their function in the processing of information. In the gray matter nerve cells are the generators of the electro-chemical activity.

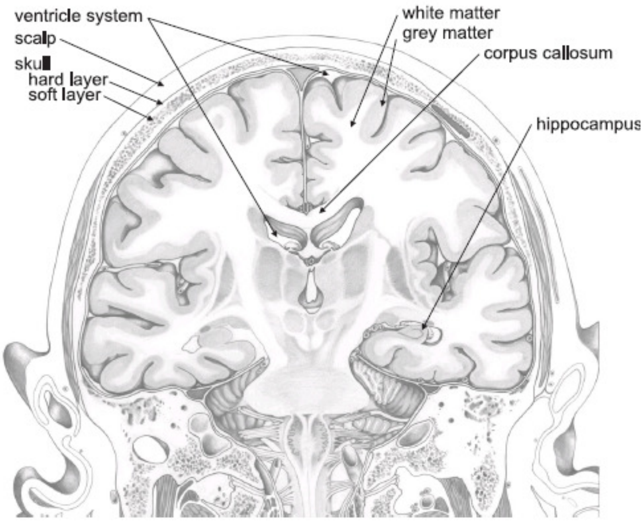

Figure 2-3 Coronal slice view of the main tissues composing the head volume

Neurons or nerve cells are the building blocks of the human central nervous system. The brain consists of about 10^{10} nerve cells or neurons. The neuron's task is to process signals coming from other neurons and transmit signals to other neurons or tissue (muscle or organs). The shape and size of the neurons vary but all neurons exhibits the same anatomical subdivision in three parts: the dendrites, the cell body or soma and the axon. The dendrites, originating from the soma and repeatedly branching, are specialized in receiving inputs from other nerve cells. The soma or cell body contains the nucleus of the cell and processes the incoming signals and decides if a signal has to be transmitted to the axon. In that case the neuron fires and an action potential is generated which propagates through the axon. Via the axon, impulses are sent to other neurons or tissue (muscles or organs). The axon's end is divided into branches which connect to other neurons or tissues. An axon can only transmit a signal to another neuron via the dendrites. Therefore, a physiological connection has to be made. This is called a synapse. The larger the dendrites, the more connections from other neurons can be made.

The synapse is a specialized interface between two nerve cells. The synapse consists of a cleft between a presynaptic and postsynaptic neuron. At the end of the branches originating from the axon, the presynaptic neuron contains small rounded swellings which contain the neurotransmitter substance.

2.2.1.1 Physiology of the neuron

At rest the intracellular environment of a neuron is negatively polarized at approximately -70 mV compared with the extracellular environment. A neuron can depolarize or hyperpolarize. A *depolarization* means that the potential difference between the intra- and extracellular environment increases. Instead of −70mV the potential difference becomes −40mV. A *hyperpolarisation* means that the potential difference between intra- and extracellular environment decreases.

After a depolarization or hyperpolarisation occurred, the neuron returns to the resting state. This is called a repolarisation and takes some time. This is called the refractory period and the neuron cannot fire an action potential during this period. The potential difference at rest is due to an unequal distribution of Na+, K+and Cl−-ions across the cell membrane. This unequal distribution is actively maintained by the Na+and K+-ion pumps located in the cell membrane, providing a dynamic equilibrium.

The processing and the transmission of the signals are done by an alternating chain of electrical and chemical reactions. Neurons activated by an action potential will secrete a chemical substance called a neurotransmitter, at the synaptic side. The secretion of neurotransmitter at the presynaptic neuron (the neuron at the axon side) is generated by action potentials. A postsynaptic neuron (the neuron at the dendrite side) has a large number of receptors on its membrane that are sensitive for this neurotransmitter. The neurotransmitter in contact with the receptors changes the permeability of the membrane for charged ions.

Two kinds of neurotransmitters exist. On the one hand there is a neurotransmitter which lets signals proliferate. These molecules cause an influx of positive ions. Hence depolarization of the intracellular space takes place. This depolarization is also called an excitatory postsynaptic potential (EPSP). On the other hand there are neurotransmitters that stop the proliferation of signals. These molecules will cause an outflow of positive ions.

Hence a hyperpolarisation can be detected in the intracellular volume. This potential change is also called an inhibitory postsynaptic potential (IPSP). There are a large number of synapses from different presynaptic neurons in contact with one postsynaptic neuron. At the cell body all the EPSP and IPSP signals are integrated. When a net depolarization of the intracellular compartment at the cell body reaches a certain threshold, an action potential is generated. An action potential then propagates along the axon to other neurons.

2.2.1.2 Generation of EEG signal

The electrodes used in scalp EEG are large and are attached to the scalp, which is distant from the neurons compared to the size of the neuron. Consequently, an electrode only detects summed activities of a large number of neurons which are synchronously electrically active. The action potentials can be large in amplitude (70-110 mV) but they have a small time course (0.3 ms). A synchronous firing of action potentials of neighbour's neurons is statistically unlikely. The postsynaptic potentials are the generators of the extracellular potential field which can be recorded with an EEG. Their time course is larger (10-20 ms). This enables the detection and measurements of summed activity of neighbour's neurons, but their amplitude is smaller (0.1-10 mV).

Apart from having more or less synchronous activity, the neurons need to be regularly arranged to result in a measurable scalp EEG signal. The spatial properties of the neurons must be so that they amplify each other's extracellular potential fields. Pyramidal neuron cells are a special type of neuron which consists of a large dendrite branch (so-called apical dendrite) which is oriented orthogonally to the surface of the gray matter. Neighbouring pyramidal cells are organized so that the axes of their dendrite tree are parallel with each other and normal to the cortical surface. Hence, these cells are suggested to be the main generators of the EEG.

The following is focused on excitatory synapses and EPSP, located at the apical dendrites of a pyramidal cell. An analogue reasoning can be made for IPSPs. As mentioned before, at the resting state there is a potential difference between the inside and outside of the cell. The incoming action potential releases the neurotransmitters in the cleft, which cause an influx of positive ions at the post synaptic membrane and depolarize the local cell membrane.

Positive ions will enter the cell. This causes a lack of extracellular positive ions at the apical dendrites of the post synaptic neuron. A redistribution of positively charged ions also takes place at the intracellular side.

These ions flow from the apical dendrite to the cell body and depolarize the membrane potentials at the cell body. Subsequently positively charged ions become available at the extracellular side at the cell body and basal dendrites. The neuron is thus an element that withdraws current from the extracellular space (a so-called current sink) and that injects a current with the same intensity (current source). The electrical activity can be modelled as a current dipole. The current flow causes an electric field and also a potential field inside the human head, which extends to the scalp.

One neuron generates a small amount of electrical activity in the order of femto-Ampere. This small amount cannot be picked up by surface electrodes, as it is overwhelmed by other electrical activity from neighbouring neuron groups. When a large group of neurons (approximately 1000) is simultaneously active, the electrical activity is large enough to be picked up by the electrodes at the surface, thus generating a meaningful EEG signal.

Moreover, in order to produce a detectable signal the dipoles corresponding to each of the neurons should be oriented in the same direction. The superposition of all these dipoles creates a sufficiently strong potential field that is sensed by the surface electrodes. A large group of electrically active pyramidal cells in a small patch of cortex can be represented as one equivalent dipole on macroscopic level [21]. It is very difficult to estimate the extent of the active area of the cortex as the potential distribution on the scalp is almost identical to that of an equivalent dipole [22].

2.2.1.3 Anisotropy characterization

Electrical conductivity is the ability of a material to conduct electric current. Tissues can have either isotropic or anisotropic conductivity.

Anisotropy is the property for which a physical characteristic varies along different directions, thus in an anisotropic material the value of physical measurement made in one direction generally differs from measurement done in other directions.

The human head is composed of several layers each with different conductivity properties. Typical layers that are considered for modelling purpose are the scalp, the skull, the cerebrospinal fluid, the gray and the white matter.

Several studies have been carried out about the direction-dependent conductivity of some areas within the human head. Tissues such as skeletal muscles or white matter have been verified to have extremely anisotropic structure which can involve highly anisotropic conductivity values. The anisotropy of some layer was proved to be able to influence the EEG forward problem solution [23], [24], [25]. Therefore for an accurate formulation of the problem it should not be neglected.

Tissues significantly interested by anisotropy are the skull and the white matter. The skull is a bony structure which provides a general framework for the head. It protects the brain from injury and supports the structures of the face. Human skull is normally made up of 28 bones, all of which, except for the mandible are joined together by sutures, rigid articulations permitting very little movement. The human skull can be modelled as a three layered structure consisting of a soft bone layer spongiosa, enclosed by two hard bone layers compacta.

The compact bone is characterized by a lower conductivity than the spongy bone, this causing a direction-dependent conductivity with anisotropy ratio commonly estimated 1:10, (radial/tangential) to the skull surface [26], see Figure 2-4 where σ_r and σ_t represent the radial (longitudinal) and tangential (transversal) conductivity respectively.

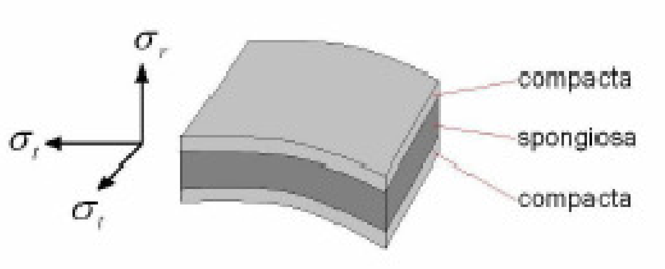

Figure 2-4 Schematic representation of the layer structure of the skull bones

The white matter is one of the main solid components of the central nervous system. It forms the bulk of the deep parts of the brain and the superficial parts of the spinal cord. Aggregates of grey matter are spread within the cerebral white matter.

White matter is composed of axons, grouped in bundles. Axons connect various grey matter areas of the brain to each other and carry nerve impulses between neurons. Nicholson made one of the early in vitro measurements proving that the white matter of a cat has bigger conductivity parallel to the fibres than normal to the fibres. In this measurement the conductivity along nerve bundle resulted to be about 9 times larger than perpendicular to it [27]

A more detailed and accurate measure of anisotropy has been achieved by means of diffusion weighted imaging (DWI) and diffusion tensor image (DTI) from magnetic resonance imaging (MRI).

In their random diffusion displacements, molecules probe the structure of a tissue at a microscopic level. Molecules of water have been largely used for the investigation.

During the diffusion they cross, bounce and interact with other molecules. The effect detected by a diffusion MRI provides unique information about the structure and the geometric organization of tissues. Since the diffusion is a three dimensional process and the mobility in tissues may not be the same in all direction a DTI supplies a powerful tool for anisotropy estimation [28].

The conductivity tensor can be derived directly from the water diffusion tensor under the assumption that they share the same eigenvectors as members of the general transport tensor [10].

Lately, a strong effort to the white matter fibre's anisotropy analysis came from the usage of cutting edge methodologies such as Q-ball imaging [29] and High Angular Resolution Diffusion Imaging (HARDI), which takes advantage from high angular DWI acquisition to sensibly improve the accuracy in anisotropy description. As a result, this technique leads to diffusion representation by means of several tensors per voxel, thus allowing detecting fibre crossing and fibre kissing; an interesting application of this whole methodology has been recently studied in [30].

2.2.2 EEG forward problem

A forward model implies considering one or more current dipole inside the head and computing the electrical potentials generated at the electrode sites on the scalp surface. The relationship between the electric potentials, at any position, and a generic current density distribution in a linear, time-invariant conducting volume is described by Poisson's equation.

To derive its formulation, let us start from considering the electromagnetic fields in media or in vacuum, described by the Maxwell equations:

$$\nabla \cdot \vec{E} = \frac{\rho}{\varepsilon_0} \tag{2.1}$$

$$\nabla \times \vec{B} - \mu_0 \varepsilon_0 \frac{\partial \vec{E}}{\partial t} = \mu_0 \vec{J} \tag{2.2}$$

$$\nabla \times \vec{E} + \frac{\partial \vec{B}}{\partial t} = 0 \tag{2.3}$$

$$\nabla \cdot \vec{B} = 0 \tag{2.4}$$

where E and B are the electric and magnetic field, respectively. ε_0 and μ_0 are the permeability and susceptibility of vacuum, respectively, which can be relate to the speed of light $c = 1/\sqrt{(\mu_0 \varepsilon_0)}$, ρ is the charge density, which is the amount of charge in a volume G (unit C/m3).

As shown in the previous section the generators of the EEG can be described by a current source and sink or a current dipole source. A current corresponds to charges in motion and can be described by a current density, which is the current passing through an elementary surface. The current density J(x, y, z) is a 3D position-dependent vector field, where the direction of the vector indicates the direction of motion of the charges. The unit of the current density is A/m2.

The divergence of a vector field J is defined as follows:

$$\nabla \cdot \vec{J} = \lim_{G \to 0} \frac{1}{G} \oint_{\partial G} \vec{J} \cdot d\boldsymbol{S} \tag{2.5}$$

The integral over a closed surface ∂G represents a flux or a current through the volume G. This integral is positive when a net current leaves the volume G and is negative when a net current enters the volume G. The vector ***dS*** for a surface element of ∂G with area dS and outward normal ***e****n*, can also be written as

ee_{n}*·*dS*. The unit of ▽·J is A/m3 and is often called the current source density, symbolized with I_m.

From the Maxwell equations the continuity equation can be derived:

$$\frac{\partial \rho}{\partial t} + \nabla \cdot \vec{J} = 0 \qquad (2.6)$$

Where ρ is the charge density and ∇ **J** is the current source density. Equation 2.8 states that the change in charge inside a volume conductor with time must correspond to a flow of charge out through the surface of the volume conductor. In other words, a current leaving or entering the volume conductor G causes a change in the total amount of charges in G.

It is shown in [31] that no charge can be piled up in the conducting extracellular volume for the frequency range of the signals measured in the EEG. At one moment in time all the fields are triggered by the active electric source. Hence, no time delay effects are introduced. All fields and currents behave as if they were stationary at each instance in time. These conditions are also called quasi-static conditions. They are not static because the neural activity changes with time, but the changes are slow compared to the propagation effects. Therefore the charge density in the volume G is constant, thus equation (2.6) yields:

$$\nabla \cdot \vec{J} = 0 \qquad (2.7)$$

Due to the linearity of the Maxwell equations the current density inside the volume conductor, representing the human head, consists of the current density imposed by the dipole source or primary current density J_p and the current density flowing in the volume conductor or return current density J_r:

$$\vec{J} = \vec{J}_p + \vec{J}_r \qquad (2.8)$$

The return current density generates an electric field. The relationship between the return current density J_r in A/m2 and the electric field E in V/m is given by Ohm's law:

$$\vec{J}_r = \bar{\bar{\Sigma}}\vec{E} \tag{2.9}$$

With Σ being the position-dependent conductivity. The conductivity Σ depends entirely on the nature of the material of which the conductor is composed, the state of aggregation of its parts and its temperature. In the case of isotropic conductivities the conductivity is position-dependent scalar, σ(x, y, z). For anisotropic conductivities the conductivity can be written as a position dependent, symmetric, positive-definite second order tensor Σ, whose matrix representation $\Sigma(x, y, z) \in R^{3\times3}$ according to a basis (e_x,e_y,e_z) given by:

$$\bar{\bar{\Sigma}} \triangleq \begin{bmatrix} \sigma_{xx} & \sigma_{xy} & \sigma_{xz} \\ \sigma_{xy} & \sigma_{yy} & \sigma_{yz} \\ \sigma_{xz} & \sigma_{yz} & \sigma_{zz} \end{bmatrix}$$

and with units A/(V m) = S/m. There are tissues in the human head that have an anisotropic conductivity. This means that the conductivity is not equal in every direction and that the electric field can induce a current density component perpendicular to it. Combining equation 2.11 with equation 2.10 yields:

$$\vec{J} = \vec{J}_p + \bar{\bar{\Sigma}}\vec{E} \tag{2.10}$$

The scalar potential field V, having volt as unit, is now introduced. This is possible due to Faraday's law (see equation 2.5) in which the time derivative of B is zero under quasi-static conditions ($\nabla \times E = 0$). The link between the potential field and the electric field is given utilizing the gradient operator:

$$\vec{E} = -\nabla V \tag{2.11}$$

The vector ∇V at a point gives the direction in which the scalar field V, having volt as its unit, most rapidly increases. The minus sign in the latter equation indicates that the electric field is oriented from an area with a high potential to an area with a low potential.

When equations (2.10 (2.11) and (2.7) are combined, Poisson's differential equation is obtained in general form:

$$\nabla \cdot \left(\bar{\bar{\Sigma}} \nabla V\right) = \nabla \cdot \overrightarrow{J_p} \tag{2.12}$$

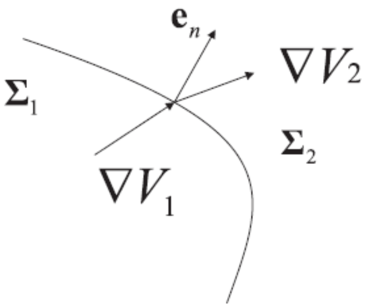

Figure 2-5 Boundary interface between two media

At the interface between two compartments, two boundary conditions are imposed. Figure 2-5 illustrates such an interface. A first condition is based on the inability to pile up charge at the interface. All charge leaving one compartment through the interface must enter the other compartment. In other words, all current (charge per second) leaving a compartment with conductivity Σ1 through the interface enters the neighbouring compartment with conductivity Σ_2.

$$\vec{J}_1 \cdot \hat{\boldsymbol{e}}_n = \vec{J}_2 \cdot \hat{\boldsymbol{e}}_n$$

$$\left(\bar{\bar{\Sigma}}_1 \cdot \nabla V_1\right) \cdot \hat{\boldsymbol{e}}_n = \left(\bar{\bar{\Sigma}}_2 \cdot \nabla V_2\right) \cdot \hat{\boldsymbol{e}}_n$$

where $\boldsymbol{e}_n$ is the normal component on the interface.

Since no current can be injected into the air outside the human head, due to the very low conductivity of the air, the Neumann boundary condition at the surface of the head reads:

$$\vec{J}_1 \cdot \hat{\boldsymbol{e}}_n = 0$$

$$\left(\bar{\bar{\Sigma}}_1 \cdot \nabla V_1\right) \cdot \hat{\boldsymbol{e}}_n = 0$$

The second boundary condition only holds for interfaces between non-air compartments, it is called Dirichlet boundary condition, and states the potential continuity across the interface:

$$V_1 = V_2$$

Because EEG signals are produced by ohmic current flow in the head, they are highly sensitive to the conductivity of the brain, skull, and extra cranial tissue. Consequently, solving a forward problem requires accurate knowledge of these properties. This leads to the modelling issue, i.e. the mathematical representation of actors involved in the so called forward problem, which will be discussed in the following paragraphs.

2.2.2.1 Source model

Current source and current sink inject and remove the same amount of current I and they represent an active pyramidal cell at microscopic level. They can be modelled as a current dipole. The position parameter r_d of the dipole is typically chosen half way between the two monopoles.

The dipole moment $\boldsymbol{m}$ is defined by a unit vector $\boldsymbol{e}_m$ (which is directed from the current sink to the current source) and a magnitude given by $m = I\,p$, with p the distance between the two monopoles.

Now, considering a dipole model source into a conductor volume, we can infer a numerical representation of the dipole itself by applying the divergence operator to small volumes which will be lately be referred to as discretization volumes.

For any volume enclosing both dipoles sink and source, clearly the net current flux is zero, i.e.

$$\nabla \cdot \vec{J}_p = 0$$

Whenever the volume encloses either the sink or the source of the dipole located at $\boldsymbol{r}_S$, the integral defining the divergence operator assumes the finite value $\pm I$ (the sign depends whether sink (-) or source (+) is enclosed in the volume). As the discretization volume G approaches zero, the singularity can be written by means of the Dirac's *delta* function. The superimposition of these three cases yields:

$$\nabla \cdot \vec{J}_p = I\, \delta(\boldsymbol{r} - \boldsymbol{r}_{\boldsymbol{source}}) - I\, \delta(\boldsymbol{r} - \boldsymbol{r}_{\boldsymbol{sink}})$$

The Poisson's equation hence becomes:

$$\nabla \cdot \left(\bar{\bar{\Sigma}} \nabla V\right) = I\, \delta(\boldsymbol{r} - \boldsymbol{r}_{\boldsymbol{source}}) - I\, \delta(\boldsymbol{r} - \boldsymbol{r}_{\boldsymbol{sink}}) \qquad (2.13)$$

From now on we will refer to the term *source space* as the union of all the possible locations for the source dipoles inside a head model. For what has been said in the paragraph 2.2.1.2, this space is usually considered coincident with the white-matter/grey-matter interface surface.

2.2.2.2 Lead Field

From the linearity of the Poisson's equation (2.12), it follows that the mapping from electric sources within the cranium to scalp recordings on the outside of the scalp can be represented by a linear operator **L**. In fact, due to a dipole at a position r_d and dipole moment $\boldsymbol{m}=m_x,\mathbf{e}_x+m_y,\boldsymbol{e}_y+m_z,\boldsymbol{e}_z$ a potential V at an arbitrary scalp measurement point $\boldsymbol{r}$ can be decomposed in:

$$V(\boldsymbol{r},\boldsymbol{r}_d,\boldsymbol{m}) = m_x V(\boldsymbol{r},\boldsymbol{r}_d,e_x) + m_y V\left(\boldsymbol{r},\boldsymbol{r}_d,e_y\right) + m_z V(\boldsymbol{r},\boldsymbol{r}_d,e_z) \tag{2.14}$$

where **r** and $\mathbf{r}_\mathrm{d}$ are the locations of the measurement electrode and the dipole source respectively. Hence, if we consider a set of M electrodes, placed on a regular basis on the scalp surface, and one dipolar source then the latter equation can be written as:

$$\boldsymbol{V}_m(t) = \begin{bmatrix} V_1(t) \\ \vdots \\ V_M(t) \end{bmatrix} = \begin{bmatrix} V(\boldsymbol{r}_1,\boldsymbol{r}_d,e_x) & V\left(\boldsymbol{r}_1,\boldsymbol{r}_d,e_y\right) & V(\boldsymbol{r}_1,\boldsymbol{r}_d,e_z) \\ \vdots & \vdots & \vdots \\ V(\boldsymbol{r}_M,\boldsymbol{r}_d,e_x) & V(\boldsymbol{r}_M,\boldsymbol{r}_d,e_x) & V(\boldsymbol{r}_M,\boldsymbol{r}_d,e_x) \end{bmatrix} \begin{bmatrix} m_x(t) \\ m_y(t) \\ m_z(t) \end{bmatrix} = \boldsymbol{L}(\boldsymbol{r_d}) \cdot \boldsymbol{m(t)} \tag{2.15}$$

L is the so-called *lead-field matrix* and contains information about the geometry and conductivity of the model.

Each element $L_{i,j}$ of the matrix **L**($\boldsymbol{r_d}$) represents the electric potential one would measure at the *i*-th (*i=1...M*) electrode caused by a single unary current dipole placed in $\boldsymbol{r_d}$ and oriented along *j*-th axis (*j=x, y, or z*).

In general, given a arbitrary configuration of sources, **m**, the measured potentials $\mathbf{V}_\mathrm{m}$, and the noise in the system, **n**, we extend equation (2.15) to the case of a distribution of N dipoles in a source space is the following:

$$\boldsymbol{V}_m(t) = \begin{bmatrix} V_1(t) \\ \vdots \\ V_M(t) \end{bmatrix} = \boldsymbol{L} \cdot \begin{bmatrix} \boldsymbol{m}_1\ (t) \\ \vdots \\ \boldsymbol{m}_N\ (t) \end{bmatrix} + \begin{bmatrix} n_1(t) \\ \vdots \\ n_M(t) \end{bmatrix} = \boldsymbol{L} \cdot \boldsymbol{m}(t) + \boldsymbol{n}(t) \tag{2.16}$$

where the columns of the matrix **L** $\in lR^{M\times 3N}$ contain the lead fields of the dipolar sources for the given M-channel EEG configuration, while $\mathbf{m}_\mathrm{i}(t)=[m_x(t),$

$m_y(t)$, $m_z(t)]^T$ represents the source activity of the current dipole placed in the i-th node of the source space.

Since the solution to the inverse problem consists of finding $\boldsymbol{m}$, this implies two steps: building the lead field matrix **L**, and "inverting" it, once the scalp potentials are known, and the noise is somehow guessed.

Finding the inverse of **L** is an ill-posed problem and its solution requires regularization. There exist many different regularization methods, as well as many papers describing their application to EEG/MEG, these will be shown in section 2.2.4 below. All of them assume that **L** either is known *a priori* or can be easily constructed. While it is true that **L** is easy to construct for simple and approximated geometries, building the **L** matrix is much more complicated for geometries based on real patient data.

In a number of application papers, researchers have been able to compute the L basis by exploiting analytic equations for each entry in L. The equations for the matrix entries, or kernels, for each method can be found in [32] For most of them, the L matrix is constructed one element at a time by evaluating the analytic expression for the potential at each recordings site the due to a source at each location in the domain.

The reciprocity theorem, validated in [33], [34], states that the potential difference between two electrodes A and B, due to a dipole $\boldsymbol{m}$ located at position $\boldsymbol{r}$, is proportional to the electric field in $\boldsymbol{r}$ due to the activity of two current monopoles, located at the very same position of the two electrodes, scaled by the current injected I_{AB}:

$$V_{AB}(\boldsymbol{r},\boldsymbol{m}) = \frac{\boldsymbol{m}^T \cdot \nabla\phi(\boldsymbol{r})}{I_{AB}} \tag{2.17}$$

Thus the number of forward computation is limited by the number of sensors applied. Moreover, since equation (2.17) implies the computation of a gradient, it requires potential values at each *node* inside the conductor volume. This is why reciprocity fits the features of numerical volumetric algorithm for the forward problem, described in the next section.

2.2.3 Head models and forward problem solution

Solutions to Poisson's equation are different, and are strictly related to the characteristics of the spatial domain in which solutions are searched.

Depending on the geometry assumed for the volume conductor model, the approaches that lead to a solution for the forward problem are either numerical or analytical. As an example, the simplest solution is the one related to a homogeneous conductor volume G with indefinite dimensions:

$$V(\boldsymbol{r}) = \frac{1}{4\pi\sigma} \cdot \int_G \vec{J}(\boldsymbol{r}_d) \cdot \frac{(\boldsymbol{r} - \boldsymbol{r}_d)}{|\boldsymbol{r} - \boldsymbol{r_d}|^3} d\boldsymbol{r}$$

When a spherical geometry is assumed for the considered model, a closed-form analytical solution of the forward problem can be used [35].

For many years, this type of solution is usually adopted for MEG and EEG forward problems. Although spherical models provide good approximations for MEG forward solutions [36], this is typically not the case for EEG.

Several approximated-geometry models have been implemented and studied over the past years [35], [37], [38], [39], [40]. Of course, they seriously lack in geometrical adherence of the assumed shape with respect to a real human head.

The "sensor-fitted sphere" approach introduced in [38] fits a multilayer sphere individually to each sensor and has shown to produce some improvement over standard spherical models [41].

More accurate forward solutions become possible by using numerical algorithms, such as the boundary element method (BEM) [42], finite-element method (FEM) [43] and finite difference method (FDM) [33] algorithms. These numerical models allow incorporating the realistic geometry of the head and brain after reconstruction of the anatomical structure from individual or standardized magnetic resonance imaging (MRI) data sets. Previous studies [44] have found that a more realistic head model performs better than a less complex, for example, spherical, head model in EEG simulations, since volume currents are more precisely taken into account. More specifically, the BEM approach is able to improve the source reconstruction in comparison with spherical models, particularly in basal brain areas, including the temporal lobe [45], because it gathers a more realistic shape of brain compartments of isotropic and homogeneous conductivities by using closed triangle meshes. The FDM and the FEM allow better accuracy than the BEM because they allow a better representation of the cortical structures, such as sulci and gyri in the brain, in a three-dimensional head model [46].

The effect of head model geometry on the EEG forward solution has been considered in several previous studies [44]. These studies analyzed the differences in EEG forward and inverse problem solution due to different spherical or realistic model geometry [36], [47], evaluated the effects of variations in the skull thickness [48] or due to different model complexity [46], presenting results for particular cases of head models.

2.2.3.1 Analytical solution and spherical models

The simplest EEG head model consists of a single-layer spherical shell of uniform conductivity σ. A closed-form solution for calculating the potential on the outermost surface is described by [49]. In practice, a singlelayer sphere proves too simplistic for the human head, which consists of multiple layers of conductivity varying by as much as two orders of magnitude between the skull and brain.

To account for the varying conductivity of brain, skull, scalp and optionally cerebrospinal fluid, three and four multilayer concentric-sphere analytic solutions have been derived, and are commonly used. These can be computed numerically using a truncated Legendre series [50]. Because of their simplicity, reasonable computation requirements and relatively good accuracy, multi-layer spherical models are by far the most widely used.

Methods to improve the computational efficiency of multilayer spherical models have focused primarily on approximating the infinite Legendre series. Following [32], a convenient formulation of the EEG/MEG forward model entails with factorizing the electric field potential or the magnetic field observed at one extra-cranial point as the product of a "field kernel" and the dipole moment of the intra-cranial source $\boldsymbol{m}$. For electrical potentials V, the field kernel is a 3x1 vector (**k**):

$$\boldsymbol{V}(\boldsymbol{r}) = \boldsymbol{k}^T(\boldsymbol{r}, \boldsymbol{r_m}) \cdot \boldsymbol{m} \tag{2.18}$$

Assuming that each spherical layer has uniform and constant conductivity, rapidly computable analytic solutions exist for both EEG and MEG forward problem. A practical formulation of the EEG kernels has been presented by Mosher et al. (1999), that only requires vectors expressed in their Cartesian form.

Ary et. al. in [51] recognized that a single-sphere model could, under certain circumstances, approximate a three-shell model with good accuracy. If we let $V_1(\mathbf{r}; \mathbf{r}_m, \mathbf{m})$ and $V_3(\mathbf{r}; \mathbf{r}_m, \mathbf{m})$ represent the potentials function on a single-layer and a three-layer spheres respectively, then we can approximate $V_3(r; r_m, m)$ by adjusting the location of the dipole along its radial direction $\boldsymbol{r}_m/|\boldsymbol{r}_m|$ by a scale factor of μ, compute the much simpler single-sphere solution and then scale the solution by λ.

Further refinements of this general approximation concept [52], [35] resulted in the remarkably accurate approximation and a convenient method for approximating an EEG field kernel from a multi-layer spherical model as the weighted sum of three kernels from a single-layer spherical model applied to a modified source configurations:

$$\boldsymbol{k}(\boldsymbol{r},\boldsymbol{r_m}) = \lambda_1 \cdot \boldsymbol{k}_{ss}(\boldsymbol{r},\mu_1\boldsymbol{r}_m) + \lambda_2 \cdot \boldsymbol{k}_{ss}(\boldsymbol{r},\mu_2\boldsymbol{r}_m) + \lambda_3 \cdot \boldsymbol{k}_{ss}(\boldsymbol{r},\mu_3\boldsymbol{r}_m)$$

where:

$$\boldsymbol{k_{ss}}(\boldsymbol{r},\boldsymbol{r_m}) = \big(c_1 - c_2 \cdot (\boldsymbol{r}\cdot\boldsymbol{r_m})\big)\cdot \boldsymbol{r}_m + c_2 \cdot r_m^2 \cdot \boldsymbol{r}$$

$$c_1 := \frac{1}{4\pi\sigma r_m^2}\cdot\left(2\frac{\boldsymbol{d}\cdot\boldsymbol{r}_m}{d^3} + \frac{1}{d} - \frac{1}{r}\right) \tag{2.19}$$

$$c_2 := \frac{1}{4\pi\sigma r_m^2}\cdot\left(\frac{2}{d^3} + \frac{d+r}{r\cdot d\cdot\big(r\cdot d + r^2 - (\boldsymbol{r_m}\cdot\boldsymbol{r})\big)}\right)$$

$$\boldsymbol{d} \overset{\text{def}}{=} \boldsymbol{r} - \boldsymbol{r_m}$$

Zhang refers to the parameters μ_j and λ_j as the Berg eccentricity and magnitude parameters respectively, and hence we will refer to this approach as the *Berg approximation*. As for the Legendre series being approximated, the parameters μ_j and λ_j are dependent only on the sphere radii/conductivity profile and independent of dipole position $\boldsymbol{r}_m$.

In order to reduce errors introduced by the spherical approximation, Huang et. al. [38] found the optimally fit sphere at each sensor that best approximates the true lead-field for the actual head volume.

A schematic diagram of the sensor-fitted sphere model described in [38] is shown in the figure below:

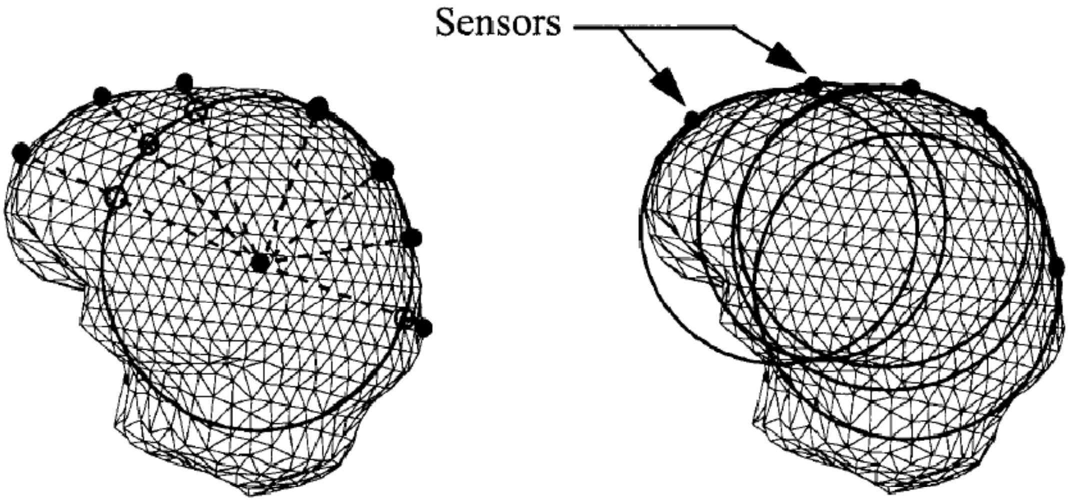

Figure 2-6 Spherical head models. right: sensor-fitted model, executed fitting one spherical model for each sensor. left: classic spherical model

In [38], rather than find a single locally best fitting sphere for all sensors based on the head geometry, has been carried out a fitting of the spherical model on a sensor-by-sensor basis using a set of grid points within the brain. It has been shown that the optimal fitting of each sensor-related sphere can be found either minimizing the correlation with a pre-computed golden standard lead-field, .e.g. using BEM algorithm, or on a geometric basis, e.g. minimizing the distance between each sphere's surface and all the others sensors.

2.2.3.2 Boundary Element Method

The BEM allows one to calculate the electrical potential V of a current source in an inhomogeneous conductor by solving the following integral equation if the conducting object is divided by closed surfaces S_i ($i = 1, \ldots, n_s$) into n_s compartments, each having a different enclosed isotropic conductivity σ_i^{in} . The electrical potential at position $\boldsymbol{r} \in S_k$ is then given by [53]:

$$\bar{\sigma}_k V(\boldsymbol{r}) = \sigma_0 V_0(\boldsymbol{r}) + \frac{1}{4\pi}\sum_{i=1}^{n_s} \Delta\sigma_i \oiint_{S_i} V(\boldsymbol{r}')\hat{\boldsymbol{n}}(\boldsymbol{r}') \cdot \frac{\boldsymbol{r}' - \boldsymbol{r}}{|\boldsymbol{r}' - \boldsymbol{r}|^3} dS'_i \tag{2.20}$$

with V_0 representing the potential of the source in an unlimited homogeneous medium with conductivity σ_0, the mean conductivity $\bar{\sigma}_k \overset{\text{def}}{=} (\sigma_k^{in} + \sigma_k^{out})/2$, and the conductivity differences $\Delta\sigma_i \overset{\text{def}}{=} \left(\sigma_i^{in} + \sigma_i^{out}\right)$.

To calculate the electrical fields it is necessary to approximate numerically the integrals over the closed surfaces S_i of the conductor boundaries consisting of differential surface elements dS'_i and with surface normal orientations $\hat{\boldsymbol{n}}$ at positions $\boldsymbol{r}'$.

The surfaces are described by a large number of small triangles and the integrals are replaced by summations over these triangle areas. Different assumptions about the variation of the potential over the triangle area can be applied [54], [55], [56], [42], [57]: averaged, regionally constant, linear, and quadratic dependencies. The potential values or the coefficients of the basis functions used to approximate the potentials on the surface elements form a vector of unknowns, which can be solved through the following matrix formulation:

$$\bar{\bar{\boldsymbol{\sigma}}}\boldsymbol{V} = \boldsymbol{\sigma_0 V_0} + \bar{\bar{\boldsymbol{B}}}\boldsymbol{V} \Rightarrow \boldsymbol{V} = (\bar{\bar{\boldsymbol{\sigma}}} - \bar{\bar{\boldsymbol{B}}})^{-1}\boldsymbol{\sigma_0 V_0} \tag{2.21}$$

If one explicitly solves equation (2.21) just for the fixed number of sensor positions, a transfer matrix T is obtained that relates the sensor signals to the homogeneous potentials, that depends on the geometry of the surfaces and the conductivities of each region. The potential vector **V**, containing the field distribution at all skin nodes, generated by a (dipolar) source inside the innermost compartment –the brain-, can thus be easily computed by a simple matrix-vector multiplication:

$$\bar{\bar{\boldsymbol{T}}} = (\bar{\bar{\boldsymbol{\sigma}}} - \bar{\bar{\boldsymbol{B}}})^{-1}\boldsymbol{\sigma_0} \Rightarrow \boldsymbol{V} = \bar{\bar{\boldsymbol{T}}}\boldsymbol{V_0} \tag{2.22}$$

The column vector V_0 contains the electrical potential values V_{0i} of all BEM model nodes i at position $\boldsymbol{r}_i$ for the source in an infinite homogeneous conductor with conductivity σ_0 (dipole at position $\boldsymbol{r}_j$, with current density $\vec{J}$):

$$V_{0i} = \frac{1}{4\pi\sigma_0}\vec{\boldsymbol{J}} \cdot \frac{\boldsymbol{r}_i - \boldsymbol{r}_j}{\left|\boldsymbol{r}_i - \boldsymbol{r}_j\right|^{3}} \tag{2.23}$$

To achieve a better computational performance, the LF of dipoles at positions on regular grids inside the innermost compartment were computed and stored for all virtual electrode positions on the skin mesh The LF of a dipolar source at an arbitrary position inside the volume conductor can then be approximated by three-dimensional linear interpolation between the precomputed LF of the eight closest regular grid positions [41], [58].

Finally, the potential distribution at the real electrode positions is calculated by two-dimensional linear interpolation from the three closest virtual electrodes [59].

Since an exact solution of the integral in eq. (2.20) is generally not achievable, an approximated solution $\widetilde{V}_i(\boldsymbol{r})$ on surface S_i may be defined as a linear combination of N_i simple basis functions:

$$\widetilde{\boldsymbol{V}}_{\boldsymbol{i}}(\boldsymbol{r}) = \sum_{j=1}^{N_i} \varphi_j^k h_j(\boldsymbol{r}) \tag{2.24}$$

Where N_i is the number of discretization elements –triangles- in the i-th interface between the volume compartments. The basis function $h_j(\mathbf{r})$ can be defined in several ways. The “constant potential” formulation, for instance, uses basis function defined as:

$$h_j(\boldsymbol{r}) = \begin{cases} 1 & \boldsymbol{r} \in \Delta_j \\ 0 & \boldsymbol{r} \notin \Delta_j \end{cases} \tag{2.25}$$

where Δ_j denotes the *j*th planar triangle on the tessellated surface. The collocation points are typically the centroids of the surface or the vertices.

The coefficients φ_j^k represent unknowns on surface S_i whose values are determined by constraining $\widetilde{\mathbf{V}}_\mathbf{i}(\mathbf{r})$ to satisfy (2.20) at discrete points, also known as collocation points.

2.2.3.3 Finite Difference Method

Finite Difference Method (FDM), Finite Element Method (FEM) and Boundary Element Method (BEM) have been largely used in many engineering application for numerical approximation to partial differential equation solution.

Analytical solutions are continuous in space and time and provide exact results for specific boundary and initial conditions. An analytical solution can be found only for a limited set of boundary conditions and initial conditions.

Numerical solutions are discrete in space and time; the spatial domain is divided into discrete elements, called the mesh or grid spacing. An approximation to the exact results is given by an estimation of the value of the derivatives using information about the function at the discrete grid points.

Although BEM has advantages with respect to the computational complexity, it is not able to handle anisotropic conductivities.

FEM and FDM are both suitable method for the present work. FDM imposes regular grid over the domain, whereas FEM allows arbitrary shaped elements over the mesh. The computational work required to obtain the same level of error by FEM and FDM varies, depending on problems and the schemes employed however generally FDM takes less computational time and storage space for the same number of grid points.

Given $u(\mathrm{x})$ a finite and continuous function of x, because of Taylor's theorem:

$$u(x+h) = u(x) + h\frac{\partial u(x)}{\partial x} + \frac{1}{2!}h^2\frac{\partial^2 u(x)}{\partial x^2} + \frac{1}{3!}h^3\frac{\partial^3 u(x)}{\partial x^3} + \cdots$$

$$u(x-h) = u(x) - h\frac{\partial u(x)}{\partial x} + \frac{1}{2!}h^2\frac{\partial^2 u(x)}{\partial x^2} - \frac{1}{3!}h^3\frac{\partial^3 u(x)}{\partial x^3} + \cdots \tag{2.26}$$

Addition of the latter two equations gives:

$$u(x+h) + u(x-h) = 2u(x) + h^2\frac{\partial^2 u(x)}{\partial x^2} + O(h^4) \tag{2.27}$$

where $O(h^4)$ represents terms containing fourth or higher powers of h. Assuming $O(h^4)$ negligible compared with lower power of h yields:

$$\frac{\partial^2 u(x)}{\partial x^2} \cong \frac{1}{h^2}[u(x+h) - 2u(x) + u(x-h)] \tag{2.28}$$

with a leading error of order h^2.

Equation (2.28) is a central difference formula and it approximates the tangent at P by the slope of the chord AB, in the figure below.

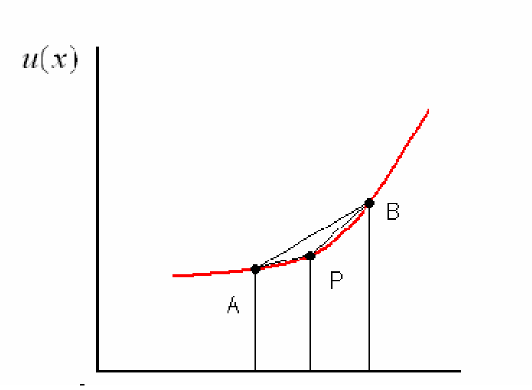

Figure 2-7example of finite difference approximation in 1-D: first order central, forward and backward difference around point P

Moreover the slope of the tangent at P can also be approximated either by the slope of the chord PB, which gives the forward difference formula:

$$\frac{\partial u(x)}{\partial x} \cong \frac{1}{h}[u(x+h)-u(x)] \tag{2.29}$$

or the slope of the chord AP, which gives the backward difference formula:

$$\frac{\partial u(x)}{\partial x} \cong \frac{1}{h}[u(x)-u(x-h)] \tag{2.30}$$

In both cases the leading errors are $O(h^2)$.

Since the numerical domain of this method is a regular 3D voxel grid, it is necessary to specify the relationship between nodes and voxels.

The FD formulation proposed and validated in [60] for inhomogeneous anisotropic field problems is first derived in the two dimensional (2-D) space for an easy understanding. The FD formulation has similarities to the one proposed and implemented by Saleheen and Kwong in [61] to determine the potential distribution in a canine torso during electrical defibrillation. The method presented in [61] differs from standard FD formulations since voxels are mapped as mesh elements and nodes of the mesh correspond to voxels' vertexes. In the method proposed in [60], the way the mesh is developed is different and follows standard FD formulations, as it considers the centre of the voxels as the mesh´s nodes and the computational points set in the voxels' center (see Figure 2-10), with a one-to-one correspondence between nodes and voxels: node 0 in Figure 2-8 represents a typical node surrounded by eight neighbors.

Problem formulation starts from homogeneous Laplace's equation:

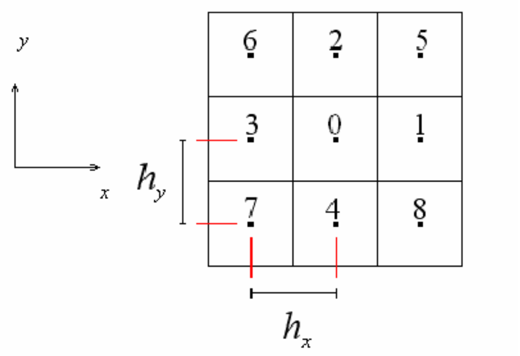

Figure 2-8 2-D grid nodes arrangement. Generally the spacing between nodes in x and y direction can be different

$$\nabla \cdot \left(\bar{\bar{\Sigma}} \nabla V\right) = 0 \tag{2.31}$$

where now $\bar{\bar{\Sigma}}$ represents the 2-D tensor in Cartesian coordinates

$$\bar{\bar{\Sigma}} \triangleq \begin{bmatrix} \sigma_{xx} & \sigma_{xy} \\ \sigma_{xy} & \sigma_{yy} \end{bmatrix}$$

the Laplacian operator can be expanded in terms of the corresponding derivatives as

$$\begin{aligned} \sigma_{xx}\frac{\partial^2 V}{\partial x^2} + \sigma_{yy}\frac{\partial^2 V}{\partial y^2} + 2\sigma_{xy}\frac{\partial^2 V}{\partial x \partial y} + \left(\frac{\partial \sigma_{xx}}{\partial x} + \frac{\partial \sigma_{xy}}{\partial y}\right)\frac{\partial V}{\partial x} \\ + \left(\frac{\partial \sigma_{yy}}{\partial y} + \frac{\partial \sigma_{xy}}{\partial x}\right)\frac{\partial V}{\partial y} = 0 \end{aligned} \tag{2.32}$$

Taylor series expansions around node 0 are developed for the products of the conductivities and potentials in eq. (2.32) at the neighbouring nodes 1-8, where σ is an appropriate entry of conductivity tensors associated with neighbouring elements around node 0. Diagonal terms of conductivity tensor are used for nodes lying in principal directions from node 0 while off-diagonal terms are used in diagonal directions. Only terms up to the second order are considered in the series expansions, constituting a system of eight different equations, one for each node.

The derivatives $\partial V/\partial y$, $\partial \mathrm{V}/\partial x$, $\partial^2 \mathrm{V}/\partial x^2$, $\partial^2 V/\partial y^2$ and $\partial^2 \mathrm{V}/\partial x \partial y$ at node 0 can then be expressed in term of potential and conductivities at all the nodes (0, …, 8) by solving these equations [61]. Substituting the expressions obtained for derivatives into eq. (2.32), we obtain the potential at node 0 in terms of the potentials and conductivities at the surrounding nodes, which can be expressed by:

$$\sum_{i=1}^{8} A_i V_i = \left(\sum_{i=1}^{8} A_i\right) V_0 \tag{2.33}$$

with

$$A_1 = \sigma_{xx(1)}\left(\frac{1}{h_x^2} - \frac{\sigma_x}{\sigma_{xx(0)}}\right) \quad A_2 = \sigma_{yy(2)}\left(\frac{1}{h_y^2} - \frac{\sigma_y}{\sigma_{yy(0)}}\right)$$

$$A_3 = \sigma_{xx(3)}\left(\frac{1}{h_x^2} + \frac{\sigma_x}{\sigma_{xx(0)}}\right) \quad A_4 = \sigma_{yy(4)}\left(\frac{1}{h_y^2} + \frac{\sigma_y}{\sigma_{yy(0)}}\right)$$

$$A_5 = \frac{\sigma_{yy(5)}}{2h_x h_y} \quad A_6 = -\frac{\sigma_{xy(6)}}{2h_x h_y}$$

$$A_7 = \frac{\sigma_{xy(7)}}{2h_x h_y} \quad A_8 = \frac{\sigma_{xy(8)}}{2h_x h_y}$$

where

$$\sigma_x = \frac{1}{2h_x^2}\left(\frac{\partial \sigma_{xx}}{\partial x} + \frac{\partial \sigma_{xy}}{\partial y}\right)\Bigg|_{(0)} \quad \sigma_y = \frac{1}{2h_y^2}\left(\frac{\partial \sigma_{xy}}{\partial x} + \frac{\partial \sigma_{yy}}{\partial y}\right)\Bigg|_{(0)}$$

Indexes (0) - (8) indicate the node at which the derivative of the conductivity is considered, which is associated with a node corresponding to a voxel. Since conductivity is considered to be constant over a voxel, the general term $\partial\sigma_x/\partial x$ (0) is zero and the terms σ_x and σ_y disappear.

As a consequence, it can be noticed that in this formulation the conductivity of the central voxel 0 is not taken into account. Furthermore, to avoid neglecting it, the general term $\sigma_{i,j(k)}$ is taken as the average of the term $\sigma_{i,j}$ at node k and node 0, with $i = x, y$, $j = x, y$ and k=1, ..., 8.

With this approach a sort of smooth transition of conductivity between the elements of the mesh can be achieved. This approximation guarantees accurate results and it increases speed convergence. Finally, the A_i coefficients of equation (2.33) are given by:

$$
\begin{aligned}
A_1 &= \frac{\left(\sigma_{xx}^{[1]} + \sigma_{xx}^{[0]}\right)}{2h_x^2} & A_2 &= \frac{\left(\sigma_{yy}^{[2]} + \sigma_{yy}^{[0]}\right)}{2h_y^2} \\
A_3 &= \frac{\left(\sigma_{xx}^{[3]} + \sigma_{xx}^{[0]}\right)}{2h_x^2} & A_4 &= \frac{\left(\sigma_{yy}^{[4]} + \sigma_{yy}^{[0]}\right)}{2h_y^2} \\
A_5 &= \frac{\left(\sigma_{xy}^{[5]} + \sigma_{xy}^{[0]}\right)}{4h_x h_y} & A_6 &= \frac{\left(\sigma_{xy}^{[6]} + \sigma_{xy}^{[0]}\right)}{4h_x h_y} \\
A_7 &= \frac{\left(\sigma_{xy}^{[7]} + \sigma_{xy}^{[0]}\right)}{4h_x h_y} & A_8 &= \frac{\left(\sigma_{xy}^{[8]} + \sigma_{xy}^{[0]}\right)}{4h_x h_y}
\end{aligned}
$$

Indexes [0]–[8] individuate the voxel to which tensor entry refers. This formulation presents a leading error of h^2.

Problem formulation is then extended to the 3-D case. In a three dimensional space voxels are organized like in Figure 2-10 where the grey spheres represent the centre of the voxel.

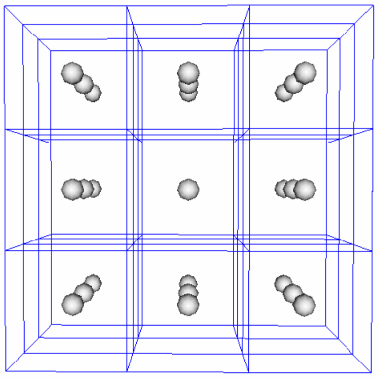

Figure 2-10 3-D grid nodes representation in the current FD formulation

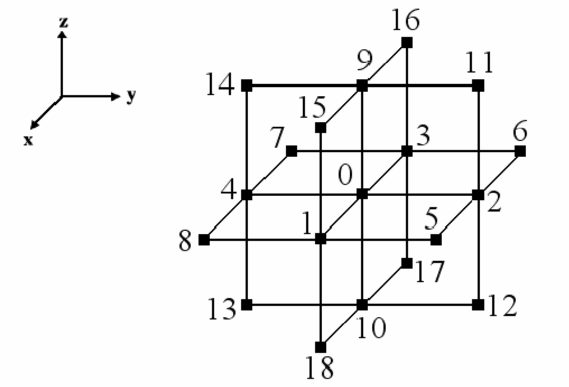

Figure 2-9: grid elements (or nodes) arrangement around node 0

In conformity with the indexes of Figure 2-9, where node 0 is surrounded by 18 neighbours, the final 3-D FD formulation becomes:

$$\sum_{i=1}^{18} A_i V_i = \left(\sum_{i=1}^{18} A_i \right) V_0$$

where

$$A_1 = \frac{\left(\sigma_{xx}^{[1]} + \sigma_{xx}^{[0]}\right)}{2h_x^2} \qquad A_2 = \frac{\left(\sigma_{yy}^{[2]} + \sigma_{yy}^{[0]}\right)}{2h_y^2} \qquad A_3 = \frac{\left(\sigma_{xx}^{[3]} + \sigma_{xx}^{[0]}\right)}{2h_x^2}$$

$$A_4 = \frac{\left(\sigma_{yy}^{[4]} + \sigma_{yy}^{[0]}\right)}{2h_y^2} \qquad A_5 = \frac{\left(\sigma_{xy}^{[5]} + \sigma_{xy}^{[0]}\right)}{4h_x h_y} \qquad A_6 = -\frac{\left(\sigma_{xy}^{[6]} + \sigma_{xy}^{[0]}\right)}{4h_x h_y}$$

$$A_7 = \frac{\left(\sigma_{xy}^{[7]} + \sigma_{xy}^{[0]}\right)}{4h_x h_y} \qquad A_8 = -\frac{\left(\sigma_{xy}^{[8]} + \sigma_{xy}^{[0]}\right)}{4h_x h_y} \qquad A_9 = \frac{\left(\sigma_{zz}^{[9]} + \sigma_{zz}^{[0]}\right)}{2h_z^2}$$

$$A_{10} = \frac{\left(\sigma_{zz}^{[10]} + \sigma_{zz}^{[0]}\right)}{2h_z^2} \qquad A_{11} = \frac{\left(\sigma_{zy}^{[11]} + \sigma_{zy}^{[0]}\right)}{4h_z h_y} \qquad A_{12} = -\frac{\left(\sigma_{zy}^{[12]} + \sigma_{zy}^{[0]}\right)}{4h_z h_y}$$

$$A_{13} = \frac{\left(\sigma_{zy}^{[13]} + \sigma_{zy}^{[0]}\right)}{4h_z h_y} \qquad A_{14} = -\frac{\left(\sigma_{zy}^{[14]} + \sigma_{zy}^{[0]}\right)}{4h_z h_y} \qquad A_{15} = \frac{\left(\sigma_{zx}^{[15]} + \sigma_{zx}^{[0]}\right)}{4h_z h_x}$$

$$A_{16} = -\frac{\left(\sigma_{zx}^{[16]} + \sigma_{zx}^{[0]}\right)}{4h_z h_x} \qquad A_{17} = \frac{\left(\sigma_{zx}^{[17]} + \sigma_{zx}^{[0]}\right)}{4h_z h_x} \qquad A_{18} = -\frac{\left(\sigma_{zx}^{[18]} + \sigma_{zx}^{[0]}\right)}{4h_z h_x}$$

Indexes within brackets [0] – [18] individuate to which voxel the tensor entry refers.

Since we are deriving a numeric formulation for computing the EEG forward problem in a finite volumes environment, clearly the Dirac's *delta* function must be approximated as follows:

$$\delta(\boldsymbol{r} - \boldsymbol{r_0}) = \left\{ \begin{matrix} \dfrac{1}{(h_x h_y h_z)} & where\ \boldsymbol{r} = \boldsymbol{r_0} \\ 0 & anywhere\ else \end{matrix} \right\}$$

Hence the right hand sides of (2.13) turn into:

$$I\,\delta(\boldsymbol{r}-\boldsymbol{r_{source}})-I\,\delta(\boldsymbol{r}-\boldsymbol{r_{sink}}) = \left\{\begin{array}{cc} \dfrac{1}{(h_x h_y h_z)}\dfrac{|\vec{\boldsymbol{m}}|}{p} & if\ \boldsymbol{r}=\boldsymbol{r}_{source} \\ -\dfrac{1}{(h_x h_y h_z)}\dfrac{|\vec{\boldsymbol{m}}|}{p} & if\ \boldsymbol{r}=\boldsymbol{r}_{sink} \\ 0 & elsewhere \end{array}\right\} \tag{2.34}$$

Once the dipole position is set, its closest node is located by i , j ,k indices spanning the 3-D grid space in x, y and z directions, respectively.

Clearly, regardless of the actual resolution of the model, that directly depends on the resolution of the MRI images, the best accuracy in dipole representation is obtained setting p as the minimum distance between two distinct monopoles, that is $h_{x,y,\ or\ z}$.

Thus, the model of the dipolar source can be finally fully described by the values of the six neighbouring nodes:

$$I_{i-1,j,k}=-\frac{m_x}{h_x^2 h_y h_z} \quad I_{i,j-1,k}=-\frac{m_y}{h_x h_y^2 h_z} \quad I_{i,j,k-1}=-\frac{m_z}{h_y h_x h_z^2}$$
$$I_{i+1,j,k}=\frac{m_x}{h_x^2 h_y h_z} \quad I_{i,j+1,k}=\frac{m_y}{h_x h_y^2 h_z} \quad I_{i,j,k+1}=\frac{m_z}{h_y h_x h_z^2}$$

2.2.4 EEG inverse modelling

As opposed to the well-posed forward modelling and computation, the EEG inverse problem results more challenging.

As an infinite number of source configurations can produce the same potential distribution on the scalp surface, the EEG inverse problem is considered a severely ill problem [62], [63], [64]. To reduce the number of possible solutions, some constraints about the source are always needed, i.e., the assumption of a proper source model. Many studies investigated this topic [62], and as a result the single current dipole model, also known as the equivalent current dipole, is the model that best fits for problems related to focal brain activity [65] and is used in this study. Furthermore, owing to the linearity of the forward problem, more complex activity can always be represented by superposition of a dipole distribution [66].

Several previous studies aimed to compare realistic geometry models to spherical models, focusing on their performances in source localisation (i.e., their application to the inverse problem). Although this is clearly a practical validation perspective, it is affected by the intrinsic uncertainties related to the particular source localization algorithm (inverse method) adopted. In fact, the imaging performance of all linear and nonlinear EEG inverse algorithms varies from case to case, depending on the nature of the brain electrical activity under analysis.

Although the evaluation of some typical algorithms has been carried out in a few experimental and simulation settings, a general conclusion or agreement regarding a single optimal inverse approach, if at all possible, has not been reached [67]. In particular, the main issue to be addressed is the regularization problem. Referring to equation (2.16), all linear distributed inverse solutions can be expressed as a collection of many spatial filters (one per source dipole component and one per source position). Altogether, these spatial filters are applied to channel data for generating the estimated EEG/MEG source time-series in all source locations and for all source orientations:

$$\widetilde{\boldsymbol{m}}(t) = \boldsymbol{W} \cdot \boldsymbol{V}_{\boldsymbol{m}}(t) \tag{2.35}$$

In this formulation, matrix **W** contains all spatial filter weights (one weight per source dipole component and location and per channel) and $\widetilde{\boldsymbol{m}}(t)$ is the estimated source time-series for all components and locations. Assuming a measurement configuration with M channels, N sources and a *free orientation model* (i.e. X, Y and Z components are considered for each dipole), matrix **W** has order 3*N*M.

Since the orientation of the main EEG generators is orthogonal to the surface of the gray matter, as previously stated in section 2.2.1.2, it is common to constrain the orientation of each source before the computation of the lead field matrix, that hence will result of order N*M.
Similarly to the lead field matrix, the inverse solution matrix **W** is stored as a collection of 3*M or M maps defined across all N source points depending on the orientation constrain. The estimation of the inverse solution **W** can proceed by either attempting a total inversion of the distributed ECD (DECD) model in (2.16) across the entire source space –the so called “imaging” approach- or by filling three-by-three the rows of **W** at each source location -“scanning” approach-.

The problem of all imaging approach is that N >> M, and this makes the linear problem severely ill-posed, i.e. no unique solutions exist if the only constrain is minimizing the residual term for fitting the measurements. Therefore, besides the obvious mathematical constrain or minimizing the residual term in (2.16), additional more “physical” constraints are to be posed to achieve a unique solution.

2.2.4.1 Weighted Minimum Norm approach

One of the most popular “imaging” approach is the weighted minimum-norm (WMN). The WMN compensates the lower gains of deeper sources by using *lead field normalization.* In this approach the weights in (2.35) are estimated in such a way to produce the source distribution with the minimum power that fits the measurements in a least-square-error sense:

$$\boldsymbol{W} = \boldsymbol{R}\boldsymbol{L}^T(\boldsymbol{L}\boldsymbol{R}\boldsymbol{L}^T + \lambda^2\boldsymbol{C_N})^{-1} \qquad (2.36)$$

Here, **R** represents the “a priori” source covariance matrix and is used to “inform” or “re-weight” the solution, i.e. to incorporate some prior knowledge about the spatial distribution of the source activity (**R**=**I** in case of no weighting).

C_N is the *covariance* matrix of the channel noise **n**(t) in and is used to "regularize" the solution with respect to the actual noise distribution in the channel space. Assuming the noise spatially uniform across all channel sites corresponds to **C_N**=**I**.

The regularization parameter λ controls the amount of regularization in relation to the expected SNR.

Since minimum-norm solutions are intrinsically biased towards superficial source locations, a common weighting scheme called *depth-weighting* specifies **R** as a diagonal matrix with non-zero entries inversely proportional to the γ–th power of lead field norms, with γ being the depth-weighting parameter:

$$L_i = \begin{bmatrix} (\boldsymbol{L})_{0,(3i+0)} & (\boldsymbol{L})_{0,(3i+1)} & (\boldsymbol{L})_{0,(3i+2)} \\ \vdots & \vdots & \vdots \\ (\boldsymbol{L})_{M-1,(3i+0)} & (\boldsymbol{L})_{M-1,(3i+1)} & (\boldsymbol{L})_{M-1,(3i+2)} \end{bmatrix} \qquad (2.37)$$

$$(R)_{ij} := \begin{cases} \|L_i\|^{-2\gamma} & (i = j) \\ 0 & (i \neq j) \end{cases}$$

2.2.4.2 Laplacian-WMN and LORETA

An important variant of WMN is the Laplacian WMN which gives the mathematical basis of the so-called Low-Resolution Electro-magnetic Topographic Analysis (*LORETA*) approach:

$$(\boldsymbol{K})_{ij} = \begin{cases} 1 & (i = j) \\ -\dfrac{1}{N_{max}} & (j \in V_i) \\ 0 & else \end{cases} \qquad (2.38)$$

$$\boldsymbol{R} = \boldsymbol{R}_{dw}(\boldsymbol{K} \cdot \boldsymbol{K}^T)^{-1}$$

where V_i represents the set of nearest "neighbours" of the source location at node *i* on the source space grid –or mesh- and N_{max} the cardinal number of V_i. $\mathbf{R}_{dw}$ is the same as in (2.37) and allows combining depth and spatial Laplacian weighting, thus giving the depth-compensated inverse solution under the constraint of smoothly distributed sources

2.2.4.3 Local Autoregressive Average

Local Autoregressive Average –or *LAURA*- weighting is similar to LORETA, but the physical distances between sources d_{ij} are involved in the weighting function and the cardinal number of V_i is allowed to vary across source locations:

$$(\boldsymbol{K})_{ij} = \begin{cases} \frac{N_{max}}{N_i} \cdot \sum\limits_{k \epsilon V_i} d_{ik}^{-2} & (i = j) \\ -d_{ij}{}^{-2} & (j \in V_i) \\ 0 & else \end{cases} \qquad (2.39)$$
$$\boldsymbol{R} = \boldsymbol{R}_{dw}(\boldsymbol{K} \cdot \boldsymbol{K}^T)^{-1}$$

2.2.4.4 Spatial filter normalization

After estimation of the WMN spatial filter (2.36), some form of normalization of the weights is usually applied. Dale et al. in [68] have proposed scaling the filter weights at each source point by their variances in the channel space.

$$(\boldsymbol{W})_{(3i+\beta),j} \to \frac{(\boldsymbol{W})_{(3i+\beta),j}}{\sqrt{\sum_{q=0}^{2} \sum_{k=0}^{M-1} \left[(\boldsymbol{W})_{(3i+q),k}\right]^2}} \qquad \begin{matrix} i = 0, \dots, N-1 \\ j = 0, \dots, M-1 \\ \beta = 0,1,2 \end{matrix} \qquad (2.40)$$

Applying this *noise-based normalization* has the important advantage of making the *point-spread function* (PSF) of each source -i.e. the image of a point current source placed in a given position- more uniform across the entire cortical space, compared to the case of a minimum-norm solution without such normalization.

A variation of the noise-based normalization is the so-called *standardized LORETA* or *s-LORETA* [69] that normalizes the inverse solution at each source location using the *resolution matrix* **T**. More specifically, the set of filter weights for the source at location *i* are jointly normalized using the i-th 3x3 block **T**$_\mathbf{i}$ along the diagonal of matrix **T**:

$$\boldsymbol{T} = \boldsymbol{W} \cdot \boldsymbol{L}$$

$$\boldsymbol{T}_i = \begin{bmatrix} (\boldsymbol{T})_{(3i+0),(3i+0)} & (\boldsymbol{T})_{(3i+0),(3i+1)} & (\boldsymbol{T})_{(3i+0),(3i+2)} \\ (\boldsymbol{T})_{(3i+1),(3i+0)} & (\boldsymbol{T})_{(3i+1),(3i+1)} & (\boldsymbol{T})_{(3i+1),(3i+2)} \\ (\boldsymbol{T})_{(3i+2),(3i+0)} & (\boldsymbol{T})_{(3i+2),(3i+1)} & (\boldsymbol{T})_{(3i+2),(3i+2)} \end{bmatrix}$$

$$\boldsymbol{w}_{i,j} = \begin{bmatrix} (\boldsymbol{W})_{(3i+0),j} \\ (\boldsymbol{W})_{(3i+1),j} \\ (\boldsymbol{W})_{(3i+2),j} \end{bmatrix} \quad \begin{matrix} i = 0, \dots, N-1 \\ j = 0, \dots, M-1 \end{matrix} \qquad (2.41)$$

$$\boldsymbol{w}_{i,j} \rightarrow \boldsymbol{T}_i^{-1} \cdot \boldsymbol{w}_{i,j}$$

2.2.4.5 The regularization parameter

While weighting entails with applying data-independent mathematical and physical constraints to an inverse solution, a regularization parameter (λ in equation (2.36)) is also introduced to avoid magnification of errors in data in relation to signal-to-noise ratio (SNR). In fact, due to the ill-posed nature of the problem of inverting the linear model in (2.16) for N > M, imaging approaches always requires some form of regularization. A convenient formula can be used to relate the regularization parameter to source SNR:

$$\lambda = \frac{trace(\boldsymbol{LRL}^T)}{trace(\boldsymbol{C}_N) \cdot SNR^2} \qquad (2.42)$$

This formula allows adjusting the regularization in terms of a realistic guess for the signal-to-noise ratio (SNR) of the current sources. The lower the “guess” SNR, the higher the value of lambda that means less spatial resolution but higher sensitivity. The higher the “guess” SNR, the lower the value of lambda which means higher resolution but less sensitivity (i.e. we need higher SNRs to “resolve” a given source). Plotting the lambda values vs the SNR values normally provide a typical L-shaped curve. Ideally, one should choose the “knee” of this curve.

2.2.4.6 *Scanning* approaches: beamforming

Beamforming is a technique that performs a spatial filtering of signals measured at discrete sensors [70]. Beamformers calculate a linear combination of the time sequences measured at the different sensors, with the aim of preserving the signal components originating from a desired direction or location, while at the same time suppressing interference from other directions or locations. A typical application of beamforming is a spatial filtering of radar signals, in which the signal in a certain direction-of-arrival is to be extracted from the signals measured at a linear sensor array. Beamforming can be applied as well in cases with more general sensor configurations.

In EEG, beamforming can be applied to implement a spatial filter that monitors the electrical activity in a certain brain region, while suppressing the contributions of interfering activity in other regions. The behaviour of a beamformer in terms of spatial response function and sensitivity to noise is completely determined by the choice of its coefficients for linearly combining the input signals.

Different types of beamformers exist, depending on the criteria put forward to determine their coefficients.

For instance, *linearly constrained minimum variance* (**LCMV**) beamformers [70] uses the following weight estimation for the source placed at location i:

$$\boldsymbol{L}_i = \begin{bmatrix} (\boldsymbol{L})_{0,(3i+0)} & (\boldsymbol{L})_{0,(3i+1)} & (\boldsymbol{L})_{0,(3i+2)} \\ \vdots & \vdots & \vdots \\ (\boldsymbol{L})_{M-1,(3i+0)} & (\boldsymbol{L})_{M-1,(3i+0)} & (\boldsymbol{L})_{M-1,(3i+0)} \end{bmatrix}$$

$$\boldsymbol{w}_i = \begin{bmatrix} (\boldsymbol{W})_{(\boldsymbol{3i+0}),\boldsymbol{0}} & & (\boldsymbol{W})_{(3i+0),M-1} \\ (\boldsymbol{W})_{(\boldsymbol{3i+1}),\boldsymbol{0}} & \dots & (\boldsymbol{W})_{(3i+1),M-1} \\ (\boldsymbol{W})_{(\boldsymbol{3i+2}),\boldsymbol{0}} & & (\boldsymbol{W})_{(3i+2),M-1} \end{bmatrix} \rightarrow [(L_i^T \cdot \boldsymbol{C}^{-1}) \cdot \boldsymbol{L}_i]^{-1} \cdot (\boldsymbol{L}_i^T \cdot \boldsymbol{C}^{-1})$$

Unlike ECD, beamforming does not require prior knowledge of the number of sources, nor does it search for a solution in an underdetermined linear system as does DECD.

For these reasons, beamforming remains the favourite method of many researchers in electromagnetic source imaging and has been suggested for use in the integrative analysis of E/MEG and fMRI.

2.3 fMRI source imaging

2.3.1 Neurovascular coupling and BOLD effect

Neuronal activity consumes energy, which is produced by chemical processes requiring glucose and oxygen. The vascular system supplies these substances by a complex network of large and small vessels.

A local increase of neuronal activity immediately leads to an increased oxygen extraction rate in the capillary bed and, thus, in an increase in the relative concentration of deoxygenated haemoglobin. This response of the vascular system to the increased energy demand is called the hemodynamic response. Still it is not completely known how the neurons inform the vascular system about their increased energy demand.

The most common method of fMRI is based on the Blood Oxygen Level-Dependent (BOLD) effect [71]. This exploits the fact that oxygenated haemoglobin has different magnetic properties to deoxygenated haemoglobin. More specifically, while oxygenated haemoglobin is diamagnetic, deoxygenated haemoglobin is paramagnetic altering the local magnetic susceptibility, creating a magnetic field distortion within and around the blood vessels in the capillary bed and venules. The BOLD effect, thus measures increased neuronal activity indirectly via a change in local magnetic field (in) homogeneity, which is caused by an oversupply of oxygenated blood.

Under the assumption of a linear time invariant (LTI) system, one can predict the expected time course of arbitrary long stimulation periods from the known impulsive response. In the fMRI context the impulsive response is the hemodynamic response function (HRF).

The data analysis of almost all fMRI studies is therefore based on the signals coming from the sustained positive BOLD response.

2.3.2 Statistical analysis of functional data: GLM

Statistical data analysis aims at identifying those brain regions exhibiting increased or decreased responses in specific experimental conditions as compared to other (e.g. control conditions). Due to the presence of physiological and physical noise fluctuations, observed differences between conditions might occur simply by chance. The statistical data analysis assesses the effect of noise fluctuations on estimated condition differences. In standard fMRI analyses this assessment is performed independently for the time course of each voxel. The obtained statistical values, one for each voxel, form a 3-D statistical map. In more complex analyses each voxel will contain several statistical values rejecting estimated effects of multiple conditions.

Without entering into details of such complex and advanced statistical methods, we will limit to cite the main analysis techniques used in this study: the general linear model (GLM). In a GLM analysis the data is processed voxel-wise (univariate) by fitting a model to the time course of each voxel independently

In order to effectively describe the method, let us first give a brief overview of few statistical concepts.

2.3.2.1 Statistical mean comparison

Statistical analysis essentially asks how likely it is to obtain a certain effect if there would be only noise fluctuations. This is formalized by the null hypothesis stating that there is no effect, i.e. no difference between conditions. Assuming the null hypothesis, it can be calculated how likely it is that an observed effect would have occurred simply by chance. This requires knowledge about the amount of noise fluctuations which can be estimated from the data. By incorporating the variability of measurements, statistical data analysis allows to estimate the uncertainty of effects (e.g. mean differences) in data samples. If an effect is so large that it is very unlikely that it has occurred simply by chance (e.g. the probability is less than p = 0.05), one rejects the null hypothesis and accepts the alternative hypothesis stating that there exists a true effect.

2.3.2.2 t Test

The uncertainty of an effect is estimated by calculating the variance of the noise fluctuations from the data. For the case of comparing two mean values, the observed difference of the means is related to the variability of that difference resulting in a t statistic:

$$t = \frac{\overline{X_2} - \overline{X_1}}{\hat{\sigma}_{\overline{X_2} - \overline{X_1}}}$$

The numerator is the mean difference while the denominator is the estimate of the expected variability, the standard error of the mean difference. Estimation of the standard error involves pooling of the variances obtained within both conditions.

The higher the t value, the less likely it is that the observed mean difference is just the result of noise fluctuations. It is obvious that measurement of many data points allows a more robust estimation of this probability than the measurement of only a few data points. The error probability p can be calculated exactly from the obtained t value using the incomplete beta function $I_x(a,b)$ and the number of measured data points N:

$$p = I_{\frac{N-2}{N-2+t^2}}\left(\frac{N-2}{2}, \frac{1}{2}\right)$$

If the computed error probability falls below the standard value ($p < 0.05$), the alternative hypothesis is accepted stating that the observed mean difference exists in the population from which the data points have been drawn (i.e. measured). In that case, one also says that the two means differ significantly.

2.3.2.3 Correlation Analysis

The described mean comparison method is not the ideal approach to compare responses between different conditions since this approach is unable to capture the gradual profile of fMRI responses. As long as the temporal resolution is low (volume-TR > 4 seconds), the mean of different conditions can be calculated easily because transitions of expected responses from different conditions occur within a single time point. If the temporal resolution is high (e.g., 2 seconds), the expected fMRI responses change gradually from one condition to the next due to the sluggishness of the hemodynamic response. In this case, time points cannot be assigned easily to different conditions. Without special treatment, the mean response can no longer be easily computed for each condition. As a consequence, the statistical power to detect mean differences may be substantially reduced, especially for short blocks and events.

To overcome this problem the *correlation analysis* is used, since this method allows explicitly incorporating the gradual increase and decrease of the expected BOLD signal. A predicted gradual time courses is used as the reference function in a correlation analysis. At each voxel, the time course of the reference function is compared with the time course of the measured data by calculation of a correlation coefficient *r*, indicating the strength of co variation:

$$r = \frac{\sum_{t=1}^{N}(X_t - \bar{X})(Y_t - \bar{Y})}{\sqrt{\sum_{t=1}^{N}(X_t - \bar{X})^2 \sum_{t=1}^{N}(Y_t - \bar{Y})^2}}$$

Index t runs over time points (t for “time”) identifying pairs of temporally corresponding values from the reference (X_t) and data (Y_t) time courses. The term in the denominator normalizes the covariation term in the numerator so that the correlation coefficient lies in a range of -1 and +1. A value of +1 indicates that the reference time course and the data time course go up and down in exactly the same way, while a value of -1 indicates that the two time courses run in opposite direction. A correlation value close to 0 indicates that the two time courses do not covary, i.e. the value in one time course cannot be used to predict the corresponding value in the other time course.

Since the reference function is the result of a model assuming different response strengths in the two conditions (e.g. “Rest” and “Stim”), a significant correlation coefficient indicates that the two conditions lead indeed to different mean activation levels in the respective voxel.

2.3.2.4 General linear model

The General Linear Model (GLM) is mathematically identical to a multiple regression analysis but stresses its suitability for both multiple qualitative and multiple quantitative variables. Because of its flexibility to incorporate multiple quantitative and qualitative independent variables, the GLM has become the core tool for fMRI data analysis after its introduction into the neuroimaging community by Friston et al. [72, 73]. In its general form, the General Linear Model has been defined for multiple dependent variables, i.e. it encompasses tests as general as multivariate covariance analysis (MANCOVA).

From the perspective of multiple regression analysis, the GLM aims to predict the variation of a dependent variable in terms of a weighted sum of several reference functions. The dependent variable corresponds to the observed fMRI time course of a voxel and the reference functions correspond to time courses of expected fMRI responses for different conditions of the experimental paradigm.

The reference functions are also called *predictors*, regressors, explanatory variables, covariates or basis functions. A set of specified predictors forms the *design matrix*, also called the *model*. A predictor time course is typically obtained by convolution of a condition box-car time course with a standard hemodynamic response function (two-gamma HRF or single-gamma HRF). A condition box-car time course may be defined by setting values to 1 at time points at which the modelled condition is defined ("on") and 0 at all other time points.

Each predictor time course X gets an associated coefficient or beta weight b, quantifying its potential contribution in explaining the voxel time course y. The voxel time course y is then modelled as the sum of the defined predictors, each multiplied with the associated beta weight b. Since this linear combination will not perfectly explain the data due to noise fluctuations, an error value e is added to the GLM system of equations with N data points and p predictors:

$$\begin{gathered} y_1 = b_0 + b_1 X_{11} + \cdots + b_p X_{1p} + e_1 \\ \vdots \\ y_N = b_0 + b_1 X_{N1} + \cdots + b_p X_{Np} + e_N \end{gathered}$$

Where the y variable on the left side corresponds to the data. After estimation (see below), the value of b_0 typically represents the signal level of the baseline condition, also called *intercept*.

While its absolute value is not informative, it is important to include the constant predictor in a design matrix since it allows the other predictors to model small condition-related fluctuations as increases or decreases relative to the baseline signal level. The other predictors on the right side model the expected time courses of different conditions. For multi-factorial designs, predictors may be defined coding combinations of condition levels in order to estimate main and interaction effects. The beta weight of a condition predictor quantifies the contribution of its time course in explaining the voxel time course. While the exact interpretation of beta values depends on the details of the design matrix, a large positive (negative) beta weight typically indicates that the voxel exhibits strong activation (deactivation) during the modelled experimental condition relative to baseline. All beta values together characterize a voxels “preference” for one or more experimental conditions. The last column in the system of equations contains error values, also called *residuals*, prediction errors or noise. These error values quantify the deviation of the measured voxel time course from the predicted time course, the linear combination of predictors.

In vectors and matrices notation, the last equation can be written as:

$$\boldsymbol{y} = \boldsymbol{X}\boldsymbol{b} + \boldsymbol{e}$$

Thus leading to a classic linear problem that can be solved in a least square sense.

2.4 EEG-fMRI integration

The integration of EEG/MEG and fMRI works under the hypothesis that the regions with the greater fMRI BOLD responses have a larger possibility of being electrically active over the time period of interest [74], [75], [68].

This hypothesis is reasonable in that neural activity, modulating neuronal firing and generating EEG signals, increases the demands for oxygen and induces larger cerebral blood flow and consequently produces larger fMRI responses [76].

Although at this time the physical and physiological basis that accounts for the correlation between fMRI signal and neural electrical activity is not yet well understood, a positive coupling between local hemodynamic response and electrical activity has been observed in both animal and human experimental studies [77], [78].

2.4.1 fMRI-constrained distributed inverse modelling

Reconsidering the diagonal WMN scheme in (2.37), one intuitive approach to insert information from fMRI is to “modulate” the diagonal entries not only with the depth of the source with respect to the channels, but also with local fMRI activity. For instance, BOLD percent signal change estimates α can be used to modulate by a flexibly variable amount k=1,2,…,10… the diagonal entries of R that correspond to location of significant BOLD-fMRI activity (in the sense of a main effect):

$$g(\alpha_i) = \begin{cases} 1 + (1-k) \cdot \dfrac{\alpha_i}{\max\limits_i(\alpha_i)} & significant\ BOLD \\ 0 & unsignificant\ BOLD \end{cases}$$

$$(\boldsymbol{R})_{ij} \rightarrow \begin{cases} g(\alpha_i) \cdot \|\boldsymbol{L}_i\|^{-2\gamma} & (i = j) \\ 0 & (i \neq j) \end{cases} \qquad (2.43)$$

2.4.2 fMRI-Guided Equivalent Current Dipole Fitting

The coupling between brain electrical activity and fMRI measurement suggests that one can use EEG to trace the time course of local neural activation revealed by fMRI.

The activation foci derived from fMRI images can be used to guide the placement of dipole locations, and the dipole orientation and strength are then fitted so as to best explain the observed bioelectromagnetic measurements over the time period of the relative neural process.

Modified from this procedure is a technique of “fMRI-seeded dipoles,” which only uses the fMRI foci as initial guesses (or seeds) for dipole locations and adjusts the dipole parameters using nonlinear optimization algorithms [79], [80].

In some cases, these techniques lead to a significant conclusion in resolving the timing details of localized activation and the interactions across different neuron assemblies that cannot be obtained when using fMRI alone. On the other hand, the fMRI-guided initial guess of dipole locations has largely alleviated the local minima problem inherent in nonlinear optimization procedures that may have been experienced in traditional multiple dipole fitting problems solely based on EEG or MEG.

Because the conventional fMRI techniques aided by these ECD-based approaches can provide additional temporal information beyond identifying the locations of neural activation, they have the potential to reveal the dynamic neuronal events, which can hardly be achieved by fMRI alone. However, these techniques are always limited by their inability to resolve complex spatiotemporally distributed activities, which are usually induced by a high-level cognitive task. When a large extent of neuronal network is active in parallel, the applicability of a simple dipole model would be questionable; or when a large number of different brain regions are involved, the nonlinear fitting procedure may fail to reach an optimal solution.

2.4.3 fMRI-Constrained Cortical Current Imaging

In order to account for the distributed nature of the neural sources inside the brain, fMRI has also been incorporated in the estimation of the continuous distribution of cortical current density. In this approach, fMRI data are used to bias the EEG/MEG inverse solution towards those locations deemed statistically significant in the view of fMRI [78], [75].

This can be implemented under different mathematical frameworks, such as:

1) in the context of the generalized Wiener filtering, which states that an optimal linear estimator can be derived given the covariance matrices of both source and sensor noise, fMRI spatial information is encoded into the diagonal elements of source covariance matrix [68], [75];

2) Based on the regularization strategy of generalized weighted minimum norm, one can set the weight matrix according to the fMRI significance, or p-value, to allow for the fMRI preference [74]. It is worth pointing out that these two frameworks are fundamentally equivalent, as we can see with the Wiener estimator

$$G = RL^T(LRL^T + C)^{-1} \tag{2.44}$$

where L is the lead field matrix, C the sensors noise covariance matrix, and R a source covariance matrix derived from fMRI activation maps. Since a voxel in fMRI must be either active or inactive, the fMRI-derived source covariance can be written as

$$R = R_f \cdot \lambda \tag{2.45}$$

where the diagonal elements of R_f are set to a positive value f only for those dipoles whose locations are deemed active in fMRI, while other diagonal elements are set to 1, and λ is a regularization parameter. The inverse operator as (2.45) is also the minimiser of a generic weighted minimum norm function

$$\Delta = \left\|C^{-\frac{1}{2}}(b - Ax)\right\|_2^2 + \frac{1}{r}\left\|R_f^{-1/2}x\right\|_2^2 \tag{2.46}$$

The parameter f controls the amount of bias towards fMRI active locations, which depends on the confidence in our hypothesis that neuronal and hemodynamic activities are collocated.

The regularization parameter r can either be determined by standard approaches like “L-curve” or be calculated if the noise covariance C is accurately estimated [81]. A further refinement of this technique is to quantitatively consider the reliability of source estimation with respect to the effect of sensor noise. Due to the linearity of both forward and inverse operators, the fMRI-constrained current density estimation can be normalized by the noise sensitivity, yielding unit-free dynamic statistical parametric maps (dSPM) of brain activity [68].

Furthermore, some of the latest advances have been made to estimate the connectivity patterns among different cortical regions of interest (ROIs) using the estimated cortical current density via directed transfer function (DTF) [82] or structural equation modelling [83]. Cortical connectivity estimation provides an important perspective regarding the causal relation and information flow pathways and, thus, specifically addresses how neuronal assemblies are activated and coordinated. Notably, a recent study on cortical connectivity estimation based on the combination of EEG and fMRI has been reported [82]. The high-density EEG as well as MRI/fMRI data were collected in separate examinations when the same subject was performing the same visually triggered finger-tapping task.

By using the linear inverse operator constrained by fMRI, the cortical current density was noninvasively estimated from EEG and then averaged to develop representative waveforms for preselected ROIs. DTF technique was applied to estimate the directional causality in various frequency bands among different ROIs, and the connectivity pattern was visualized in a subject-specific cortex reconstructed from MRIs

2.4.4 Multimodal Beamforming

Lahaye et. al. [84] suggest an iterative algorithm for conjoint analysis of EEG and fMRI data acquired simultaneously during an event-related experiment. Their method relies on iterated source localization by the LCMV beamformer, which makes use of both EEG and fMRI data. The covariance C_X used by the beamformer is calculated anew each time step, using the previously estimated sources and current event responses from both modalities.

This way neuronal sites with a good agreement between the BOLD response and EEG beamformer reconstructed source amplitude, benefit most at each iteration.

Although the original formulation is cumbersome, this method appears promising as (a) it makes use of both spatial and temporal information available from both modalities, and (b) it can account for silent BOLD sources using an electro-metabolic coupling constant which is estimated for each dipole and defines the influence of the BOLD signal at a given location onto the estimation of C_S which, in turn, drives the estimate of C_X.

2.4.5 EEG Source Analysis with EEG-fMRI Coupling

Exploring the signal coupling of simultaneously recorded EEG and fMRI time-series is attractive because fMRI signals can be automatically predicted (and fMRI patterns can be generated) directly from spatio-temporally selective EEG responses, thus improving accuracy in source localization [85].

2.4.5.1 Background

Modeling EEG-fMRI coupling effects entails with the extraction of integrated features from the EEG source responses, e.g. the EEG source power at a given latency or inside a given time or time-frequency interval. The resulting series of “EEG values” is then standardized across all trials and converted to a new time-course at the fMRI temporal resolution (TR). The conversion from this series of EEG measures to an fMRI predictor is performed in two steps: (i) hemodynamic convolution at EEG time resolution and (ii) time-course resampling at fMRI time resolution. The resulting time-course can be used for predicting and modeling, and, hence, localizing the joint fluctuations of EEG and fMRI signals.

2.4.5.2 Processing

The series of EEG values is standardized (i.e. the mean is subtracted and the values are scaled to their standard deviation) and convolved with the double gamma hemodynamic function estimated at the EEG time resolution and resampled at the fMRI time resolution. Assuming a series of N EEG values (corresponding to N EEG epoch-specific measures, either from stimulus or fMRI triggers) and a series of K fMRI values (corresponding to T fMRI time points), the EEG-fMRI coupling time-course can be easily expressed as a discrete time convolution:

$$y(k) = \sum_{n=1}^{N} EEG_n \cdot HRF(t_k - t_n) \qquad k = 1{,}2 \ldots \ldots K$$

Where:

EEG_n is the integrated measure corresponding to the n-th trial

t_n is the time of n-th trial trigger (with respect to the EEG segment)

t_k is the time of the k-th fMRI trigger (with respect to the EEG segment)

$HRF(t)$ is the hemodynamic response function

Hemodynamic convolution at the original EEG resolution is necessary because the stimulus or any other EEG trigger of interest is normally not synchronized with all fMRI time points, with the sole exception of the fMRI trigger itself. On the other hand, even if the fMRI trigger is used to extract EEG values, the long fMRI repetition time (normally 100:1000 times longer than the EEG sampling period) may suggest using different subintervals within each TR with the result of introducing a time shift between the trigger event and the actual EEG measure.

2.4.5.3 Experimental note

When analyzing simultaneous EEG-fMRI data, there are two alternative approaches for extracting the series of EEG values to be used in the prediction and modeling of the fMRI data: single-trial coupling and continuous coupling. Single-trial coupling entails with extracting EEG features from each single-trial response (e.g. the power at a certain latency or inside a given time-frequency box) with respect to the stimulus trigger; these values are assumed to be capable of modulating the amplitude of the event-related fMRI response to that stimulus. Continuous coupling entails with integrating the EEG power inside a certain time-frequency box defined with respect to the fMRI trigger. In general, the choice between these two approaches is implicitly driven by the experimental design.

In event-related designs a single EEG trigger of a given protocol condition is associated with the occurrence of single experimental stimulus whose duration is assumed to be zero (i.e. an impulse). Assuming that the absence of a stimulus implies the absence of a neuronal response and, vice versa, the presence of a stimulus implies the presence of the fMRI response, the EEG-fMRI coupling for that condition can be studied directly from single-trial data (STD/TFD) prepared for that specific stimulus.

In block-design experiments a single stimulus trigger only defines the onset or the offset of a block (or, equivalently, the borders of a data segment). In this case, the fMRI trigger should be used and an integrated EEG measure (e.g. the total power in a given frequency band) is calculated for each TR. More in general, this approach is preferred in all cases where EEG-fMRI correlations are studied for long periods corresponding to entire segments rather than short trials of EEG data (e.g. resting-state, free viewing or listening, etc.).

3 Comparative analysis of different head modelling approaches in EEG-based functional neuroimaging

3.1 Aim of the study

So far, it is not yet clear which brain regions are more sensitive to the choice of different model geometry, both from quantitative and qualitative point of view. In order to address this issue and avoiding the intrinsic uncertainties related to the particular inverse method adopted [67], we propose a comparison between the effects that different modelling approaches directly give on the forward fields [44], [34]. One is the anatomically-shaped modelling approach, the other is the well known multi-layer spherical geometry approach. This knowledge would allow determining whenever the spherical approximation shall meet the required accuracy for the EEG current sources under investigation. In order to achieve as much generality as possible, we based our study on the MNI152 template, since it is derived from an average of several healthy humans head MRIs; hence the inferred considerations shall be widely applicable [59]. Starting from real magnetic resonance imaging (MRI) high-resolution anatomical images we explore the spatial variation of the forward fields, directly basing on the analysis of the lead fields [34] produced by simulated cortical sources placed on the reconstructed mesh of the neocortex along the surface electrodes of a 62-channel configuration.

We first proposed a comparison between realistic and approximated geometry, whose results have been published in [6], then we decided to deepen the study including two distinct approaches of realistic modelling [7]

3.2 Sensors and sources

We started considering a typical 62-channel EEG electrode configuration, with one more electrode acting as reference (Figure 3-1 on the right), and a brain cortex surface from the averaged MNI head and brain image dataset (Figure 3-1 on the left), subsampled to 5000 vertices. The latter will be referred to as our *source space*, i.e., the surface the vertices of which are all possible source positions. The three orthogonal dipole orientation axes are directed as follows: right-left (*x* axis), frontal-occipital (*y* axis) and bottom-up (*z* axis).

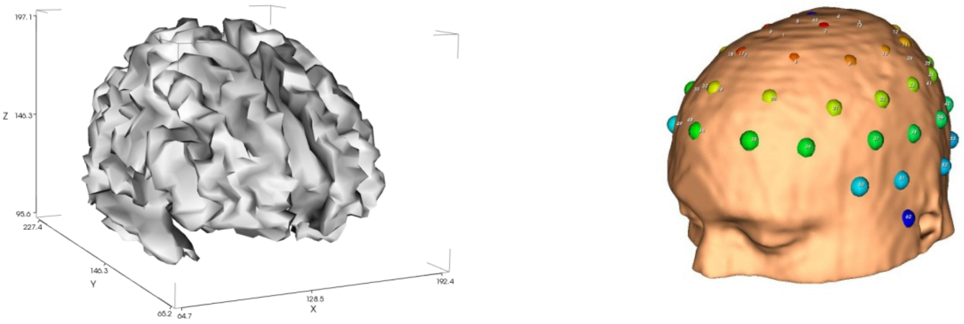

positions on

3.3 Building of the MNI-template-based realistic model

We aimed to develop a generic realistic geometry template that could be helpful in EEG source analysis even when only EEG and no specific MRI data are available for a particular subject, or the acquired dataset was not suitable for segmentation. In these cases, a lead field computation performed on this model and based on the real EEG sensors locations can be used to perform source analysis.

A realistic-shaped FDM volume conductor model of the head was derived from an averaged T1-weighted MRI dataset, available from the Montreal Neurologic Institute (http://www.mni.mcgill.ca/).

Segmentation by BrainSuite analysis tool (http://brainsuite.usc.edu/) was used to identify the following five tissue types in the head: scalp, skull, cerebrospinal fluid (CSF), gray matter, and white matter (see Figure 3-2).

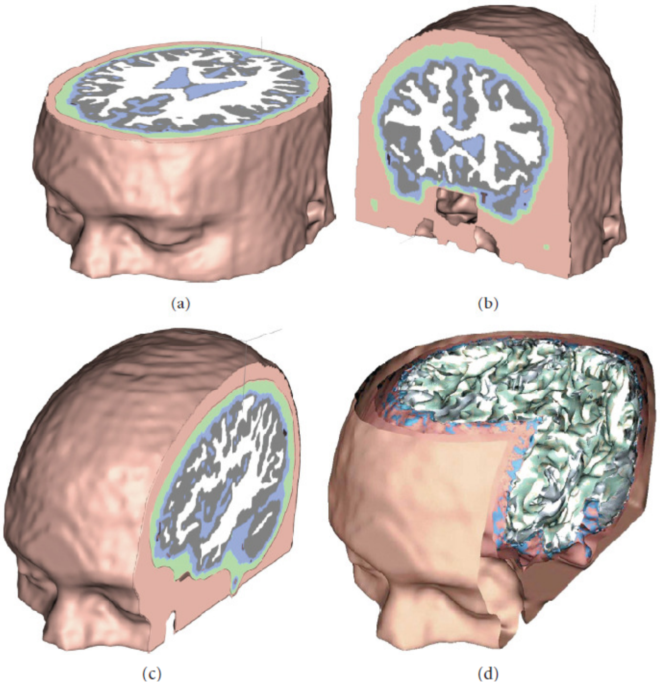

Figure 3-2(a), (b), and (c): *Realistic FDM model based on the MNI anatomy composed by four compartments representing scalp (pink), skull (green), CSF (blue), and brain, given by fusion of grey matter and white matter. (d): The complete 3D model, with rendered surfaces.*

In addition to the standard three compartments of scalp, skull, and brain, the CSF layer has been considered as it plays an important role in modifying the scalp potentials and can also influence the inverse source localizations [86] .

Based on literature [87], we set the homogeneous isotropic conductivities as σ = 0.33 S/m (skin), σ = 0.0042 S/m (skull), σ = 1.0 S/m (CSF), σ = 0.33 S/m (GM), and σ = 0.14 S/m (WM), respectively

Moreover, aiming to assess the influence that tissue anisotropy has on EEG forward modeling, we proceeded in characterize white matter and skull bones tissue conductivity tensors. The following paragraphs will describe the overall implemented process to build an anisotropy template for white matter and skull bones.

3.3.1 Workflow overview

The following key points briefly summarise the steps necessary to build the template, before describing each step in detail:

- Selection of DTI datasets
- Pre-processing:
- Eddy currents correction for all subjects
- Brain Extraction Tool (BET)
- Extraction of DTI components (DTIFIT)
- Application of VBM-style process for gray matter alignment
- Application of TBSS-style process for white matter alignment
- Application of TBSS-style NON FA process for computation of eigenvalues of final template
- Implementation of vectorial registration and alignment procedures preceding averaging to calculate the eigenvectors of the final template
- Computation of diffusion tensor matrices

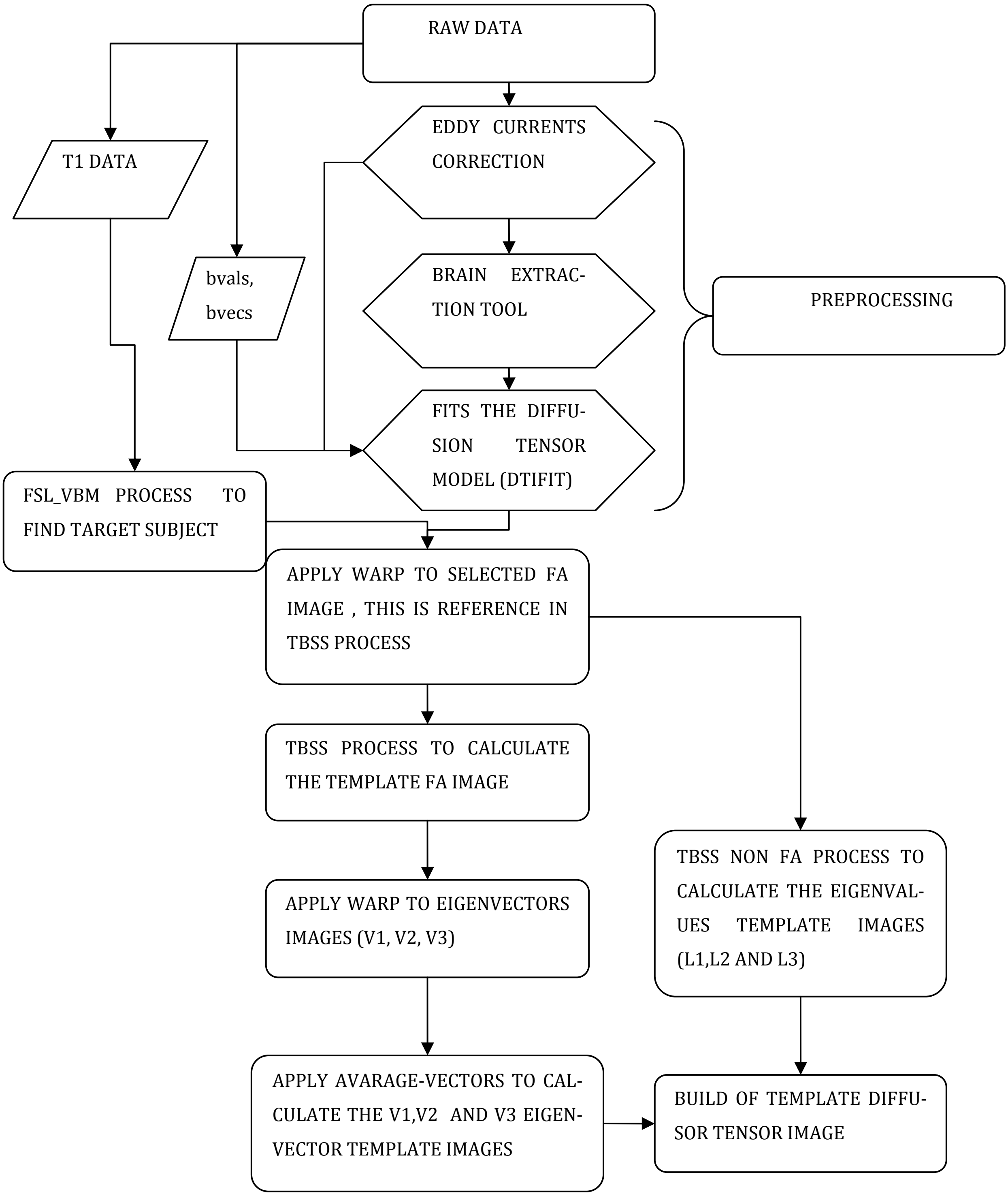

As the conductivity tensors are assumed to share the same eigenvalues and eigenvectors of diffusion tensors, we start considering the diffusion tensors analysis

Most of the mentioned steps have been performed using the FSL software package [88], [89] which includes many DWI/DTI processing tools.

3.3.2 DWI Data

The data sets used in this work have been made available by the John Hopkins University Medical Institute, Laboratory of Brain Anatomical MRI, with a DTI database which has been developed under the Human Brain Project and National Research Resource Center grant. We used a group of twenty raw DTI datasets of normal population; each of them is composed by three studies with the same acquisition protocol. The data are anonymous with the following imaging characteristics:

All dataset have been acquired by means of a 1.5 T Philips MRI scanner			
Scan mode	Multiple slice		
Number of slice	50		
Scan resolution (x, y)	96	96	
Recon resolution (x, y)	256	256	
FOV (ap,fh,rl) [mm]	240.00	125.00	240.00
Slice thickness [mm]	2.50		
Slice gap [mm]	0.00		
Data Format	Analyze		
Gradient directions	35		
B value [s/mm^2]	700		

3.3.3 Voxel Based Morphometry procedure

Once artefacts (eddy currents and head motion) correction have been carried out, we applied DTIFIT tool to fit the diffusion tensor to each voxel, thus obtaining L1, L2, L3 (the eigen values), V1, V2, V3 (the eigenvectors) that fully describe each tensor.

In order to align all the Grey Matter (GM) images, these need to be first transformed into a standard space, which involves the use of non-linear registration. This approach is somewhat of a trade-off: all the cortex morphologic features across subjects are desirable to match, but not "too much" or one would not be able to see any difference, if all these structures were perfectly aligned across the subjects. That's why we use limited degrees-of-freedom for the non-linear registration.

Structural data have been analysed by means of FSL VBM-style analysis facilities, which perform brain-extraction of structural images applying BET, and tissues segmentation with the FAST tools provided by FSL.

The resulting grey-matter partial volume images were then aligned to MNI152 standard space using the affine registration tool FLIRT, followed by nonlinear registration using FNIRT towards the GM-ICBM-152 template.

3.3.4 Target subject and template determination

At the end of the process described above, we use the information pertaining to the warp matrices for selecting the subjects' reference. We have a number of related files that is equal to the number of subjects; these files are characterized by two important parameters: the mean of the squared mean values across the three images of warp volume (computed on non-zero voxels) and the percentile of 50% of the squared mean values across the three images of warp volume (that is the median). We use this information to select the best target subject. The warp files are then compared to find the target that requires the minimal changes to get warped into the MNI standard space (with reference to GM-ICBM 152), i.e., the subject more similar to the MNI template.

Once identified the best target subject, in the second part of the code, the same warping to standard space is applied on best target subject's FA maps.

Finally, this results in the target image, that we call *TEMPLATE_FA,* in the final standard space.

3.3.5 Application of Tract Based Spatial Statistics (TBSS)

Voxelwise statistical analysis of the FA data was carried out using TBSS (Tract-Based Spatial Statistics, [90]), part of FSL [89].

First, FA images were created by fitting a tensor model to the raw diffusion data using FDT, and then brain-extracted using BET. All subjects' FA data were then aligned into the common space *TEMPLATE_FA* using the nonlinear registration tool FNIRT, which uses a b-spline representation of the registration warp field. Hence, the warp matrix obtained projects each subject's data into the MNI152 space. This warp matrix will be later applied to the eigenvectors images.

Next, the mean FA image was created and thinned to create a mean FA skeleton which represents the centres of all tracts common to the group.

Each subject's aligned FA data was then projected onto this skeleton and the resulting data fed into voxelwise cross-subject statistics.

Finally, we threshold the skeleton images to create a mask, and create a skeleton distance map projecting all FA data onto the skeleton. FA data have been threshold at 0.2.

We applied this technique also to each eigenvalues map and then averaging the results across the subjects in order to obtain the eigenvalues template.

3.3.6 Eigenvectors estimation

The final step of the overall process consists in estimating a sort of vector averaging across the subject's eigenvectors maps previously computed.

First, the warping matrix computed during the previous FNIRT processing is applied to warp all the eigenvectors towards the “best target”. Then, a second transform warps the vectors to the FMRIB58 model into MNI152 space.

Eventually, with all the vectors in template standard space, we can estimate the mean value of eigenvectors for each voxel by averaging, estimating their orientation’s mode. Since in each voxel of the final image the eigenvectors orientations of all subjects must be taken into account and since all of them can reasonably be assumed affected from noise, especially in the non-white-matter voxels, a simple vectors averaging could lead to poorly reliable results. This is why the mode (across the subjects) of the orientations of each eigenvector has been taken into account. Figure 3-3 illustrates the FA image with the usual color-coding referred to the first eigenvector:

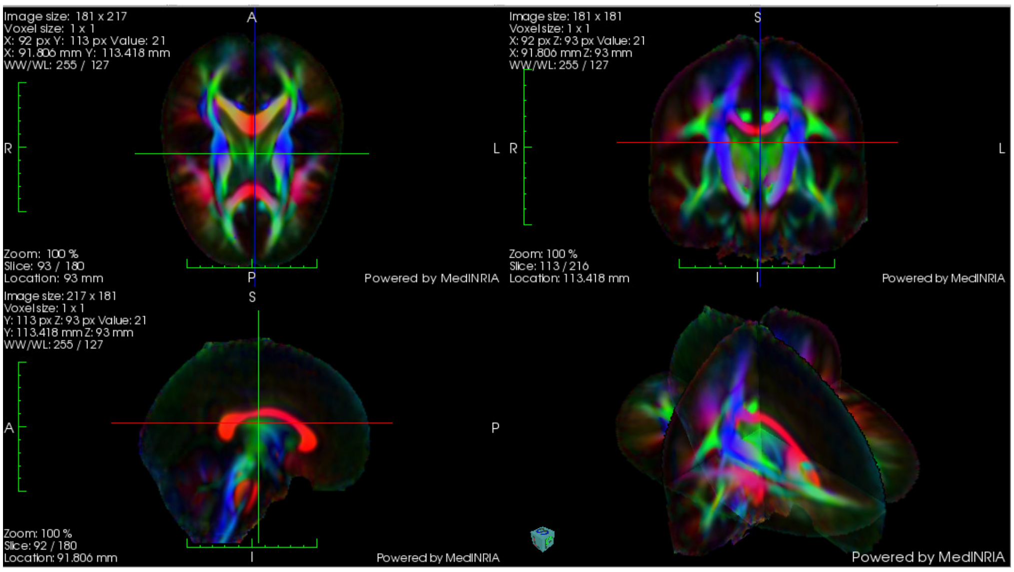

Figure 3-3 FA image with V1 color-coding, tri-axial view

3.3.7 From conductivity tensors to diffusion tensors

As already stated DT-MRI doesn’t measure conductivity tensor directly but rather infers from the diffusion tensors which describes the movement of both water molecules and electrically charged particles (ions).

To implement conductivity tensor we assume that the same structural features that result in anisotropic mobility of water molecules also result in anisotropic conductivity. In other words the eigenvectors of the conductivity tensor can be considered similar as those from water diffusion tensor

Furthermore the eigenvalues can be estimated from the isotropic conductivity by means of two constraints, whose effectiveness has been proven in white matter anisotropy measurements:

$$\begin{cases} \frac{4}{3}\pi\sigma_{long}\left(\sigma_{long}\right)^2 = \frac{4}{3}\pi\sigma_{iso}^3 \\ \sigma_{long}\cdot\sigma_{trans} = \sigma_{iso}^2 \end{cases}$$

They are called *volume constraint* [87] and *Wang’s constraint* [91], respectively.

Figure 3-4 below shows the result of the white matter conductivity tensor imaging:

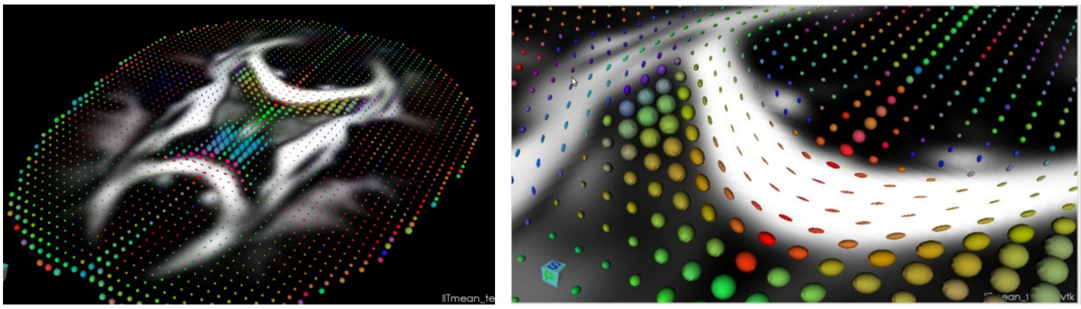

Figure 3-4 Conductivity tensor imaging. Left: axial view, Right: detailed view. The image in background is the FA image

3.3.8 Skull conductivity anisotropy

Realistic modelling of the conductivity tensor eigenvalues in the skull is a difficult task, not only because the absolute and relative thicknesses of spongiosa and compacta layers vary and their boundaries are difficult to segment, but especially because of inhomogeneous skull resistivity and an inter- and intrasubject variability which can be related to age, diseases, environmental factors, and personal constitution [92], [93].

We therefore started from the commonly used isotropic conductivity value of skull = 0.0042 S/m [94], and assumed a given anisotropy ratio $\sigma_{\mathrm{long}}: \sigma_{\mathrm{trasv}} = 1: 10$ according to [93], [66], [25]. Next we applied Wang's constraint which has been proven to lead to smaller errors, according to [87].

3.3.9 Effects of anisotropy in Lead Field computation

In order to assess the effects that conductivity anisotropy has on the forward modelling, we directly cross-compared four LF matrices, one of them based on an fully-isotropic modelling, and the other computed with a different anisotropy characterization (white matter only, skull only, both), by means of a correlation of the LF values (see section 3.6.3).

The first two models compared to the isotropic one present anisotropy characterization either of the only white matter conductivity, or the only skull bones conductivity. These two results are illustrated in Figure 7-10a and Figure 7-10b, respectively.

In the third case a model featuring both white and skull conductivity anisotropy has been introduced and compared to the isotropic model and the resulting correlation map reported in Figure 7-10c.

3.4 Spherical modelling approach

As described in 2.2.3.1, we built a sensors fitted spherical head model, which does not require any sensors projection on the outer sphere surface, preventing the unknown effects of differences in the sensors set on the lead fields comparison.

Basically, for each i^{th} electrode located in $\mathbf{r}_{ei}$, the outer sphere surface is built by imposing two constraints: the passing through $\mathbf{r}_{ei}$, and the minimization of the mean distance between the surface itself and the other sensors. Thus, with these constraints, the external sphere can be derived and it will be completely described by its radius and its centre c. Then, the inner shell is the following model compartment that will be built: while it shares the same centre c as the external one, its radius must be slightly greater than the distance between the source and c, i.e., the inner sphere has to strictly include the current dipole source (otherwise convergence issues in the Legendre polynomials approximation will occur). Finally, the remaining shells, all sharing the same centre c, will have appropriate radii depending on pre-defined proportion constants, according to Table 3-1. Then, each layer is been assigned the same isotropic conductivity value $\sigma_{\_iso}$, as in the following table:

Model compartment	Scalp	Skull	CSF	Brain
Relative radius	1	0.95	0.87	0.84
Conductivity σ_{iso} (S/m)	0.33	0.0042	1.79	0.33

Table 3-1 Parametrical setting of the adopted 4-shells spherical model: for each model compartment, the relative radius and the conductivity value are listed. The compartment's relative radii are given by the ratio between the radius of the model compartment and the radius of model's outest layer (i.e., the scalp)

The number of adopted layers has been set to 4, considering a trade-off between reality coherence and model complexity: scalp, skull, CSF and brain are the regions with the most different isotropic conductivity values

A representation of this model is show in Figure 3-5

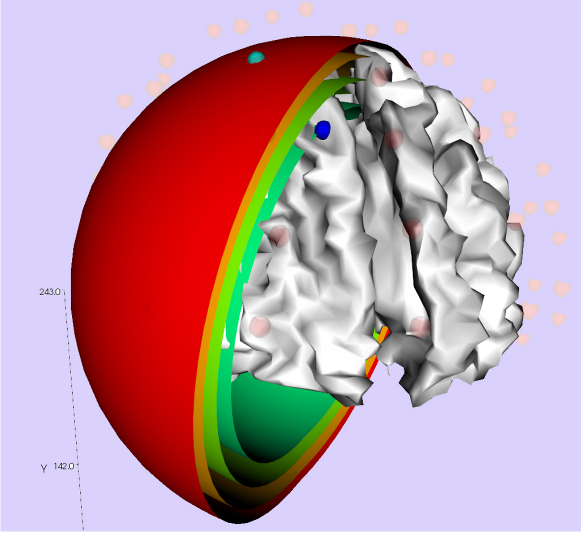

ntation

3.5 BEM modelling approach

For the comparative study, using the same segmentation results, a four-shell BEM head model has been built with the *BrainStorm* toolkit (http://neuroimage.usc.edu/brainstorm/), computing the linear Galerkin algorithm [41], after resampling each surface mesh from the original tessellation to 1500 vertices.

3.6 Comparison methods

With reference to the notation introduced in 2.2.2.2, there have been proposed [6] three methods for assessing the performances of the models relative to the forward problem solution. In this section they will be introduced.

From now on, we will refer to the set of values *V(1, j)..V(i,j)...V(n, j)* as the generic *j_th* column of the LF matrix **L** with the symbol $\boldsymbol{V}_j$, regardless of the dipole orientation

3.6.1 Point Spread Function (PSF) analysis

Due to the linearity of the forward problems, a measure of estimation error defined as “point spread function” (PSF) [68] can be calculated for each source location. In detail, 5000 evenly spaced points on the brain cortex mesh were initially considered as possible source positions, while 26 "true" source positions have been placed in specific vertices of this mesh (see Figure 3-6). The 26 source positions have been selected in order to achieve a rather uniform spatial sampling of the source space, with the aim of investigating the main differences that can be observed in terms of source reconstruction for the various cortical regions in the spherically approximated and in the realistic model. Given the *i* th source, for each point of the cortex mesh, the correlation (*corr*) and relative difference (*rdm*) [65] between the coefficients $\mathbf{V}_i$ (i = 1…26) and $\mathbf{V}_j$ (j = 1….λ) are computed, as a measure for the divergence between the two lead fields. Thus, denoting with $PSF(\vec{r}_{s,j})$ the function evaluated at point $\vec{r}_s$, if the actual source is located in $\vec{r}_j$, its value is defined as follows:

$$PSF(\vec{r}_{s,j})_{rdm} = 100 \times \sqrt{\frac{\sum_{i}^{n}\left(V_s - V_j\right)^2}{\sum_{i}^{n} V_j^{\,2}}}$$

$$PSF(\vec{r}_{s,j})_{corr} = \frac{c_{1,2}}{\sqrt{c_{2,2} \cdot c_{1,1}}}$$

$$\text{where } c_{m,n} \in Cov\left(V_s, V_j\right) = \begin{pmatrix} c_{1,1} & c_{1,2} \\ c_{2,1} & c_{2,2} \end{pmatrix}$$

A map is hence created, evidencing how sharp (or how smooth) the PSF decreases spatially from the point *j*. The PSF specifies the ratio of the energy that arises from the actual current dipole at a given location but spreads onto the estimates at all other locations to the energy that only contributes to the source estimate at the same location.

Given its definition, the PSF function specifies a measure of the spatial blurring of the true activity at any given position. Therefore, a location with lower PSF is expected to have a smaller spatial extent and higher source estimation accuracy [95]. The comparison of the PSF maps obtained from the two

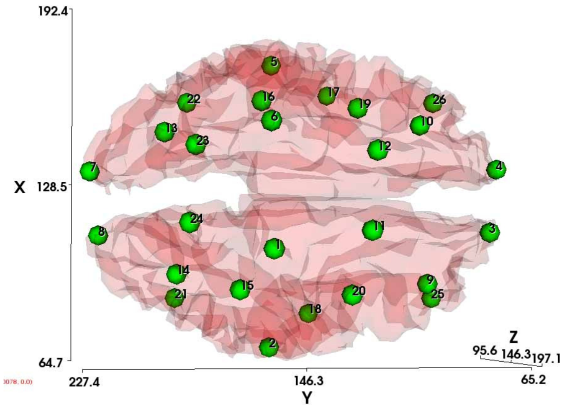

Figure 3-6 Location of the 26 sources used for the cortical PSF map calculations

modelling methods would then indicate which of them appears to be more specific.

3.6.2 Full width at half maximum (FWHM) parameter

In order to quantitatively describe the behaviour of each of the PSFs along the surface versus the distance between the source and each vertex, we first fit the map values with the best Gaussian-like function, then compute its FWHM parameter, for both PSFs. Figure 3-7 shows the PSF values sorted by distance from a certain source and the corresponding best-fitting function (bi-exponential Gaussian).

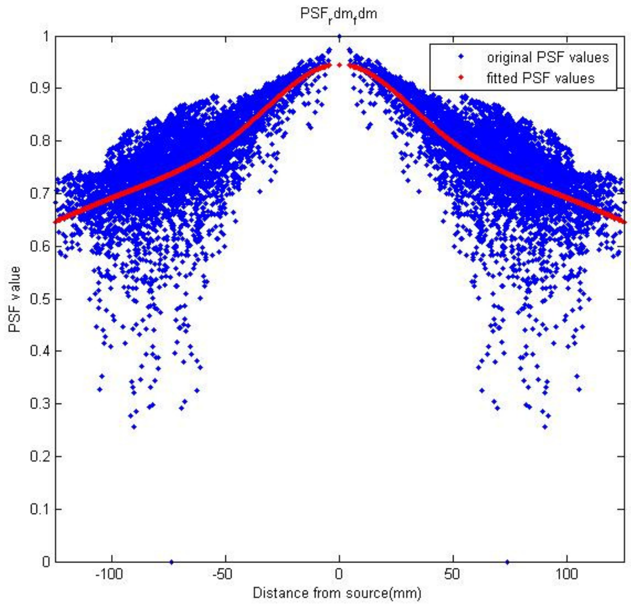

Figure 3-7 Example of PSF(corr) values distribution, normalized with respect to their maximum, plotted versus the distance from the source, and fitted by a bi-exponential Gaussian curve. Negative distance values have been introduced by mirroring the positive distance values to perform the Gaussian fitting

3.6.3 Mutual Correlation (MC)

The differences between the two forward models can be evaluated by computing the correlation coefficients between the correspondent lead fields elements. Effectively, mutual correlation can be computed between one row of the LF matrix for the spherical model and the corresponding one in the LF matrix for the realistic model. Correlation between the *i*th rows of two different LFs will indicate how the *i*th electrode is differently affected by the forward field in different head models. This computation is then iterated for each row of the lead field matrices (i.e., for each electrode), thereby gathering an electrodes map. Alternatively, correlating the *j*th column of the LF for the spherical model with the corresponding *j*th column of the LF for the realistic one, a value will be obtained representing how the contribution of the *j*th vertex to the EEG signal measured at the electrodes differs among two different models. Again, reiterating this process for all the columns of the LF matrices (i.e., for each mesh vertex in the source space), will result in a cortex map.

3.7 Comparative analysis of different modelling approaches: spherical spherical vs. realistic geometry

3.7.1 PSF maps

For each of the 26 selected sources, we computed the PSF values, basing on both *rdm* and *corr* formulations, over the whole cortex mesh. These calculations produced a series of 3 maps for each source position, according to each source orientation, thus obtaining 78 maps for each PSF parameter, *corr* and *rdm,* totalling 156 maps. Figure 7-1 and Figure 7-2 present an example of the obtained results for the PSF(*rdm*) and PSF(*corr*) parameters for the realistic and spherical models, considering source number 5, placed in the temporal cortex, oriented parallel to *y*-axis.

To quantitatively compare, for the different head models, the spatial characteristics of the PSF maps at any given source position, the mean, minimum and maximum values of the obtained PSFs have been reported and compared for all the 78 analyzed dipole sources, for either the realistic FDM or the sensor-fitted spherical models. Table 8-1 and Table 8-2 summarize the quantitative results of the performed analysis on the PSF maps for the PSF(*rdm*) and PSF(*corr*) parameters respectively. Table 8-1 and Table 8-2 aim also to evidence how sensitive is the PSF to dipole's orientation and position.

3.7.2 Extended FWHM values maps

These results are reported in Table 8-1 and Table 8-2, together with an evaluation of the differences in terms of FWHM between the realistic FDM and the sensor-fitted spherical models. The reported differences have been evaluated by subtraction of the FDM FWHM parameter to the spherical FWHM. Positive values in the *diff* columns in Table 8-1 and Table 8-2 indicate a smaller spatial extent and hence a higher source estimation accuracy for the FDM realistic model with respect to the sensor-fitted spherical model.

In order to gather a broader evaluation of the PSF behaviour on the overall brain cortex, we extended the evaluation of the PSF to all the 5000 points of the cortex surface. Even though the relationship between the PSF values and the specific source location results less self-evident, following the large number of sources considered, this evaluation is able provide a quantitative overall cortex estimation of the FWHM parameters distribution. These results are shown in Figure 7-3, related to the PSF based on the RDM parameter, in which the overall separate behaviour of the different *x*-, *y*- and *z* source orientations in the spherical and realistic models has been evidenced, also with reference to the *x*, *y*, and *z*-positions of the vertices. The extended evaluation of the PSF function based on the cross correlation parameter shows a rather similar behaviour, shown in Figure 7-4. It is worth underlining that Figure 7-3 and Figure 7-4 show the FWHM values with three different dipole orientations. Each of these plots can be rearranged in terms of the *x*, *y*, or *z* coordinates of the dipole positions (i.e., the vertices of the source space). As specified in the figures' captions, each row reports the three plots for the three different source orientations, arranging the values by each of the three components of the dipole positions.

However, still remains the importance of considering a root mean squared (RMS) superposition of the effects given by the three dipole orientations, in order to gather a broader vision of the PSF behaviour. Figure 7-5 and Figure 7-6 present the RMS values of the previous distributions.

These results support the findings about the effects of source eccentricity on modelling errors reported in [96], since an increasing trend of the FWHM values is evident with the decreasing of source eccentricity. They also suggest that the smaller the eccentricity, the less precise our spherical forward model will be, in comparison to the realistic one.

3.7.3 MC maps

Figure 7-7 depicts the mutual correlation values between realistic and spherical lead fields. In the right panel of Figure 7-7 the colour-coding of the electrodes indicates the correlation between spherical and realistic lead fields related to the same electrode, obtained by computing the mutual correlation over each row of the lead field matrices.

3.8 Evaluation of effects led by model geometrical differences

The investigation of the dissimilarities between the forward field simulated for a spherically approximated and a realistic head model has been carried out on standard real cortex geometry by means of a direct analysis of the lead fields. Starting from these, the Point Spread Function (PSF) has been used to quantify the amount of spatial blurring of simulated cortical activity effects. The obtained results showed in many cases relevant differences between the realistic and the sensor-fitted spherical models when applied to the same source space (cortex) and generally indicated the presence of a more pronounced spatial blurring for the latter model, as evidenced by a broader extent of higher PSF values with respect to the same source in the realistic FDM model. A quantitative comparison of the spatial characteristics of the PSF maps for many pre-defined source positions is reported in Table 8-1 and Table 8-2 for the two models. The reported PSF values generally indicate a smaller extent, and hence a clear improvement, for the FDM realistic model in comparison with the sensor-fitted spherical model. By inspection of the *diff* columns reported in Table 8-1 and Table 8-2, the realistic FDM model presented an improvement of more than 5 mm in the FWHM respectively for 82% and 76% of the analyzed sources for the PSF(*corr*) and PSF(*rdm*) parameters respectively, and limited to 5 mm for the 6% (*corr*) and 3% (*rdm*) of the sources. A limited worsening within 5 mm was presented by 4% (*corr*) and 9% (*rdm*) of the sources, whereas 8% (*corr*) and 13% (*rdm*) of the sources presented a worsening of more than 5 mm in FWHM values.

An interesting behaviour can be observed for sources 3 and 4 (see Figure 3-6 and the corresponding values in the diff columns in Table 8-1 and Table 8-2), for which the FDM FWHM results larger than the corresponding spherical FWHM. Sources 3 and 4 are both positioned in the frontal cortex in proximity of the paranasal sinuses, which are actually filled with humid air but are nonetheless modelled as compact bone in our realistic model, in order not to introduce a fifth compartment. While in the corresponding spherical model the skull compartment is modelled by a spherical layer of uniform thickness, the above cited presence of the paranasal sinuses in the realistic model is thought to be a possible cause for this blurring effect that has been found in the corresponding PSFs. To test this hypothesis, sources 9 and 10 (see Figure 3-6) have been selected on the cortex mesh, placed laterally with respect to sources 3 and 4 and to the paranasal sinuses, with the resulting positive effect of improvement in terms of spatial blurring given by the realistic model for these source positions.

A confirmation of this behaviour has been obtained with sources 25 and 26, which are also anatomically located laterally with respect to sources 3 and 4, in proximity of sources 9 and 10 but in a lower position (see Figure 3-6), and exhibited an analogous positive effect of improvement in terms of spatial blurring. Results for sources that are placed in the temporal cortex (namely 2 and 5, 15 and 16, 17 and 18, 19 and 20) indicate that adopting the realistic model always leads to an improvement in terms of spatial blurring; these results are in agreement with previous studies that showed that a 3-compartment realistic BEM model of the head performed better than a 3-shell spherical model, particularly in the temporal lobe [45] . This trend is also confirmed for sources which are positioned in the occipital cortex, namely 7 and 8, 13 and 14, 21 and 22, 23 and 24, again demonstrating that the adoption of a realistic model can lead to benefits in terms of power of discrimination for the reconstruction of these sources. For two sources, 7 and 8, the realistic model leads to a good improvement for the PSF(*corr*) parameter, but the same does not apply for the PSF(*rdm*) parameter; this behaviour might probably be due to the small curvature of the skull near these source positions and needs to be carefully tested in future work investigating similar and different source/skull relative conditions. Similar effects are presented by sources 1 - 6 and 11 - 12.

MC maps confirm that the FDM lead fields mainly differ from those of the spherical models in frontal cortical areas, as represented in Figure 7-7, in which a lower mutual correlation has been found for these brain areas. It is also evident that, in spite of the relatively high correlation coefficients distributed along the surface, the overall effect of the LF mismatch on some of the electrodes is often greater than expected. For instance, the LF dissimilarities are negligible on some of the parietal areas. Conversely, the sensors that appear to be strongly affected by the spherical approximation are those nearest to the temporal lobes, where the correlation values decrease down to 0.2 and lower. However, this aspect is due to the specific 62-channel configuration used here and can be improved by using more channels through the scalp.

The obtained results present a high symmetricity of the PSF maps over the two hemispheres, as it could be expected within the geometrical similarity of the two hemispheres. The PSF (*rdm*) maps derived from the realistically shaped model presented a reduced amount of spatial local minima (see Figure 7-1) in all the analyzed situations. Moreover, for sources located in temporal and parieto-occipital areas (see Table 8-1 and Table 8-2 for sources n. 13-17 and 21-24 in Figure 3-6), both PSF parameters exhibit smaller FWHM for the realistic model, compared to the spherical one. Since RDM is a measure commonly used in most of the source localization algorithms [97], this implies that the lead fields computed on realistic geometry would give better performances in localization accuracy and convergence stability than those obtained adopting spherical models.

The reported findings are hence expected to lead implications also from the point of view of the localization error of neural brain sources which would occur when using realistically shaped head models instead of spherical models in EEG inverse problem solution, independently of the specific adopted head model. Although PSF maps considerably depend on dipole orientation, it should be noted that during source localization procedures actual source orientation is clearly not known *a priori*, and for this reason also the RMS values of the FWHM distributions over the three directions are presented, to give more general results (see Figure 7-5 and Figure 7-6). Finally, the greater the source eccentricity, the sharper the PSF(*rdm*). This confirms previous findings by Finke et al. [96] that the RDM in source localization increases with source eccentricity, with an effect markedly larger for the spherical head model.

The presented results confirm also the findings of previous work [86], [98], [99] on the influence of head models on EEG simulations and inverse source localizations, according to which the structure of the anatomical surfaces, e.g., CSF and gray and white matter, could severely influence the flow of volume currents in a head model, and in turn also influence the scalp potentials and the inverse source localizations. According to [98], as the CSF layer plays an important role in modifying the scalp potentials and is also able to influence the inverse source localizations, the two different realistic and spherical four layers head models that have been adopted in this study consider also the presence of the CSF model compartment.

Finally, the same analysis method presented in this work is also well suited to be performed on further investigations with other and more complex model uncertainties, as anisotropic conductivities, in order to point out which brain regions are more sensitive to the choice of an increased volume conductor model complexity.

3.9 Increasing model complexity: comparative analysis of the three different modelling approaches

We enriched the previous study with a deeper analysis based on the same measurements now performed on two different realistic model algorithms, BEM and FDM, and the same spherical model.

3.9.1 PSF maps

The PSF maps on the cortex mesh have been computed for each source location and orientation for a total of 78 PSF maps for the realistic and the spherical head models. The visual inspection of the PSF maps allowed a qualitative evaluation of the spatial blurring of the true activity at the considered source position for the specific head model. The obtained results showed in many cases marked differences between the realistic and the sensor-fitted spherical models when applied to the same source space (cortex) and generally indicated the presence of a more pronounced spatial blurring for the latter model, as evidenced by a broader extent of higher PSF values, with respect to the same source in the realistic BEM and FDM models. Figure 7-8 shows an example of the results obtained for source 2, placed in the temporal region and *x*-oriented.

The PSF maps in the three models indicate the presence of a more pronounced spatial blurring for the sensor-fitted spherical model, evidenced by a broader extent of higher PSF values in the figure, with respect to the same source in the realistic BEM and in the FDM models.

To quantitatively compare, for the different head models, the spatial characteristics of the PSF maps at any given source position, and hence their power of discrimination for the EEG source reconstruction, the mean and minimum values of the obtained PSFs have been reported and compared for all the 78 analyzed dipole sources, being 1 the maximum PSF value in each condition, for the realistic BEM and FDM and the sensor-fitted spherical models. Table 8-3 and Table 8-4 summarize the quantitative results of the performed analysis on the PSF maps.

A closer inspection of the PSF values presented in Table 8-3 and Table 8-4 indicates that the reported mean PSF values are larger in the realistic BEM than in the FDM model in 79% of the total tested conditions (62 cases over 78), and specifically in 50%, 88%, and 100% of the analyzed situations for the *x*-, *y*-, and *z*-oriented sources, respectively (i.e., 13, 23, and 26 cases over 26, resp.), rising up to 100% for the RMS superimposition of the effects given by the three source orientations.

The minimum PSF values result larger in the BEM with respect to the FDM model in 27% of the tested conditions (21 cases over 78), in the 0%, 4%, and 77% of cases for the *x*-, *y*-, and *z*-oriented sources, respectively, rising up to 85% for the RMS data. The spherical head model (SPH) presents larger mean PSF values with respect to both the realistic BEM, and FDM models, for 60% (BEM) and 92% (FDM) of the total tested conditions (47 and 72 cases over 78, resp.), with minimum PSF values larger in 97% and 85% of the total conditions (76 and 66 cases over 78, resp.). The analysis of the RMS superimposition of the effects given by the three source orientations indicates that the spherical model shows larger mean PSF values in 85% of the tested conditions with respect to the BEM model, rising up to 96% for the FDM; the minimum PSF values result larger in 96% of the tested conditions for the BEM model and in 54% for the FDM. For *x*-oriented sources the spherical model shows larger mean and minimum PSF values in 96% and 100% of the tested conditions, respectively, for both the BEM and the FDM models.

The *y*-oriented sources show a similar behaviour with larger mean and minimum PSF values for the spherical model in 85% and 100% of the tested conditions with respect to BEM, and in 92% and 54% with respect to FDM. For *z*-oriented sources, the minimum PSF values result larger for the spherical model in 92% (BEM) and 100% (FDM) of the tested conditions.

Conversely, the *z*-oriented sources present smaller mean PSF values for the spherical model in comparison with the BEM in all the 26 tested conditions, while for the FDM this situation shows up only for 3 cases out of 26, thus giving larger mean PSF values for the spherical model with respect to FDM in 88% of the tested conditions. The evaluation of the mean SD values of the reported mean PSF values for the three models analyzed, listed in Table 8-3, confirmed these trends for the three source orientations and for the RMS data. The data from all the analyzed samples (FDM, BEM and SPH) resulted normally distributed and nine two-tailed paired *t*-tests have been performed to investigate differences between the spherical and the realistic models, that is, FDM versus BEM, FDM versus SPH and BEM versus SPH for the three source orientations.

Statistically significant differences have been found in the mean PSF values in 7 cases out of the total 9: for all source orientations for both BEM versus SPH ($x: p = 6.43 \times 10^{-7}$; $y: p = 1.90 \times 10^{-5}$; $z: p = 9.45 \times 10^{-8}$) and FDM versus SPH($x: p = 1.25 \times 10^{-10}$; $y: p = 6.74 \times 10^{-8}$; $z: p = 3.13 \times 10^{-4}$) and for the *z*-oriented sources ($p = 3.23 \times 10^{-13}$) in FDM versus BEM.

No statistically significant differences have been found in 2 cases, that is, for the *x*-oriented ($p = 0.70$) and for the *y*-oriented sources ($p = 0.28$) in FDM versus BEM. The analysis on the minimum PSF data led to similar results, with 7 cases of significant differences out of the total 9: for all source orientations in BEM versus SPH ($x: p = 1.43 \times 10^{-13}$; $y: p = 9.55 \times 10^{-11}$; $z: p = 2.17 \times 10^{-8}$), for the *x*-oriented ($p = 2.35 \times 10^{-6}$) and the *z*-oriented sources ($p = 2.02 \times 10^{-9}$) in FDM versus SPH (*y*-oriented sources: $p = 0.29$), and for the *x*-oriented ($p = 1.49 \times 10^{-12}$) and the *y*-oriented sources ($p = 3.49 \times 10^{-9}$) in FDM versus BEM (*z*-oriented sources: $p = 0.08$).

The RMS data showed significant differences in both FDM versus BEM and FDM versus SPH for either the mean (FDM versus BEM: $p = 1.90 \times 10^{-10}$); FDM versus SPH: $p = 1.90 \times 10^{-11}$) and the minimum PSF values (FDM versus BEM: $p = 8.34 \times 10 - 5$); FDM versus SPH: $p = 4.71 \times 10^{-7}$).

3.9.2 Extended FWHM values map

The obtained PSF FWHMs have been reported and compared for all the 26 analyzed dipole sources for each source orientation, for the realistic BEM and FDM and the sensor-fitted spherical models. Table 8-5 summarizes the quantitative results of the performed analysis on the PSF maps.

Basing upon a closer inspection of the PSF FWHM results presented in Table 8-5, it can be observed that the realistic FDM model presents an improvement over BEM in 68% of the total tested conditions (53 cases over 78), and specifically in 54% of the x-oriented sources (14 cases over 26), in 81% and 69% for the y- and z-oriented sources respectively (21 and 18 cases over 26, resp.), and in 38% of the RMS (10 over 26). The realistic BEM presents an improvement over the spherical model in 62% of the total tested conditions (48 cases over 78), in 77%, 73%, 35%, and 77% of the situations for the x-, y-, and z-oriented sources and RMS, respectively.

The improvement of FDM over the spherical model shows up in 88% of the analyzed situations for all the three source orientations, and in the 66% for the RMS. These trends are also confirmed by the mean SD values of the reported PSF FWHM results for the three models, shown in Table 8-5.

Nine two-tailed paired t-tests have been performed to investigate differences between the spherical and the realistic models (pairs FDM versus BEM, FDM versus SPH, and BEM versus SPH) for the three source orientations.

Statistically significant differences have been found in 7 out of the total 9 cases analyzed: for all source orientations in FDM versus SPH ($x : p = 2.03 \times 10^{-6}$; $y : p = 1.98 \times 10^{-4}$; $z : p = 1.93 \times 10^{-3}$), for the y- and z oriented sources in FDM versus BEM (y: p = 1.69×10^{-3}; z: $p = 3.66 \times 10^{-4}$), and for the

x- and y-oriented sources in BEM versus SPH (x : $p = 1.67 \times 10^{-2}$; y : $p = 2.83 \times 10^{-2}$).

The two-tailed paired t-tests performed on the RMS results showed significant differences in the FDM versus SPH pair ($p = 1.36 \times 10^{-2}$) and non significant differences in the FDM versus BEM ($p = 0.91$) and in the BEM versus SPH ($p = 5.63 \times 10^{-2}$).

In order to gather a broader evaluation of the PSF behavior on the overall brain cortex, we extended the evaluation of the FWHM PSF to all the 5000 points of the cortex surface. Figure 7-9 shows the differences between the FWHM RMS PSF maps between couples of different head models, to investigate the principal benefits or pitfalls given by the adoption of the different head models.

3.10 Evaluation of the effects given by different modelling choices

The dissimilarities between the forward fields simulated for the spherically approximated and the two different superficial- and volume-based realistic models have been investigated on standard real cortex geometry by means of analysis of the lead fields.

The Point Spread Function (PSF) has then been used to quantify the amount of spatial blurring of simulated cortical activity effects. The reported PSF values generally indicate a smaller extent, and hence a clear improvement, for the FDM realistic model in comparison with the BEM, and of the BEM model in comparison with the sensor-fitted spherical model (see Figure 7-8 and Figure 7-9 and Table 8-3,Table 8-4Table 8-5). This can be better observed analyzing the mean SD values of the reported PSF FWHM results for the three models, for which a clear trend in this sense can be observed for the *x*- and *y*-oriented sources, a slight worsening can be observed for the *z*-oriented sources in BEM versus SPH accompanied by an improvement in both FDM versus BEM and FDM versus SPH, and a slight improvement in FDM versus BEM for the RMS data, accompanied by an improvement of both FDM and BEM versus SPH. This trend in FDM versus BEM is reported also by the mean PSF values that are larger in the realistic BEM than in the FDM model in most of the total tested conditions for the separate source orientations, rising up to totality for the RMS superimposition of the effects given by the three source orientations.

This situation is accompanied by generally lower minimum PSF values for the BEM with the three separate source orientations but not for the RMS data, leading in general to smaller PSF FWHMs for FDM versus BEM with the separate source orientations, inferring a lower spatial blurring effect for FDM with respect to BEM; for the RMS superimposition of the effects given by the three source orientations the PSF FWHMs result rather similar, as indicated also by the presence of statistical significant differences in FDM versus BEM for the only *y*- and *z* oriented sources. The resulting trend in SPH versus BEM and versus FDM is also confirmed by the larger mean and minimum PSF values presented by the spherical head model with respect to both the realistic BEM and FDM in most of the total tested conditions for the separate three source orientations and for the RMS superimposition of the effects, with the exception of smaller mean PSF values for the spherical model than for the BEM for the *z*-oriented sources.

The exception behaviour observed for the *z*-oriented sources is reflected also by their PSF FWHMs, with an improvement of the realistic BEM over the spherical model in only 35% of the tested situations and by the presence of statistical significant differences for all source orientations and for the RMS values in the pair FDM versus SPH and for only the *x*- and *y*-oriented sources in the pair BEM versus SPH. It should be however observed that the improvement of one of the models with respect to the other one might be evaluated not only in terms of the sole mean PSF or of the PSF FWHM value but also in terms of the combined information which can be gathered basing upon these data. The relationship between the PSF FWHM and the standard deviation σ of the PSF can be in fact expressed as FWHM = $2\sqrt{2\ \ln 2}\sigma \approx 2.35482\sigma$. Considering that the signal-to-noise ratio (SNR) of the PSF can be expressed as the reciprocal of the coefficient of variation (CV) of the PSF distribution, which can be in turn expressed as the ratio of the standard deviation σ and the mean PSF, the SNRs of the PSF distributions for the BEM and the SPH models can be computed based upon the mean PSFs and the standard deviations obtained by the PSF FHWM values reported in Table 8-3 and Table 8-5.

The evaluation of the SNRs of the z-oriented sources for the BEM and the SPH models indicates that there is a general increase (22.7% mean) in the SNR for the BEM model with respect to the spherical one for all the z-oriented tested sources.

A worsening of both the realistic models versus the spherical can be observed for sources in the frontal lobe (Figure 7-9(c)–Figure 7-9(e), sources 3-4 in Figure 3-6), positioned in proximity of the frontal sinus. This might be due to the vicinity of the paranasal sinuses, which are actually filled with humid air but are nonetheless modelled as compact bone in our realistic models, in order not to introduce a fifth compartment. To test this hypothesis, sources 9-10 and 25-26 (see Figure 3-6) have been selected on the cortex mesh, placed laterally to sources 3 and 4 and to the paranasal sinuses, with the positive effect of improvement in terms of spatial blurring given by the realistic model (see Figure 7-9(c)–Figure 7-9(e)).

Results for sources placed in the temporal cortex (namely 2–5, 15-16, 17-18, and 19-20 in Figure 3-6) indicate that the realistic model generally leads to an improvement in terms of spatial blurring with respect to spherical model. The same trend is presented by realistic FDM with respect to BEM.

These results are in agreement with previous studies that showed that a 3-compartment realistic BEM model of the head outperformed a 3-shell spherical model, particularly in the temporal lobe [45]. This trend is also confirmed for sources which are positioned in the occipital cortex, namely, 7-8, 13-14, 21-22, and 23-24, again demonstrating that the adoption of a realistic model instead of a spherical one can lead to benefits in terms of power of discrimination for the reconstruction of these sources. The spherical model results in fact to perform best in the more spherical upper parts of the brain (see Figure 7-9(c)–Figure 7-9(f)), but fails in the temporal and occipital lobe areas, which cannot be well represented by the spherical shells.

These findings confirm earlier studies that showed similar behaviour [59]. Moreover, for sources located in parieto-occipital areas (see Table 8-5 for sources n. 13–17 and 21–24 and see Figure 7-9(b)–Figure 7-9(d) and Figure 7-9(e)), PSF parameters exhibit smaller FWHM for the realistic model, compared to the spherical one, with slightly smaller FWHM for BEM with respect to FDM that might be due to the smoothing of sulci presented by BEM.

The computational performances of the spherically approximated and of the two different BEM and FDM realistic models analyzed can provide also useful elements in order to assess cost-benefit of the specific model adopted. Computational performance was determined for the spherical and the BEM models with a standard PC (AMD64 3.00 GHz/3GB RAM, 2MB cache 2L) and for the FDM model with a Linux cluster PC composed by 8 elements of the same type (i.e., the above described unit as the front-end node plus 7 AMD64 3.00 GHz / 2GB RAM elements), as the FDM EEG forward problem solution was set up on a parallel computing implementation, given the higher computational load presented by the volume-based realistic models (FDM and FEM) [44]. When measuring the wall-clock time, it should be distinguished between the setup-computation that only has to be carried out once per head model for the building of the lead field matrix and the forward computations that has to be carried out hundreds or hundreds of thousands of times depending on the inverse problem solution procedure. During the setup, the computation of the leadfield matrix by means of the FDM solver took about 5.7 hours, that is, about 330 seconds per sensor. The resulting linear system matrix for the computation of each column vector of the lead field matrix had a size of about 14 GB, while the final lead field matrix had a size of about 8MB for all the three models considered. The computation of the LF matrix by means of the BEM solver took about 4.1 hours, being this the total time needed for the transfer matrix setup and decomposition with additional 12 s for the computation of the columns of the LF matrix for all the sensors. The computation of the LF matrix by means of the adopted sensor-fitted spherical approach needed a time of 0.82 hours (2960 seconds).

It should finally be underlined that the cost-benefit of having selected one or the other of the analyzed models should consider only the initial setup time for computing and storing the leadfield matrixes for the different models [34] . The choice of adopting one specific head model has then to be made in terms of costs basing on the one-time initial setup time, and taking into consideration for the benefits the factors of improvement that are gathered by the different models which have been here evaluated in terms of the specific PSF maps.

In conclusion, the obtained results demonstrate that realistic geometry can provide a factor of improvement which is particularly important when considering sources placed in the temporal or in the occipital cortex. In these situations, using a realistic head model will allow a better spatial discrimination of neural sources in comparison with the spherical model, as it can be appreciated by the analysis of the PSF maps presented in this dissertation. It is also worth stressing that the results presented in this dissertation, thanks to the adoption of the MNI-based models, based on a large series of MRI scans on normal controls and thus reflecting average neuroanatomy more representative of the population, can be enrichment with respect to other studies for the possibility of gathering more general information also extensible to other application studies in this field.

4 Application to EEG-fMRI multimodal integration

4.1 Aim of the study

In this study spatially selective EEG information will be extracted within the general framework of a cortex-based distributed source EEG analysis and used to study "region-specific" EEG-fMRI coupling effects.

To this end, we will perform a whole-cortex spectral perturbation analysis in a given time-frequency window, localize extended regions of maximal, narrow-band EEG synchronization and extract regional power time-courses for fMRI modelling and prediction.

We focused on the study of alpha band effects during the application of a common EEG-fMRI acquisition protocol called the "eyes closed-eyes open experiment". We focused our investigation in the primary visual cortex (V1) brain region, as it is well-known to be involved in this task execution [100].

Most of the performed analysis has been carried out basing on BrainVoyager QX 2.3 (Brain Innovation, Maastricht, The Netherlands) to analyze the recorded f/MRI data [101] in conjunction with the "EEG Distributed Source Analysis" for the forward and inverse EEG modelling methods discussed in chapter 2.

4.2 Building of the realistic model

As the T1 MRI dataset comes from real acquired data, it exhibits a low SNR, and a more robust segmentation algorithm was required in comparison with the MNI model data.

The FSL software package [88], [89] provided a suitable atlas-based segmentation tools that met the needs to segment the brain volume into 3 compartments: CSF, gray and white matter.

The remaining skull and skin tissues have been segmented by means of semi automated algorithms. The obtained results are illustrated in Figure 4-1:

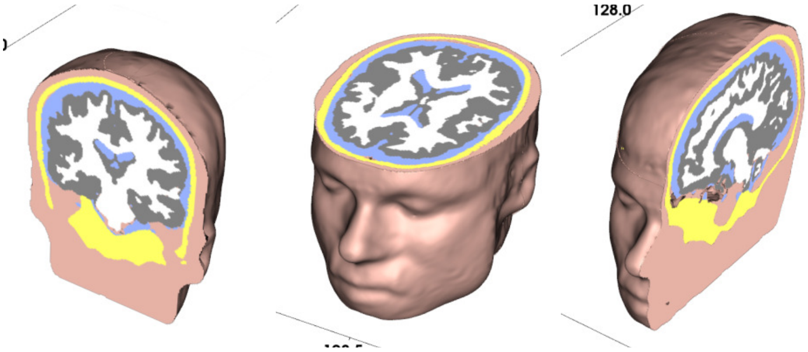

Figure 4-1 segmentation of subject specific MRI data into five compartments: white matter (white color), grey matter (grey color), CSF (blue), skull (yellow), skin (pink). From left to right: axial, coronal and sagittal slice view

4.3 Experimental design

In this simultaneous EEG-fMRI experiment the subject was asked to alternate between periods of resting with eye open (14s) (the baseline) and eye closed (18s). The fMRI data set (TR=2s) has been entirely pre-processed and spatially transformed to the Talairach space with a spatial Gaussian filtering

FWHM 6mm wide. Furthermore, a head mesh and a cortical surface mesh (see Figure 4-2) have been made available and reconstructed in the Talairach space. The channels acquired are incorporated in a 62 channels cap (see Figure 4-2), and have been acquired at a sampling rate Fs=250Hz.

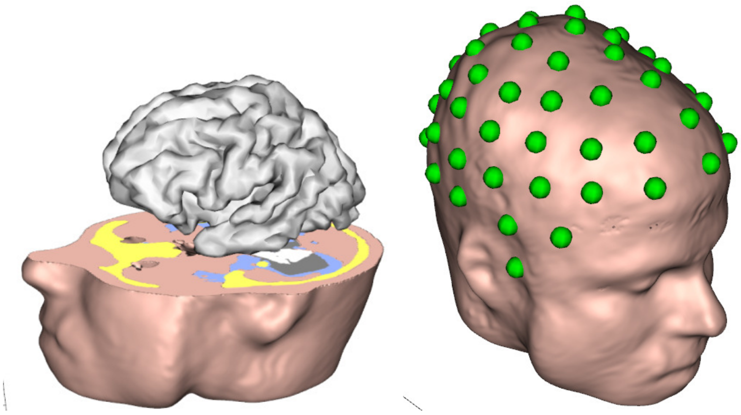

Figure 4-2 Left: cortical mesh source space. Right: electrodes set

4.4 fMRI activation imaging

We ran one single study GLM on the functional data, thus obtaining both the volumetric and cortical maps. The functional volume time course data has been previously filtered by a spatial Gaussian kernel 6mm wide, in order to prevent noise effects. A default predictor was used for the closed-eyes condition, showed in the figure below:

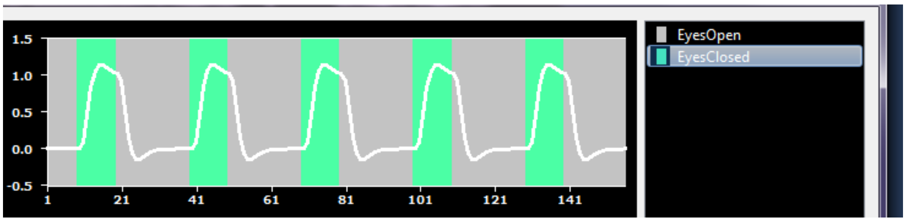

Figure 4-3 GLM standard predictor, resulting from convolution between box-car function and HRF

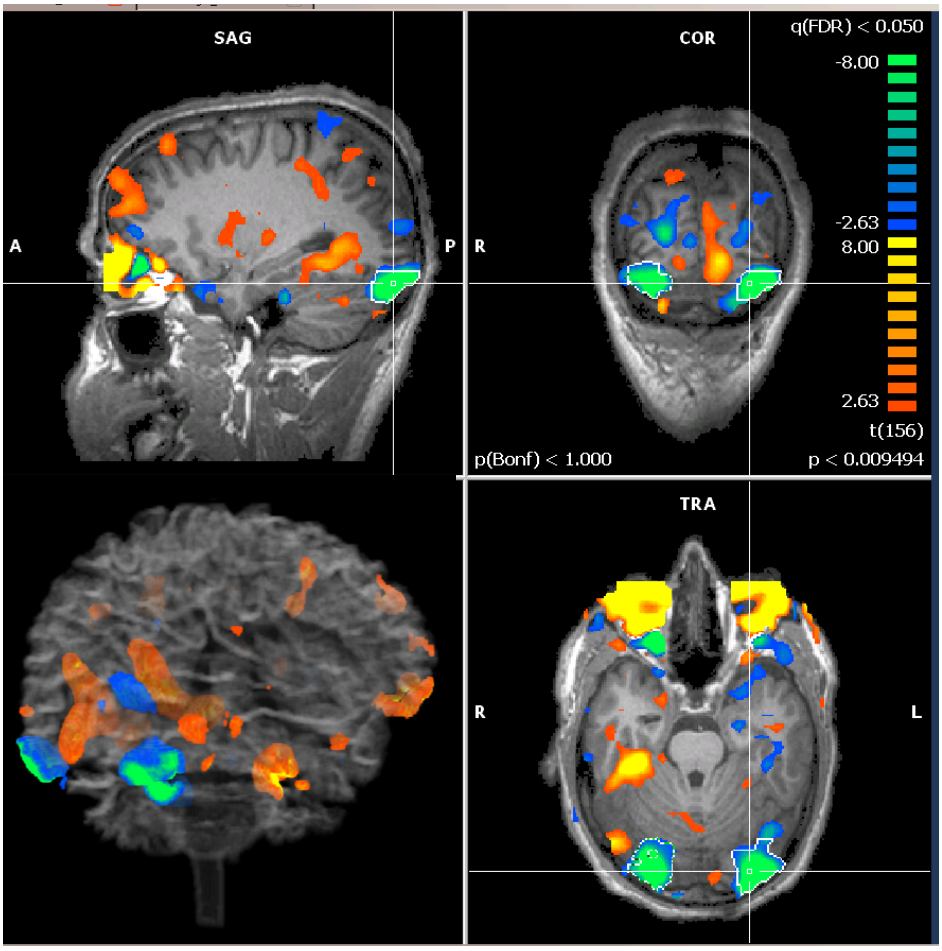

Figure 4-4 Volume map of the statistical contrast between the two conditions.

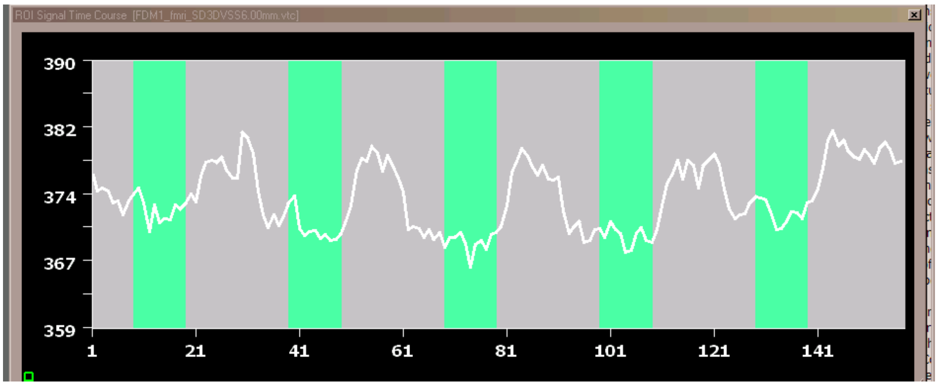

Figure 4-5. The fMRI signal timecourse averaged between points belonging to the region of interest (ROI)

We built the GLM for both the experimental conditions (eyes closed and eyes open, see Figure 4-3), then a contrast map was computed, in which we compared the differences in the statistical values of each condition (Figure 4-4). Since the difference has been defined as “eyes open vs. eyes closed”, the green regions in the visual cortex mean that that region is significantly active during “eyes closed” condition, compared to “eyes open” condition.

In Figure 4-5 the fMRI signal time course averaged between points belonging to the region of interest (ROI) is reported. The selected ROI belongs to the V1, and it has been projected onto the cortical surface (see Figure 4-6), to be the computational domain for the statistical analysis.

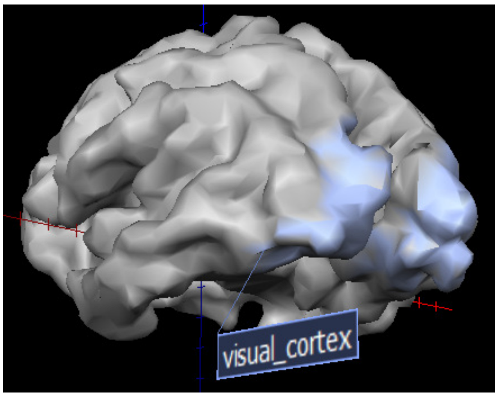

Figure 4-6 patch of interest of the cortical mesh

Projecting the statistical volume map onto the cortical mesh produced the cortical map reported in Figure 4-7.

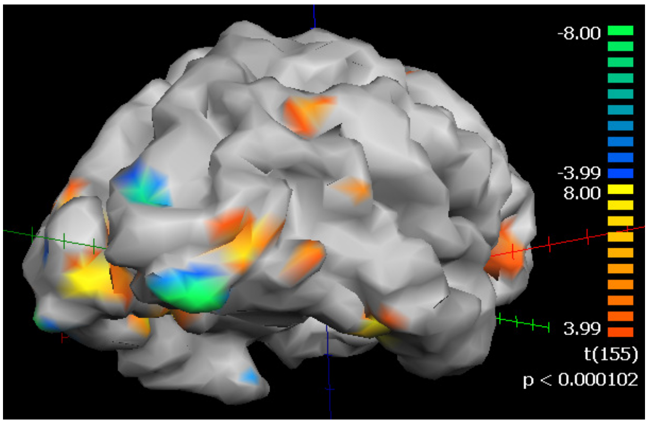

Figure 4-7 fMRI statistical contrast map projection on the cortical mesh

4.5 EEG distributed source analysis

Since the entire procedure, described in this paragraph, takes as input a previously calculated lead field matrix, it is possible to compare the source imaging results among different modelling techniques. In our investigation we used realistic (FDM) and spherical models lead fields, pre-computed using the algorithms described in chapter 2.

4.5.1 Channel pre-processing

The EEG signal projection from the channel to the source space requires that channel data are preliminary organized as single-trial channel data (STD) or time-frequency data (TFD) [102], [85].

This means that, with or without final averaging and time-frequency transformation, single trials have to be extracted from continuous channel data (CTC). Moreover, the experimental condition has to be specified.

The most important triggers we are seeking in the EEG data are called "R1" and "S2" in the acquisition protocol, and they correspond to the fMRI trigger at each TR and the instruction for closing eyes, respectively. We started with analyzing the data with respect to trigger "S2" by selecting a pre-trigger interval of 5000ms and a post-trigger interval of 20000ms

In order to produce time-frequency transform (which is based on the Short-Time Fourier Transform), we set a time resolution of the analysis of 200ms, and a time window 2s wide. Since we are interested in alpha band (i.e. around 10 Hz) signals, we filtered the EEG data up to 20Hz.

A plot of the TFD gives a scaled image trial averaged positive and negative changes of the spectral power around the condition trigger. In many channels, a strong positive change in the event-related spectral perturbation (synchronization) induced by the status change from eye open to eye closed can be observed inside the alpha band (8-13 Hz).

In order to define the cortical region of maximal synchronization, we have to estimate a distributed inverse solution that we will later use for projecting EEG signals in a pre-specified time-frequency box from the channel to the source space.

4.5.2 Covariance calculation

Recalling section 2.2.4, we now need to estimate the data covariance matrix. In order to create a condition-independent inverse solution with maximal statistical power, the STD created from all conditions in the protocol is used. In the context of *beamforming* techniques the covariance matrix will be later used to quantify the amount of interference between all possible sources "visible" in the channel space.

4.5.3 Inverse Modeling

Now we can combine the covariance data with the previously computed lead fields, to produce the EEG inverse problem solution.

The inverse methods adopted at this point are the LCMV beamforming, which has been mentioned in chapter 2.2.4, as it has been recently shown to achieve the best results when applied to distributed source localization [20], [103]; furthermore, the well know and used WMN filter with noise based regularization (see 2.2.4.4) has also been used for comparative purpose.

4.5.4 Source time-course reconstruction

The newly computed inverse solution can be used for reconstructing the source time-course at each point of the cortex mesh, in term of RMS power signal (virtual electrode) [102], [85]. We reconstruct the source power time-courses in a mesh time-course after filtering the single-trial data set.

For the present application, it is not interesting to project full-band or averaged data, but rather narrow-band time-courses, which can be obtained by using continuous-wavelet-transform filters with wavelet functions adapted to the desired centre frequency and the desired duration-bandwidth ratio. A centre frequency of 11 Hz and a wavelet ratio of 11 are used.

It is important to check the approximate duration and bandwidth of the wavelet for these settings before proceeding with the filtering. Provided that the bandwidth is acceptable, the duration of the wavelet also affects the choice of a possible decimation of the projected time courses. Here we use a decimation factor of 100 which entails to resample the source power time-courses from the original sampling period of 4 ms to a sampling period of 400ms. Since we are interested in appreciating any induced sustained perturbation in a long period of 20s, rather than fast transient effects, the new sampling period can be accepted. Later, the created mesh time-course with the average induced source power perturbations will be displayed, after the final source analysis.

4.5.5 Source imaging and statistical analysis

The approach presented in [102], [85] allows generating (series of) brain activity maps for specific time (or time-frequency) intervals of interest and producing source time and time-frequency plots from regions of interest prespecified as patches of interest (POIs).

The input data of this final stage is again the TFD computed by the preprocessing step. The “target” time-frequency box will consist of the entire period of closed-eye (18s) and of the entire alpha band (8:13Hz). The baseline for the source statistical image is the entire prestimulus interval (-5000ms:0).

The output of the source image analysis will be a t-map expressing the statistical significance of the target vs baseline effects in the specified time-frequency box. For illustrative purposes it will be used a reference threshold of t=3.50 (p=0.000486) that highlights a distributed region in the occipital cortex where the studied effects is relatively stronger (see Figure 4-8). Moreover, the patch-of-interest of the “activated” region allows displaying the spatially averaged source power change. The image shows the region where alpha modulation was maximally expressed, compared to the rest of the cortex.

As a rule of thumb, the threshold statistical test values are typically visualized using a red-to-yellow colour range for positive values and a green-to-blue range for negative values. With this colour bar, a positive (negative) t value just passing over a specified threshold would be coloured in red (green), while a very highly positive (negative) t value would be coloured in yellow (blue).

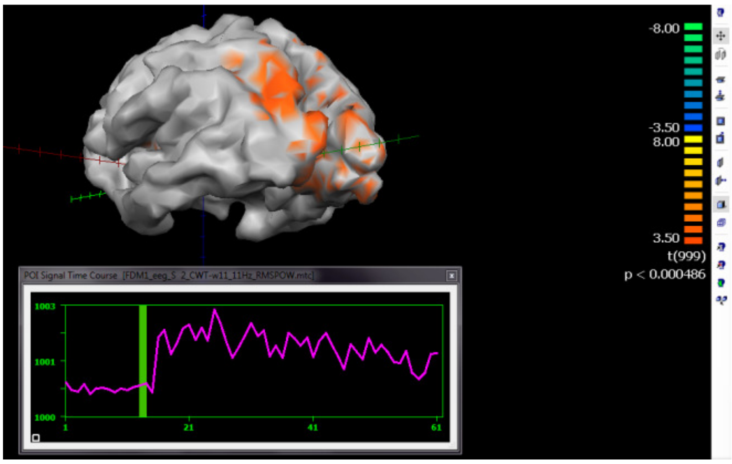

Figure 4-8 Example of typical source imaging (cortical map on top) and time reconstruction(plot on bottom) result

4.6 EEG-fMRI distributed Source Coupling Analysis

According to the considerations in paragraph 2.4.5.3, this experimental design is suitable for being studied by means of EEG-fMRI coupling analysis.

4.6.1 Channel pre-processing

This time we selected the protocol condition that includes all fMRI triggers, i.e. “R1”, and set the pre-trigger and post-trigger timings to -500.00 and 1500 ms, respectively. The data pre-processing has been ran setting a finer time resolution for the time-frequency analysis: 20ms and a time window of 0.2s. The maximum frequency has been kept at 20 Hz.

4.6.2 Single design matrix

The next processing steps remain almost the same as in section 4.4, except for the statistical source analysis, which now is required to output the so-called *single design matrix* (SDM). According to section 2.4.5.2, we will give as input, in the GLM analysis, a prediction of the temporal fMRI signal, basing on the convolution of HRF with the EEG signal. The estimation of the SDM implies collecting the EEG data series (for the condition R1) from all the trials available and, finally, z-standardized. This process requires the a-priori knowledge of three fMRI parameters for the correct synchronization between EEG and fMRI time points and the application of the hemodynamic correction: the time in milliseconds of the first fMRI trigger corresponding to the first fMRI scan actually included in the analysis (in our case 0), the fMRI repetition time (TR=2) and the number of scans constituting the fMRI time-series (this case 158).

4.7 fMRI weighting of an EEG inverse solution

The last approach we applied is conceptually the opposite of the latter, since we first process the functional data, and then we use the informations as a weighting for the EEG inverse solution. The fMRI processing gave an F-map summarizing the fMRI main effects of interest and a second map with the percentage of signal change of these effects (see Figure 4-9).

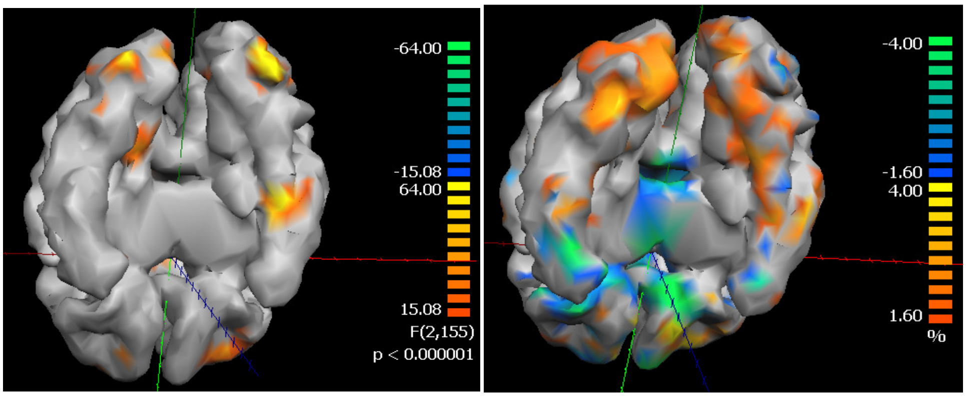

Figure 4-9 FMRI maps used for MEG spatial weighting. F-map (left) and % s.c. map (right) for the main effects of the conditions (linear contrast: +1, +1).

Here it is also important to apply a reasonable statistical threshold to the F-map for discriminating sources with significant fMRI effects from sources with non-significant main effects.

4.8 Results

4.8.1 EEG-source analysis

Figure 7-11 shows the t-maps among different forward and inverse modelling techniques: realistic FDM model (see paragraph 4.2) and four-shells sensor-fitted spherical model; while beamforming and WMN where used as inverse algorithms. The EEG source localization of these effects entailed with finding the local peaks of the cortical maps [104] and accepting as EEG sources the local peaks whose corresponding p-value was below 0.001 (uncorrected).

Moreover, the induced RMS source power perturbation time course is plotted at bottom of each map, showing the values spatially averaged across the POI, and temporally averaged across trials.

4.8.2 EEG-fMRI coupling

Considering the same four cases aforementioned, we illustrate in Figure 7-12 the different fMRI predictors estimated from the EEG data, given different inverse solutions for different modelling techniques.

Furthermore, the cortical maps of the standardized t-maps are shown in Figure 7-13. The p-value threshold is set to 0.00165. Figure 7-13a refers to the fMRI classic analysis, i.e. not driven by EEG data.

4.8.3 fMRI weighting of EEG inverse solution

Since the weighting of an inverse solution applies only to imaging approaches, this technique has not been used in conjunction with beamforming. The figures report the t-maps for the realistic as well as the spherical model, both processed by means of WMN noise normalized inverse method with fMRI weighting and Bonferroni corrected (p=0.05).

4.9 Evaluation of brain source reconstruction capabilities

This study focused on the alpha band modulation effects during an experimental “eyes open-eyes closed” protocol in an EEG-fMRI contemporary acquisition. In the EEG framework, we epoched the EEG single trial data, and extracted the time-frequency components of interest (frequency band from 8 to

13 Hz, consistent with findings in [105]). Then the preprocessed data, as well as the channels covariance estimation and the precomputed lead fields, entered the inverse modelling algorithm to produce the source imaging and RMS power time-course.

An fMRI statistical activation map was separately computed, using a standard GLM with two different predictors for the two conditions.

Then two kind of multimodal integration have been performed. First, the source power time-series were exploited to derive a predictor with source-specific information in the GLM analysis of the functional MRI.

The maps illustrated in Figure 7-11a,b show that the EEG source analysis is strongly affected by the choice of the forward modelling applied, as pointed out also in [6, 63, 94, 106]. Even if both realistic and approximated geometry models lead to an inverse solution centred in the visual cortex, according findings in [107], they also spot different regions, sparse around the patch-of-interest (POI) of Figure 4-6. Since the FDM algorithm applied [8] takes into account the realistic geometry of the whole head, it is reasonable to consider it more reliable. This is true as long as the noise is mostly correlated noise, rather than Gaussian [63].

In order to give more strongly evidences on the absolute increasing in accuracy led by the introduction of a realistic model, a group study on a wider number of subjects will be used in required for further investigations.

The first methodological consideration is focused on the choice of the inverse problem algorithm applied. While LORETA solution is analogous to the noise-normalized WMN solution used in others recent works (see e.g. [85]), it only differs from the latter by the smoothness constrain, which is embodied in matrix **R** in equation (2 . 3 8), and by the requirement of a regular-grid sources domain [69]. Here we did not use LORETA because in current literature, to our knowledge, there are no evidences of its application in a mesh-based distributed source modelling.

As expected, the EEG source analysis, as well as the source temporal reconstruction, is sensitive to the inverse algorithm used. As shown in Figure 7-11c,d the beamforming technique seems to produce an inaccurate source localization when applied to the spherical forward model, thus exhibiting a low average power time course, compared to the realistic case. However, since beamforming has been proven to be effective in source localization and particularly in rejecting interferences in EEG signals [108], a deeper comparative investigation of the performances of the two implementations is required.

Another methodological issue regards the regularization parameter in the WMN spatial filtering estimation (eq. (2 . 4 2)). It has been observed that, at constant SNR guess and with the same depth factor (γ in equation (2 . 3 7), the lambda parameter sensibly increases when computed on a realistic leadfield matrix, compared to the spherical LF. Although in many evoked response experiments [81] the used value is 5, this might not be suited for a realistic-derived forward field, for which can be empirically verified that:

$$\mathit{trace}(\mathbf{L}_{\mathbf{FDM}}*\mathbf{L}^{\mathbf{T}}_{\mathbf{FDM}}) << \mathit{trace}(\mathbf{L}_{\mathbf{SPH}}*\mathbf{L}^{\mathbf{T}}_{\mathbf{SPH}})$$

This aspect should be object of further studies.

As shown in Figure 7-13, the contribute of the EEG inverse analysis to the fMRI source localization is relevant, as already showed in [85] [102], as it helps isolating the alpha-band effective sources of the V1 region. A closer look, also to Figure 7-12, suggests this EEG-fMRI coupling technique does not show to be sensitive to the forward-modelling approach used, but rather to the inverse modelling algorithm. In this case the beamforming seemed to perform better than WMN, since the latter tends not to lose the left V1 activated region (see Figure 7-13).

fMRI weighting of the EEG inverse analysis (see Figure 7-14) produces relevant effects on source localization, confirming the findings in [74]. In spite of EEG fMRI coupling approach, this technique is sensitive to the model adopted, other than the fMRI weighting parameter *k* defined in 2.4.1.

As it has been observed, the regularization parameter λ increases almost linearly, keeping the SNR guess constant, with k. The overall effect of the functional constraints is to then to “smoothly bias” the EEG solution towards the most statistically significant BOLD signal changes. In the results illustrated in Figure 7-14, only two values of k have been used: 20 and 80. Other trials involved either smaller or greater values, but they led to totally ignoring fMRI contribution, or ignoring EEG contribution, respectively.

Finally, as we expected, both the realistic and spherical models benefit from the approach.

5 *Conclusions*

In this chapter a general conclusion is given of this dissertation, followed by brief overview of the future works.

In the first part of the research we compared different spherical and realistic head modelling techniques in estimating EEG forward solutions from current dipole sources distributed on a standard cortical space reconstructed from Montreal Neurological Institute (MNI) MRI data. Computer simulations are presented for three different four-shell head models, two with realistic geometry, either surface-based (BEM) or volume-based (FDM), and the corresponding sensor-fitted spherical-shaped model. Point Spread Function (PSF) and Lead Field (LF) cross-correlation analyses were performed for 26 symmetric dipole sources to quantitatively assess models' accuracy in EEG source reconstruction.

The results obtained demonstrate that realistic geometry can provide a factor of improvement which is particularly important when considering sources placed in the temporal or in the occipital cortex. In these situations, using a realistic head model will allow a better spatial discrimination of neural sources in comparison with the spherical model, as it can be appreciated by the analysis of the PSF maps as shown in chapter 3. Hence, in this investigation we have demonstrated that a significant improvement in source modelling accuracy can be obtained without significant increase in effort, namely replacing the standard spherical head model with a standardized realistically shaped FDM head model. By appropriately warping the electrode array of an individual patient to the standardized model, the same realistic head model can be used for any patient with great gain in computational speed because the time-consuming numerical calculations of the FDM matrixes have already been performed. At the speed of modern PCs, the additional computation effort needed to use this standardized model is reasonable. This is particularly true when considering the improved accuracy afforded by such a standardized FDM model and the amount of effort required to set up an individualized head model. It is also worth stressing that the results presented in this dissertation, thanks to the adoption of the MNI-based models, based on a large series of MRI scans on normal controls and thus reflecting average neuroanatomy more representative of the population, can be an enrichment with respect to other studies for the possibility of gathering more general information also extensible to others application studies in this field

Later we increased the complexity of the MNI-based realistic model, implementing a multi-subject DTI data integration that led to an accurate anisotropy description of the white matter and skull bones tissues. We have also shown a novel comparative analysis performed between isotropic and anisotropic forward fields, whose results comply with previous literature's findings.

In the last part of our studies, two methods of EEG-fMRI data integration have been included in the multimodal framework and applied to different modeling techniques. The preliminary results point out an improvement in EEG source imaging reliability by means of the beamforming EEG inverse modelling approach on a realistic forward model. Noticeably, it has been shown that both EEG-driven fMRI, as well as fMRI-driven EEG analysis can further improve both fMRI's source localization and EEG's source reconstruction accuracy.

However, it should be considered that since in the literature there are no group-analysis experimental studies performed with realistic modelling approach, this aspect should be further investigated. Other than this, there are some more issues that still need to be addressed in future works: how the LF matrix conditioning is related to the regularization parameter involved in the source imaging approaches, and how to define an optimal *pre-regularization* of the LF matrix. Furthermore the application of LAURA or LORETA inverse algorithms, to the multimodal integration is also attractive, but requires the definition of a different source-seeking spatial domain.

6 Bibliography

1. Vatta, F., P. Bruno, and P. Inchingolo, *Improving lesion conductivity estimate by means of EEG source localization sensitivity to model parameter.* J Clin Neurophysiol, 2002. **19**(1): p. 1-15.
2. Ebersole, J.S. and S. Hawes-Ebersole, *Clinical application of dipole models in the localization of epileptiform activity.* J Clin Neurophysiol, 2007. **24**(2): p. 120-9.
3. Goldman, R.I., et al., *Acquiring simultaneous EEG and functional MRI.* Clin Neurophysiol, 2000. **111**(11): p. 1974-80.
4. Lemieux, L., et al., *Event-related fMRI with simultaneous and continuous EEG: description of the method and initial case report.* Neuroimage, 2001. **14**(3): p. 780-7.
5. Gholipour, T., et al., *Reproducibility of interictal EEG-fMRI results in patients with epilepsy.* Epilepsia, 2010.
6. Meneghini, F., et al., *Comparison between realistic and spherical approaches in EEG forward modelling.* Biomed Tech (Berl), 2010. **55**(3): p. 133-46.
7. Vatta, F., et al., *Realistic and spherical head modeling for EEG forward problem solution: a comparative cortex-based analysis.* Comput Intell Neurosci, 2010: p. 972060.
8. Meneghini, F., et al., *Threedimensional eeg source reconstruction on high performance computers methodological and computational issues.* Biomed Sci Instrum, 2008. **44**: p. 336-41.
9. Vatta, F., et al., *Head modeling for realistic electrical brain activity mapping identification of a multimodal neuroimaging protocol.* Biomed Sci Instrum, 2008. **44**: p. 342-8.
10. Basser, P.J., J. Mattiello, and D. LeBihan, *Estimation of the effective self-diffusion tensor from the NMR spin echo.* J Magn Reson B, 1994. **103**(3): p. 247-54.
11. Basser, P.J., J. Mattiello, and D. LeBihan, *MR diffusion tensor spectroscopy and imaging.* Biophys J, 1994. **66**(1): p. 259-67.
12. Hasan, K.M., D.L. Parker, and A.L. Alexander, *Comparison of gradient encoding schemes for diffusion-tensor MRI.* J Magn Reson Imaging, 2001. **13**(5): p. 769-80.
13. Koay, C.G., et al., *A unifying theoretical and algorithmic framework for least squares methods of estimation in diffusion tensor imaging.* J Magn Reson, 2006. **182**(1): p. 115-25.
14. Alexander, A.L., et al., *A geometric analysis of diffusion tensor measurements of the human brain.* Magn Reson Med, 2000. **44**(2): p. 283-91.
15. Westin, C.F., et al., *Processing and visualization for diffusion tensor MRI.* Med Image Anal, 2002. **6**(2): p. 93-108.
16. Makris, N., et al., *Morphometry of in vivo human white matter association pathways with diffusion-weighted magnetic resonance imaging.* Ann Neurol, 1997. **42**(6): p. 951-62.
17. Pajevic, S. and C. Pierpaoli, *Color schemes to represent the orientation of anisotropic tissues from diffusion tensor data: application to white matter fiber tract mapping in the human brain.* Magn Reson Med, 1999. **42**(3): p. 526-40.

18. Witwer, B.P., et al., *Diffusion-tensor imaging of white matter tracts in patients with cerebral neoplasm.* J Neurosurg, 2002. **97**(3): p. 568-75.
19. Lazar, M., et al., *White matter reorganization after surgical resection of brain tumors and vascular malformations.* AJNR Am J Neuroradiol, 2006. **27**(6): p. 1258-71.
20. Grech, R., et al., *Review on solving the inverse problem in EEG source analysis.* J Neuroeng Rehabil, 2008. **5**: p. 25.
21. He, B., D. Yao, and J. Lian, *High-resolution EEG: on the cortical equivalent dipole layer imaging.* Clin Neurophysiol, 2002. **113**(2): p. 227-35.
22. Hara, J., T. Musha, and W.R. Shankle, *Approximating dipoles from human EEG activity: the effect of dipole source configuration on dipolarity using single dipole models.* IEEE Trans Biomed Eng, 1999. **46**(2): p. 125-9.
23. Zhou, H. and A. van Oosterom, *Computation of the potential distribution in a four-layer anisotropic concentric spherical volume conductor.* IEEE Trans Biomed Eng, 1992. **39**(2): p. 154-8.
24. Klepfer, R.N., C.R. Johnson, and R.S. Macleod, *The effects of inhomogeneities and anisotropies on electrocardiographic fields: a 3-D finite-element study.* IEEE Trans Biomed Eng, 1997. **44**(8): p. 706-19.
25. Marin, G., et al., *Influence of skull anisotropy for the forward and inverse problem in EEG: simulation studies using FEM on realistic head models.* Hum Brain Mapp, 1998. **6**(4): p. 250-69.
26. Akhtari, M., et al., *A model for frequency dependence of conductivities of the live human skull.* Brain Topogr, 2003. **16**(1): p. 39-55.
27. Nicholson, P.W., *Specific impedance of cerebral white matter.* Exp Neurol, 1965. **13**(4): p. 386-401.
28. Le Bihan, D., et al., *Diffusion tensor imaging: concepts and applications.* J Magn Reson Imaging, 2001. **13**(4): p. 534-46.
29. Tuch, D.S., *Q-ball imaging.* Magn Reson Med, 2004. **52**(6): p. 1358-72.
30. Bastiani, M., *Fibre-tracking in high angular resolution diffusion imaging of cortical white matter: crossing-fibre models, graph tractography and cortico-cortical connectome tractography* in *Department of Cognitive Neuroscience, Faculty of Psychology and Cognitive Neuroscience*

2009, Maastricht University.

31. Plonsey, R. and D.B. Heppner, *Considerations of quasi-stationarity in electrophysiological systems.* Bull Math Biophys, 1967. **29**(4): p. 657-64.
32. Mosher, J.C., R.M. Leahy, and P.S. Lewis, *EEG and MEG: forward solutions for inverse methods.* IEEE Trans Biomed Eng, 1999. **46**(3): p. 245-59.
33. Vanrumste, B., et al., *The validation of the finite difference method and reciprocity for solving the inverse problem in EEG dipole source analysis.* Brain Topogr, 2001. **14**(2): p. 83-92.
34. Weinstein, D., L. Zhukov, and C. Johnson, *Lead-field bases for electroencephalography source imaging.* Ann Biomed Eng, 2000. **28**(9): p. 1059-65.
35. Zhang, Z., *A fast method to compute surface potentials generated by dipoles within multilayer anisotropic spheres.* Phys Med Biol, 1995. **40**(3): p. 335-49.
36. Cuffin, B.N., *Effects of head shape on EEG's and MEG's.* IEEE Trans Biomed Eng, 1990. **37**(1): p. 44-52.
37. Cuffin, B.N., *Eccentric spheres models of the head.* IEEE Trans Biomed Eng, 1991. **38**(9): p. 871-8.

38. Huang, M.X., J.C. Mosher, and R.M. Leahy, *A sensor-weighted overlapping-sphere head model and exhaustive head model comparison for MEG.* Phys Med Biol, 1999. **44**(2): p. 423-40.
39. Vatta, F., P. Bruno, and P. Inchingolo, *Multiregion bicentric-spheres models of the head for the simulation of bioelectric phenomena.* IEEE Trans Biomed Eng, 2005. **52**(3): p. 384-9.
40. Gutierrez, D. and A. Nehorai, *Array response kernels for EEG and MEG in multilayer ellipsoidal geometry.* IEEE Trans Biomed Eng, 2008. **55**(3): p. 1103-11.
41. Ermer, J.J., et al., *Rapidly recomputable EEG forward models for realistic head shapes.* Phys Med Biol, 2001. **46**(4): p. 1265-81.
42. Fuchs, M., et al., *An improved boundary element method for realistic volume-conductor modeling.* IEEE Trans Biomed Eng, 1998. **45**(8): p. 980-97.
43. Zhang, Y., et al., *A cortical potential imaging study from simultaneous extra- and intracranial electrical recordings by means of the finite element method.* Neuroimage, 2006. **31**(4): p. 1513-24.
44. Hallez, H., et al., *Review on solving the forward problem in EEG source analysis.* J Neuroeng Rehabil, 2007. **4**: p. 46.
45. Fuchs, M., M. Wagner, and J. Kastner, *Boundary element method volume conductor models for EEG source reconstruction.* Clin Neurophysiol, 2001. **112**(8): p. 1400-7.
46. Ramon, C., J. Haueisen, and P.H. Schimpf, *Influence of head models on neuromagnetic fields and inverse source localizations.* Biomed Eng Online, 2006. **5**: p. 55.
47. Yvert, B., et al., *A systematic evaluation of the spherical model accuracy in EEG dipole localization.* Electroencephalogr Clin Neurophysiol, 1997. **102**(5): p. 452-9.
48. Cuffin, B.N., *Effects of local variations in skull and scalp thickness on EEG's and MEG's.* IEEE Trans Biomed Eng, 1993. **40**(1): p. 42-8.
49. Brody, D.A., F.H. Terry, and R.E. Ideker, *Eccentric dipole in a spherical medium: generalized expression for surface potentials.* IEEE Trans Biomed Eng, 1973. **20**(2): p. 141-3.
50. Cuffin, B.N. and D. Cohen, *Comparison of the magnetoencephalogram and electroencephalogram.* Electroencephalogr Clin Neurophysiol, 1979. **47**(2): p. 132-46.
51. Ary, J.P., S.A. Klein, and D.H. Fender, *Location of sources of evoked scalp potentials: corrections for skull and scalp thicknesses.* IEEE Trans Biomed Eng, 1981. **28**(6): p. 447-52.
52. Berg, P. and M. Scherg, *A fast method for forward computation of multiple-shell spherical head models.* Electroencephalogr Clin Neurophysiol, 1994. **90**(1): p. 58-64.
53. Sarvas, J., *Basic mathematical and electromagnetic concepts of the biomagnetic inverse problem.* Phys Med Biol, 1987. **32**(1): p. 11-22.
54. de Munck, J.C., *A linear discretization of the volume conductor boundary integral equation using analytically integrated elements.* IEEE Trans Biomed Eng, 1992. **39**(9): p. 986-90.
55. Oostendorp, T.F. and A. van Oosterom, *Source parameter estimation in inhomogeneous volume conductors of arbitrary shape.* IEEE Trans Biomed Eng, 1989. **36**(3): p. 382-91.

56. Ferguson, A.S., X. Zhang, and G. Stroink, *A complete linear discretization for calculating the magnetic field using the boundary element method.* IEEE Trans Biomed Eng, 1994. **41**(5): p. 455-60.
57. George, J.S., et al., *Mapping function in the human brain with magnetoencephalography, anatomical magnetic resonance imaging, and functional magnetic resonance imaging.* J Clin Neurophysiol, 1995. **12**(5): p. 406-31.
58. Yvert, B., A. Crouzeix-Cheylus, and J. Pernier, *Fast realistic modeling in bioelectromagnetism using lead-field interpolation.* Hum Brain Mapp, 2001. **14**(1): p. 48-63.
59. Fuchs, M., et al., *A standardized boundary element method volume conductor model.* Clin Neurophysiol, 2002. **113**(5): p. 702-12.
60. Bruno, P., et al., *A FDM anisotropic formulation for EEG simulation.* Conf Proc IEEE Eng Med Biol Soc, 2006. **1**: p. 1121-5.
61. Saleheen, H.I. and K.T. Ng, *New finite difference formulations for general inhomogeneous anisotropic bioelectric problems.* IEEE Trans Biomed Eng, 1997. **44**(9): p. 800-9.
62. Schimpf, P.H., C. Ramon, and J. Haueisen, *Dipole models for the EEG and MEG.* IEEE Trans Biomed Eng, 2002. **49**(5): p. 409-18.
63. Vanrumste, B., et al., *Comparison of performance of spherical and realistic head models in dipole localization from noisy EEG.* Med Eng Phys, 2002. **24**(6): p. 403-18.
64. Vanrumste, B., et al., *Dipole location errors in electroencephalogram source analysis due to volume conductor model errors.* Med Biol Eng Comput, 2000. **38**(5): p. 528-34.
65. Van Hoey, G., et al., *Influence of measurement noise and electrode mislocalisation on EEG dipole-source localisation.* Med Biol Eng Comput, 2000. **38**(3): p. 287-96.
66. de Munck, J.C., B.W. van Dijk, and H. Spekreijse, *Mathematical dipoles are adequate to describe realistic generators of human brain activity.* IEEE Trans Biomed Eng, 1988. **35**(11): p. 960-6.
67. He, B. and Z. Liu, *Multimodal Functional Neuroimaging: Integrating Functional MRI and EEG/MEG.* IEEE Rev Biomed Eng, 2008. **1**(2008): p. 23-40.
68. Dale, A.M., et al., *Dynamic statistical parametric mapping: combining fMRI and MEG for high-resolution imaging of cortical activity.* Neuron, 2000. **26**(1): p. 55-67.
69. Pascual-Marqui, R.D., *Standardized low-resolution brain electromagnetic tomography (sLORETA): technical details.* Methods Find Exp Clin Pharmacol, 2002. **24 Suppl D**: p. 5-12.
70. B. D. Van Veen , K.M.B., *Beamforming: A versatile approach to spatial filtering.* IEEE Acoustics, Speech and Signal Processing Magazine, 1988. **5**: p. 4-24.
71. Ogawa, S., et al., *Brain magnetic resonance imaging with contrast dependent on blood oxygenation.* Proc Natl Acad Sci U S A, 1990. **87**(24): p. 9868-72.
72. Friston, K.J., et al., *Characterizing dynamic brain responses with fMRI: a multivariate approach.* Neuroimage, 1995. **2**(2): p. 166-72.
73. Friston, K.J., et al., *Value-dependent selection in the brain: simulation in a synthetic neural model.* Neuroscience, 1994. **59**(2): p. 229-43.
74. Babiloni, F., et al., *Multimodal integration of high-resolution EEG and functional magnetic resonance imaging data: a simulation study.* Neuroimage, 2003. **19**(1): p. 1-15.

75. Liu, A.K., J.W. Belliveau, and A.M. Dale, *Spatiotemporal imaging of human brain activity using functional MRI constrained magnetoencephalography data: Monte Carlo simulations.* Proc Natl Acad Sci U S A, 1998. **95**(15): p. 8945-50.
76. Magistretti, P.J. and L. Pellerin, *Cellular mechanisms of brain energy metabolism and their relevance to functional brain imaging.* Philos Trans R Soc Lond B Biol Sci, 1999. **354**(1387): p. 1155-63.
77. Malonek, D. and A. Grinvald, *Interactions between electrical activity and cortical microcirculation revealed by imaging spectroscopy: implications for functional brain mapping.* Science, 1996. **272**(5261): p. 551-4.
78. Puce, A., et al., *Functional magnetic resonance imaging of sensory and motor cortex: comparison with electrophysiological localization.* J Neurosurg, 1995. **83**(2): p. 262-70.
79. Di Russo, F., et al., *Identification of the neural sources of the pattern-reversal VEP.* Neuroimage, 2005. **24**(3): p. 874-86.
80. Opitz, B., et al., *The functional neuroanatomy of novelty processing: integrating ERP and fMRI results.* Cereb Cortex, 1999. **9**(4): p. 379-91.
81. Lin, F.H., et al., *Spectral spatiotemporal imaging of cortical oscillations and interactions in the human brain.* Neuroimage, 2004. **23**(2): p. 582-95.
82. Babiloni, F., et al., *Estimation of the cortical functional connectivity with the multimodal integration of high-resolution EEG and fMRI data by directed transfer function.* Neuroimage, 2005. **24**(1): p. 118-31.
83. Astolfi, L., et al., *Estimation of the cortical connectivity by high-resolution EEG and structural equation modeling: simulations and application to finger tapping data.* IEEE Trans Biomed Eng, 2005. **52**(5): p. 757-68.
84. P.-J. Lahaye, S.B., J.-B. Poline, and L. Garnero, *Fusion of simultaneous fMRI/EEG data based on the electro-metabolic coupling.* Proc. IEEE ISBI, 2004: p. 864-867.
85. Esposito, F., C. Mulert, and R. Goebel, *Combined distributed source and single-trial EEG-fMRI modeling: application to effortful decision making processes.* Neuroimage, 2009. **47**(1): p. 112-21.
86. Ramon, C., P.H. Schimpf, and J. Haueisen, *Influence of head models on EEG simulations and inverse source localizations.* Biomed Eng Online, 2006. **5**: p. 10.
87. Wolters, C.H., et al., *Influence of tissue conductivity anisotropy on EEG/MEG field and return current computation in a realistic head model: a simulation and visualization study using high-resolution finite element modeling.* Neuroimage, 2006. **30**(3): p. 813-26.
88. Woolrich, M.W., et al., *Bayesian analysis of neuroimaging data in FSL.* Neuroimage, 2009. **45**(1 Suppl): p. S173-86.
89. Smith, S.M., et al., *Advances in functional and structural MR image analysis and implementation as FSL.* Neuroimage, 2004. **23 Suppl 1**: p. S208-19.
90. Smith, S.M., et al., *Tract-based spatial statistics: voxelwise analysis of multi-subject diffusion data.* Neuroimage, 2006. **31**(4): p. 1487-505.
91. Wang, Y., D.R. Haynor, and Y. Kim, *An investigation of the importance of myocardial anisotropy in finite-element modeling of the heart: methodology and application to the estimation of defibrillation efficacy.* IEEE Trans Biomed Eng, 2001. **48**(12): p. 1377-89.
92. Ollikainen, J.O., et al., *Effects of local skull inhomogeneities on EEG source estimation.* Med Eng Phys, 1999. **21**(3): p. 143-54.
93. Rush, S. and D.A. Driscoll, *Current distribution in the brain from surface electrodes.* Anesth Analg, 1968. **47**(6): p. 717-23.

94. Huiskamp, G., et al., *The need for correct realistic geometry in the inverse EEG problem.* IEEE Trans Biomed Eng, 1999. **46**(11): p. 1281-7.
95. Liu, Z., F. Kecman, and B. He, *Effects of fMRI-EEG mismatches in cortical current density estimation integrating fMRI and EEG: a simulation study.* Clin Neurophysiol, 2006. **117**(7): p. 1610-22.
96. Finke, S., R.M. Gulrajani, and J. Gotman, *Conventional and reciprocal approaches to the inverse dipole localization problem of electroencephalography.* IEEE Trans Biomed Eng, 2003. **50**(6): p. 657-66.
97. Crevecoeur, G., et al., *A hybrid algorithm for solving the EEG inverse problem from spatio-temporal EEG data.* Med Biol Eng Comput, 2008. **46**(8): p. 767-77.
98. Ramon, C., P.H. Schimpf, and J. Haueisen, *Effect of model complexity on EEG source localizations.* Neurol Clin Neurophysiol, 2004. **2004**: p. 81.
99. Wen, P. and K. Pope, *Realistic human head model for EEG from both the geometry and conductivity aspects.* Australas Phys Eng Sci Med, 2003. **26**(1): p. 1-5.
100. Zou, Q., et al., *Functional connectivity between the thalamus and visual cortex under eyes closed and eyes open conditions: a resting-state fMRI study.* Hum Brain Mapp, 2009. **30**(9): p. 3066-78.
101. Goebel, R., F. Esposito, and E. Formisano, *Analysis of functional image analysis contest (FIAC) data with brainvoyager QX: From single-subject to cortically aligned group general linear model analysis and self-organizing group independent component analysis.* Hum Brain Mapp, 2006. **27**(5): p. 392-401.
102. Esposito, F., et al., *Distributed analysis of simultaneous EEG-fMRI time-series: modeling and interpretation issues.* Magn Reson Imaging, 2009. **27**(8): p. 1120-30.
103. Chen, Y.S., et al., *Maximum contrast beamformer for electromagnetic mapping of brain activity.* IEEE Trans Biomed Eng, 2006. **53**(9): p. 1765-74.
104. Hauk, O., *Keep it simple: a case for using classical minimum norm estimation in the analysis of EEG and MEG data.* Neuroimage, 2004. **21**(4): p. 1612-21.
105. Barry, R.J., et al., *EEG differences between eyes-closed and eyes-open resting conditions.* Clin Neurophysiol, 2007. **118**(12): p. 2765-73.
106. Vatta, F., et al., *Comparison of realistic head modeling methods in EEG source imaging - biomed 2010.* Biomed Sci Instrum, 2010. **46**: p. 398-403.
107. Marx, E., et al., *Eyes open and eyes closed as rest conditions: impact on brain activation patterns.* Neuroimage, 2004. **21**(4): p. 1818-24.
108. Brookes, M.J., et al., *Simultaneous EEG source localisation and artifact rejection during concurrent fMRI by means of spatial filtering.* Neuroimage, 2008. **40**(3): p. 1090-104.

7 Figures

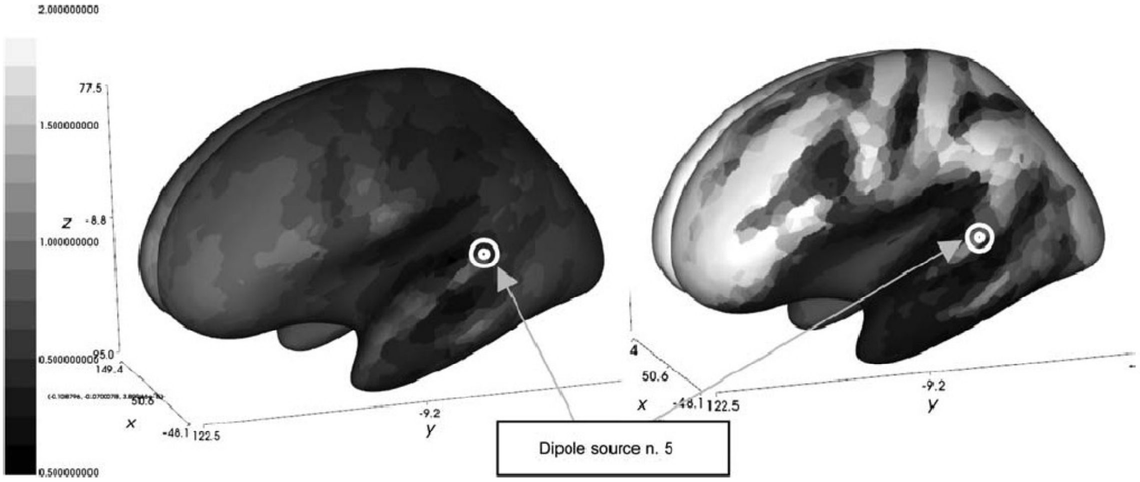

Figure 7-1PSF(rdm) inflated maps for dipole source n. 5, oriented along the y-axis (frontal to occipital).

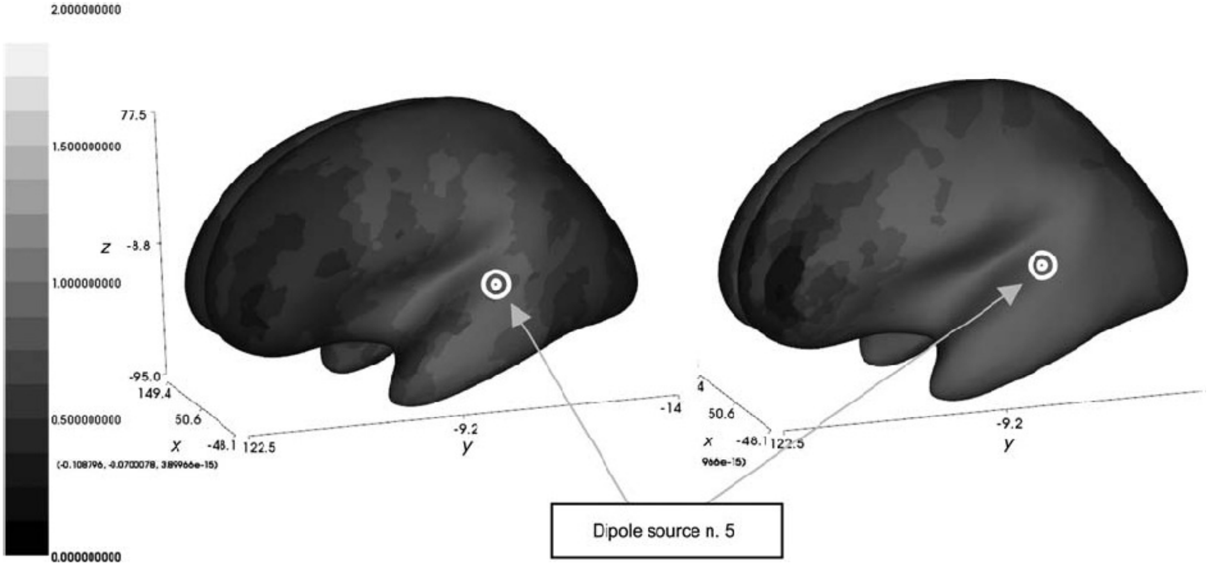

Figure 7-2PSF(corr) inflated map for dipole source n. 5, oriented along the y-axis (frontal to occipital).

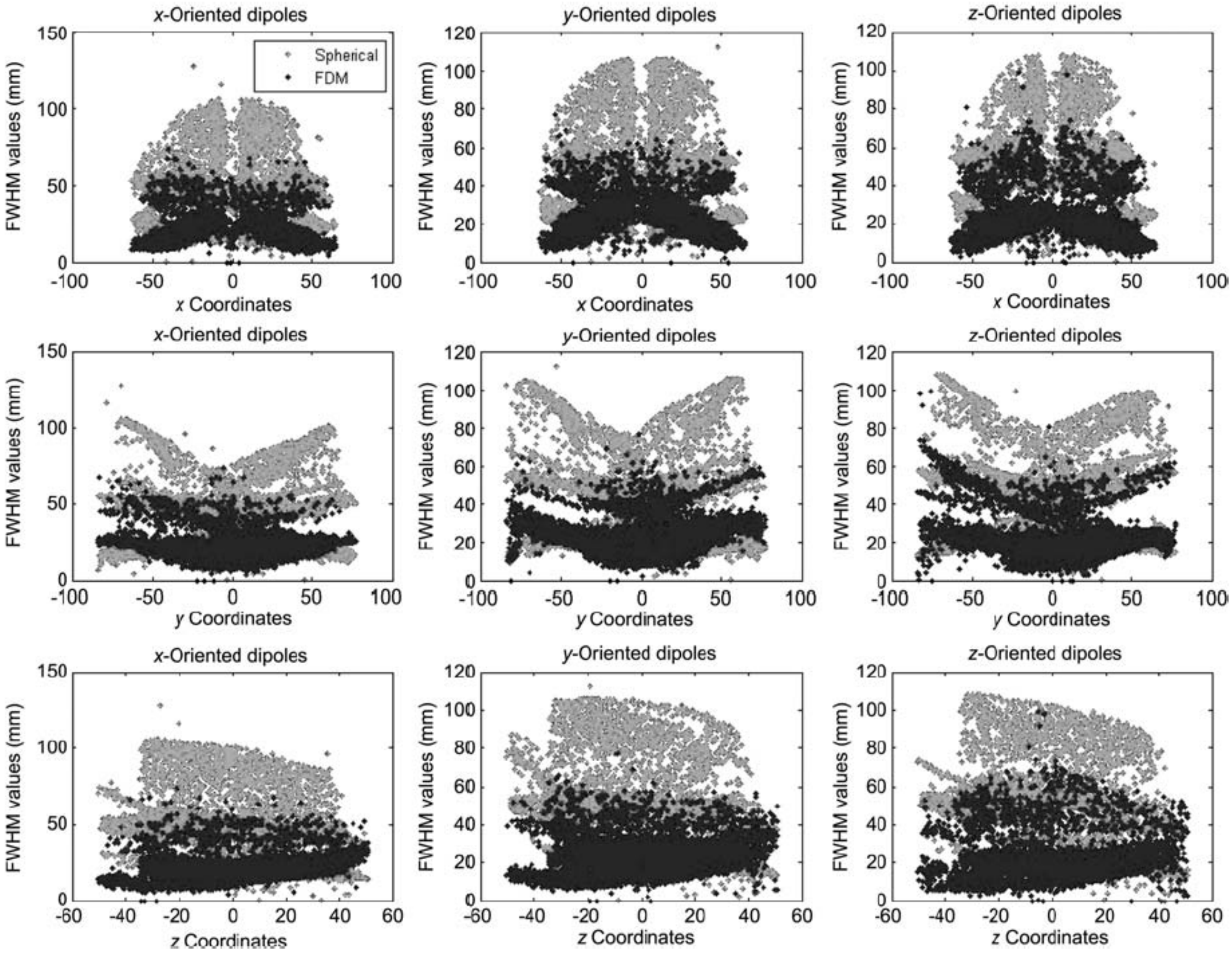

Figure 7-3FWHM values for PSF(rdm) computed over the whole cortex mesh, for the three different source orientations x, y and z, on the first, second and third columns, respectively. The reported values have also been arranged according to the dipole positions components x, y and z on the first, second and third rows. Black dots: realistic model. Grey dots: spherical model

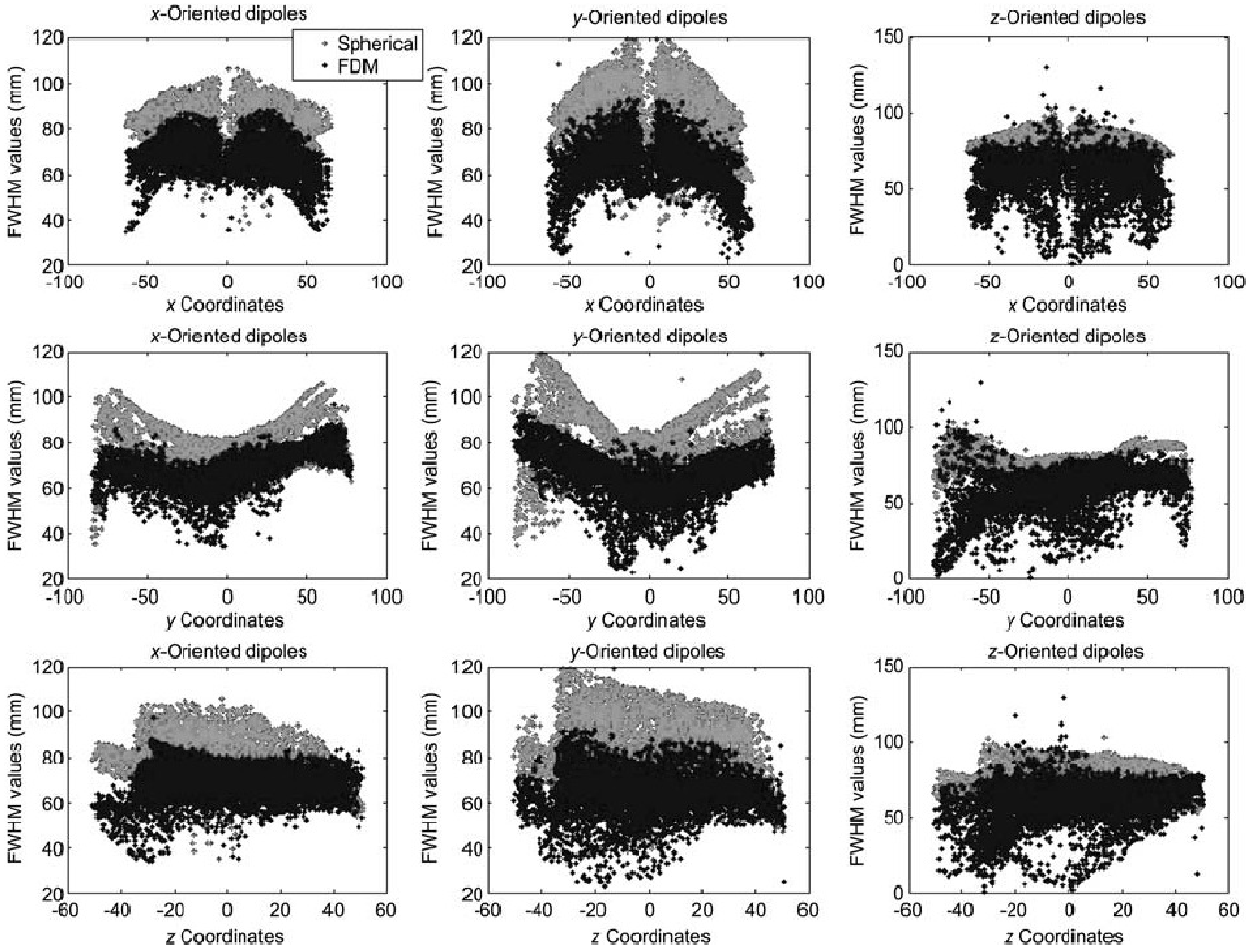

Figure 7-4FWHM values for PSF(corr) computed over the whole cortex mesh, for the three different source orientations x, y and z, on the first, second and third columns, respectively.The reported values have also been arranged according to the dipole positions components x, y and z on the first, second and third rows. Black dots: realistic model. Grey dots: spherical model.

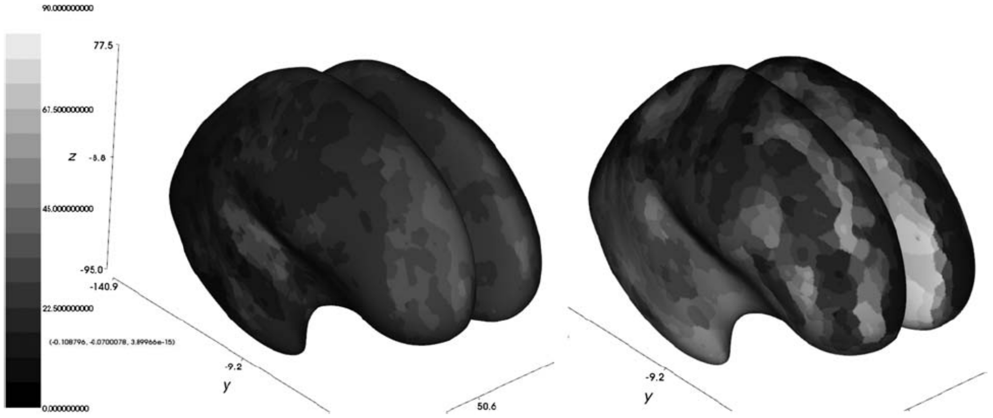

Figure 7-5 RMS inflated maps of the FWHM values for PSF(rdm). Realistic model (left) and spherical model (right).

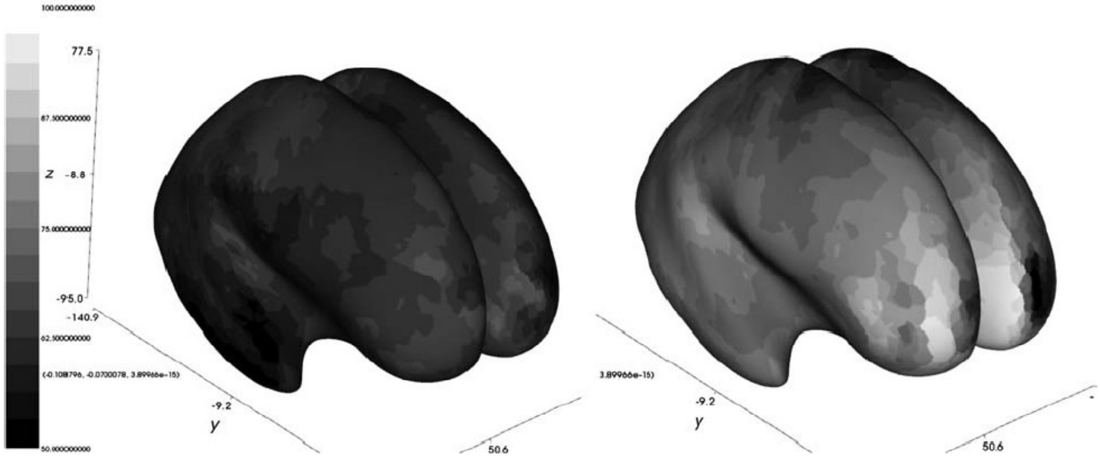

Figure 7-6 RMS inflated maps of the FWHM values for PSF(corr). Realistic model (left) and spherical model (right).

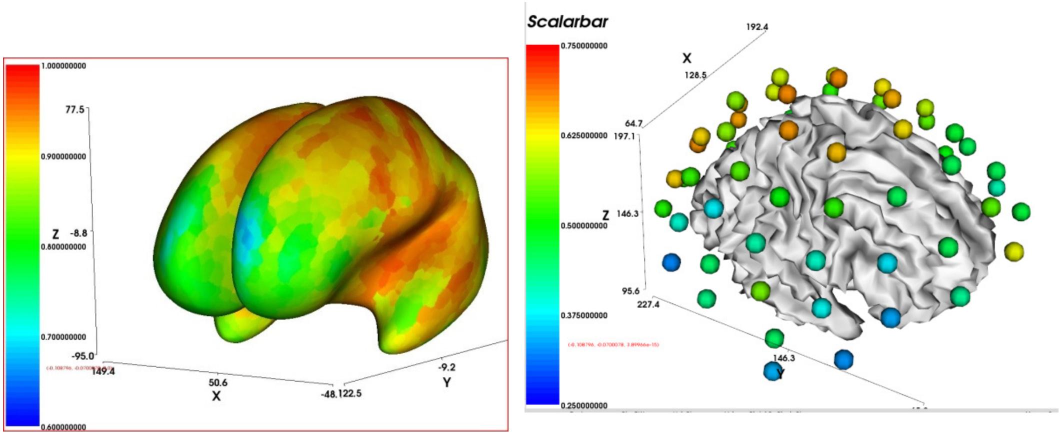

e

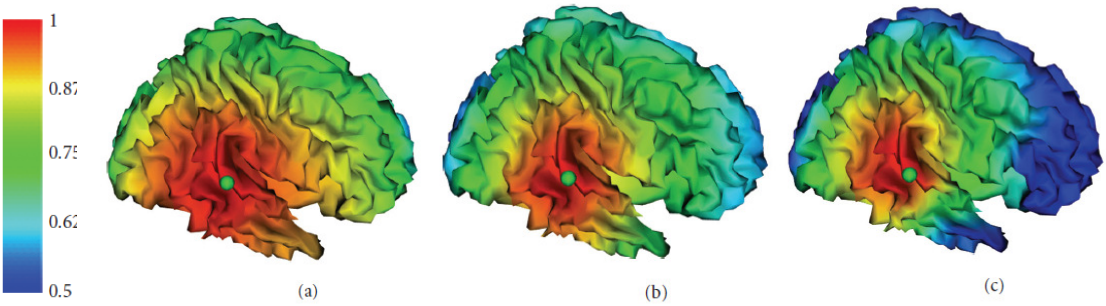

(a)

(b)

(c)

d source,

) FDM

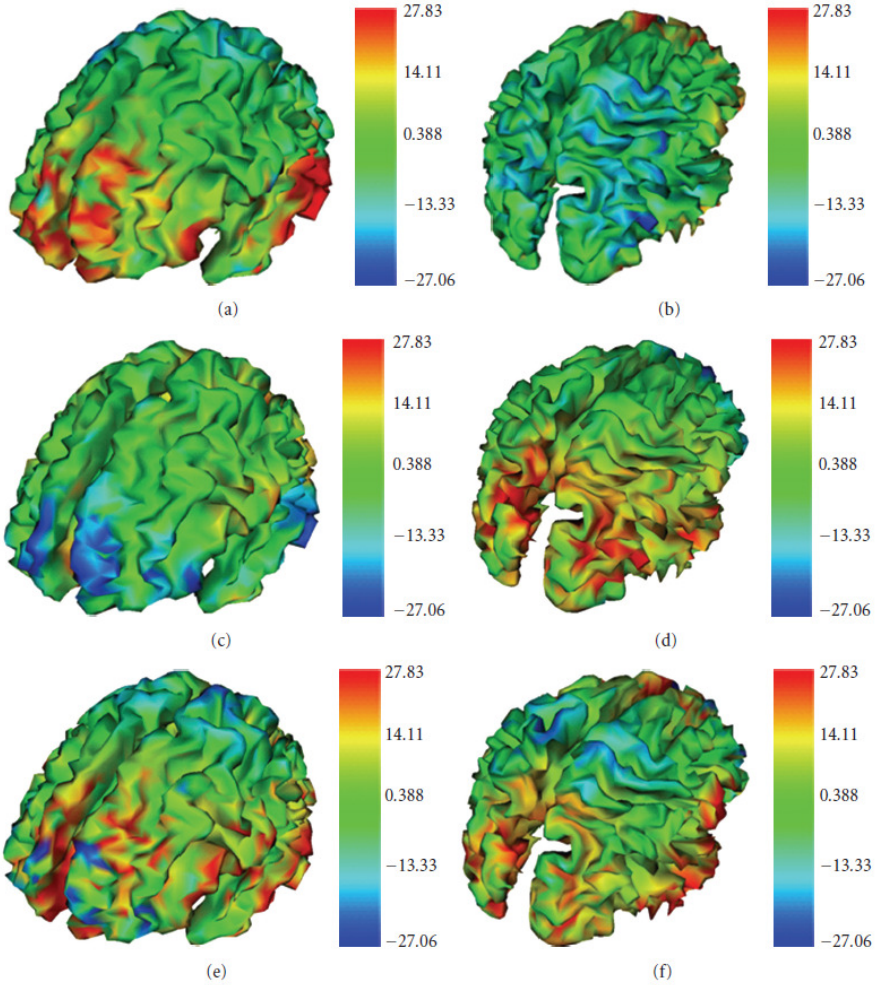

Figure 7-9 Differences between the FWHM values of the RMS PSF maps for the three couples of analyzed head models, computed as the difference between values of $FWHM_{Model1}$ and $FWHM_{Model2}$ over the cortex mesh ($FWHM_{Model1} - FWHM_{Model2}$). (A, B) $FWHM_{BEM} - FWHM_{FDM}$; (C, D) $FWHM_{SPH} - FWHM_{BEM}$; (E, F) $FWHM_{SPH} - FWHM_{FDM}$. Positive values in the computed $FWHM_{Model1} - FWHM_{Model2}$ differences are represented in red; negative values are represented in blue. Red zones correspond to a smaller spatial extent and hence to abetter capacity in terms of spatial discrimination of neural sources of Model 2 with respect to Model 1 for the different model pairs.

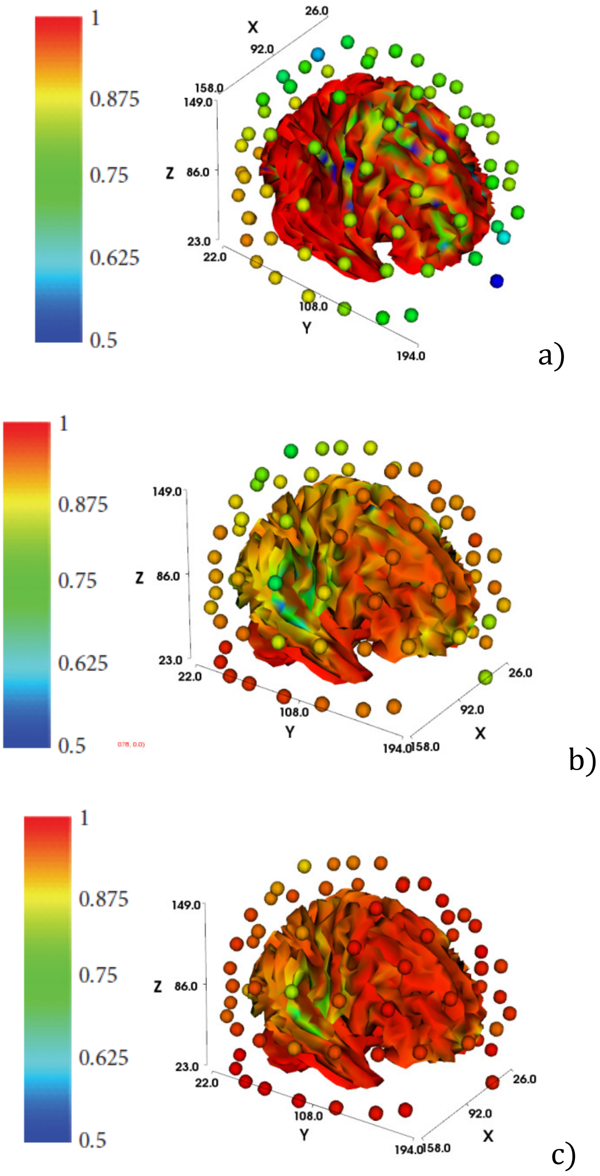

Figure 7-10 LeadField comparative analysis between isotropic model and: a)white matter anisotropy b) skull bones anisotropy c) white matter and skull bones anisotropy

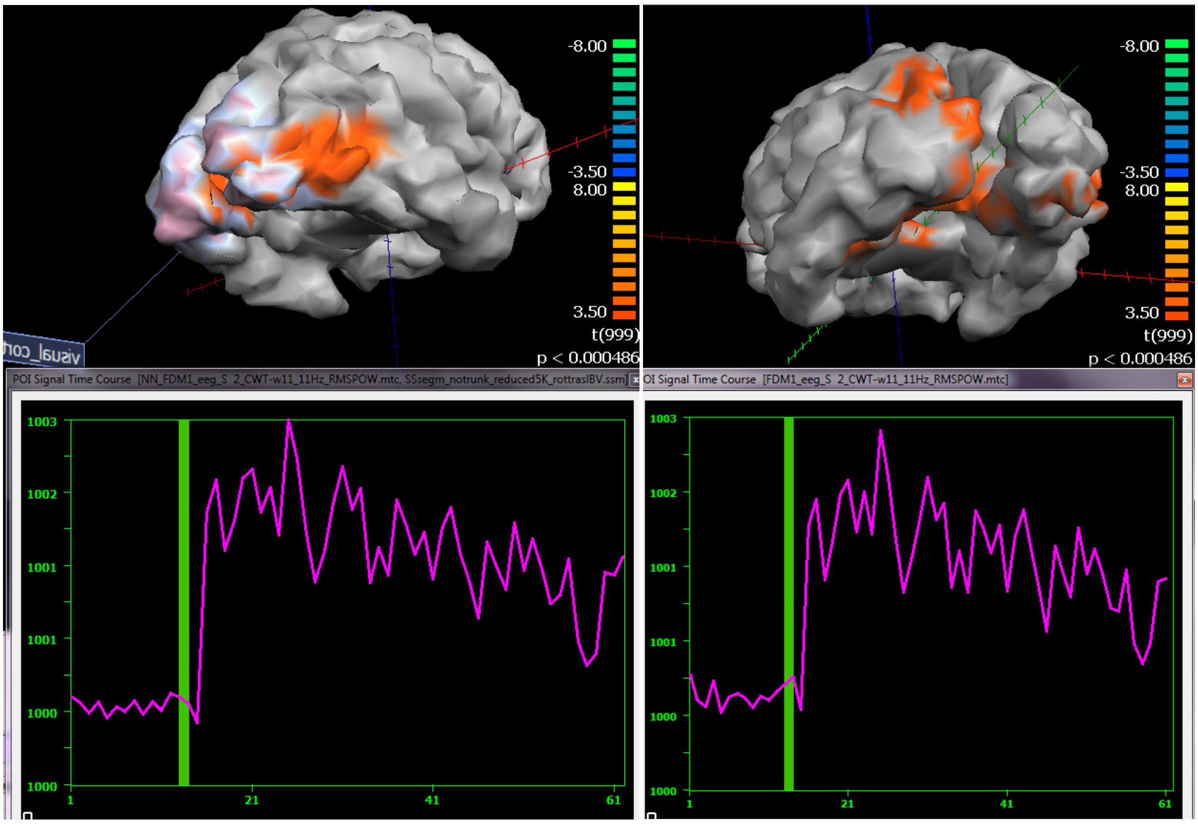
-8.00
-3.50
8.00
3.50
t(999)
p < 0.000486
visual_cort
POI Signal Time Course [NN_FDM1_eeg_S_2_CWT-w11_11Hz_RMSPOW.mtc, SSsegm_notrunk_reduced5K_rottraslBV.ssm]
1003
1002
1001
1001
1000
1000
1
21
41
61
-8.00
-3.50
8.00
3.50
t(999)
p < 0.000486
OI Signal Time Course [FDM1_eeg_S_2_CWT-w11_11Hz_RMSPOW.mtc]
1003
1002
1001
1001
1000
1000
1
21
41
61

a) *b)*

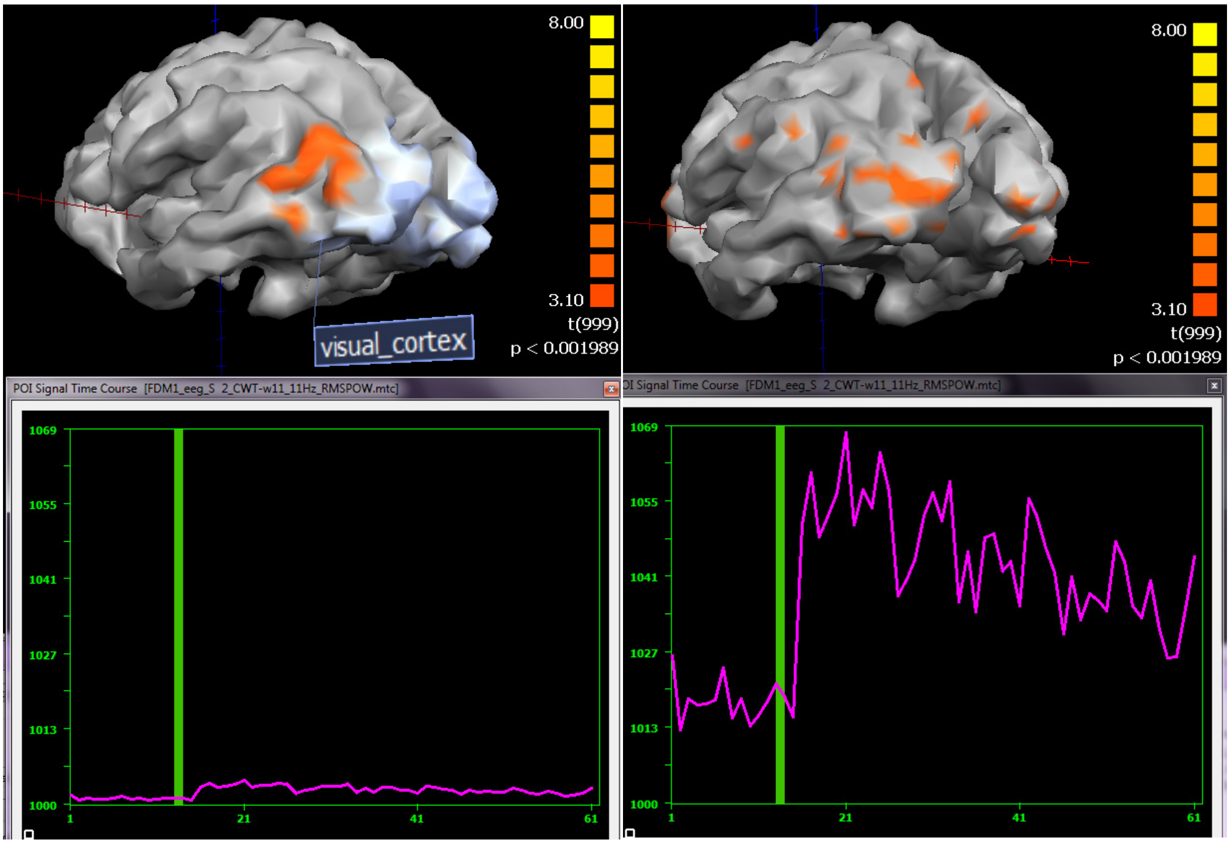

d) *c)*

Figure 7-11 EEG source imaging results: a) model: spherical, inverse: WMN. b)model: FDM, inverse: WMN. c) model:spherical, inverse: beamforming. d) model: realistic FDMl, inverse:beamforming

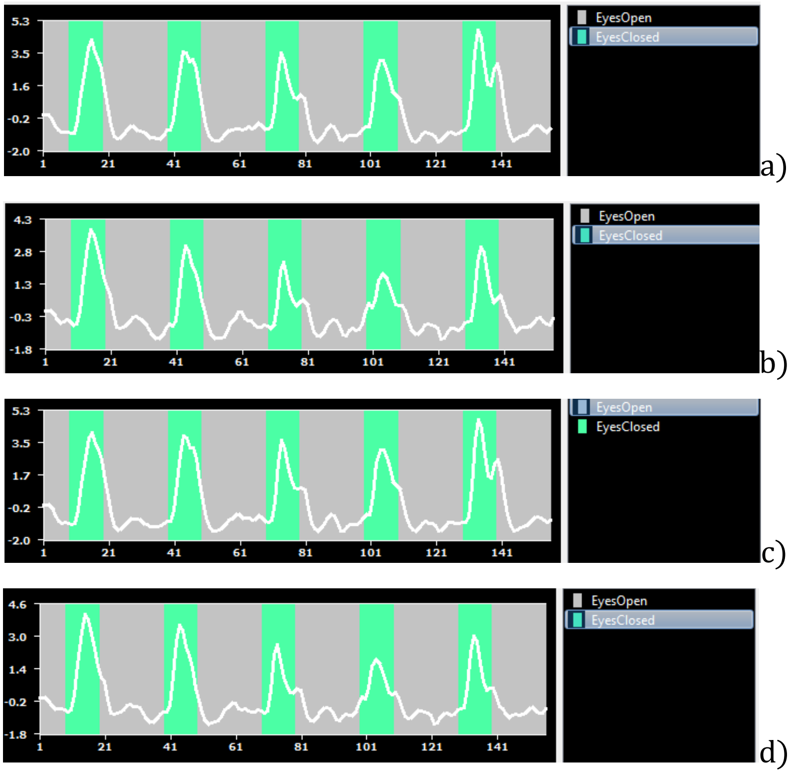

Figure 7-12 EEG- based fMRI predictors. a)model: realistic FDM, inverse: WMN; b)model: realistic FDM, inverse: beamformer; c) model: spherical, inverse: WMN, d) model: spherical, inverse: beamforming

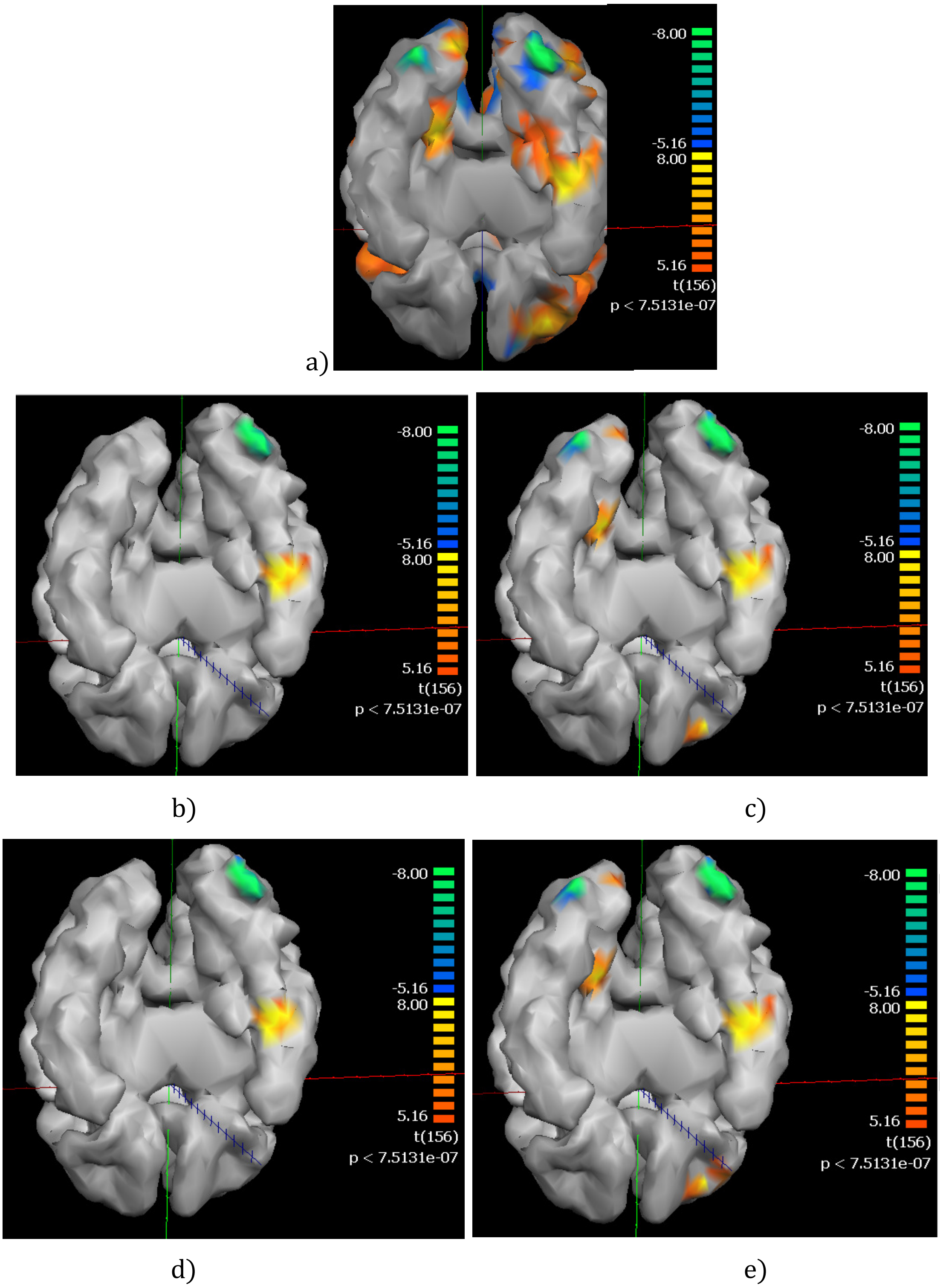

Figure 7-13 Statistical t-maps.resulting from EEG-fMRI coupling a) fMRI-only GLM analysis. b)model: realistic FDM, inverse: WMN; c)model: realistic FDM, inverse: beamformer; d) model: spherical, inverse: WMN, e) model: spherical, inverse: beamforming

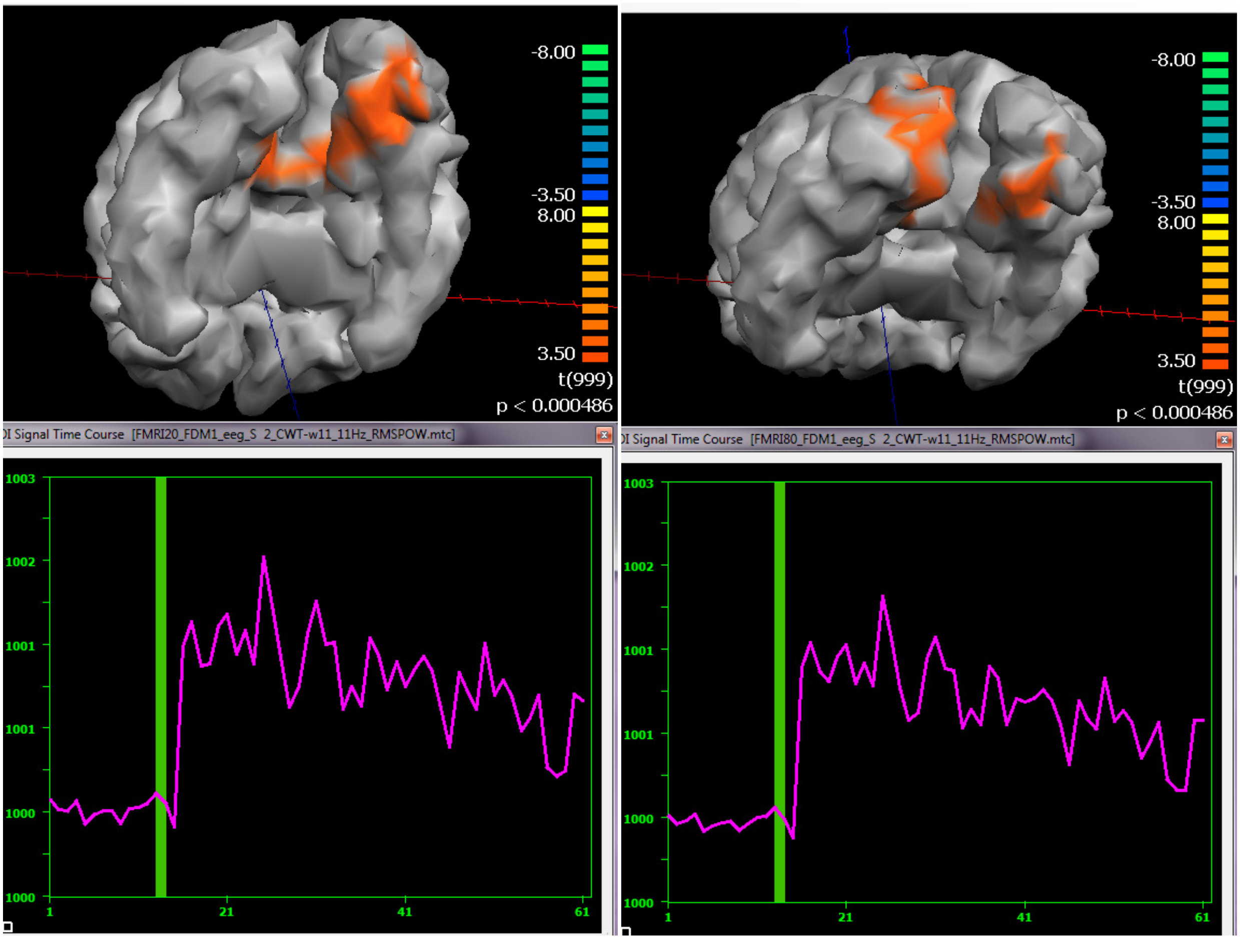
-8.00
-3.50
8.00
3.50
t(999)
p < 0.000486
)I Signal Time Course [FMRI20_FDM1_eeg_S 2_CWT-w11_11Hz_RMSPOW.mtc]
1003
1002
1001
1001
1000
1000
1
21
41
61
-8.00
-3.50
8.00
3.50
t(999)
p < 0.000486
)I Signal Time Course [FMRI80_FDM1_eeg_S 2_CWT-w11_11Hz_RMSPOW.mtc]
1003
1002
1001
1001
1000
1000
1
21
41
61

a) b)

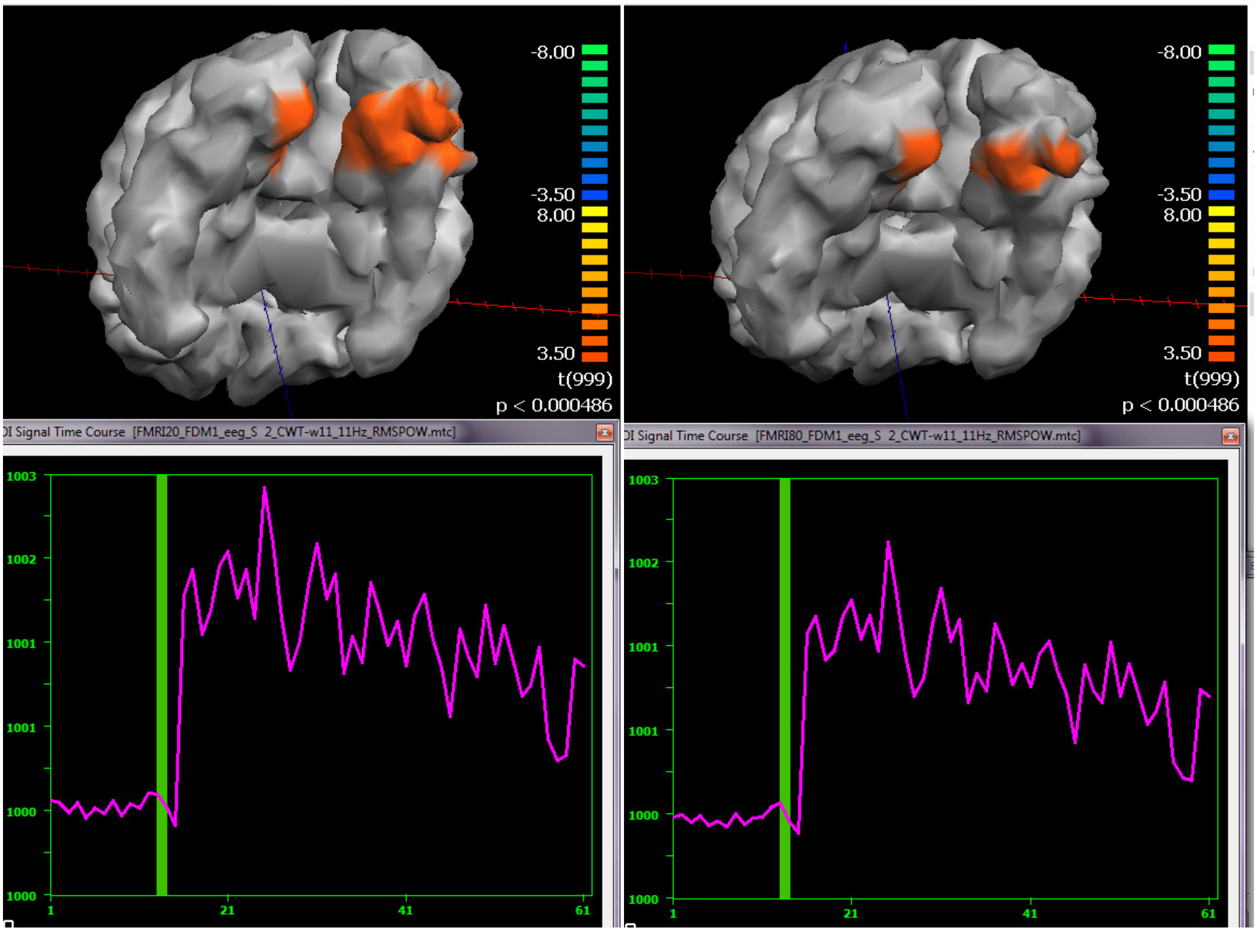

c) d)

Figure 7-14 t-maps resulting from EEG source analysis with fMRI weighting. a) realistic (FDM) model with fMRI weighting 20. b) realistic (FDM) model with fMRI weighting 80. c) spherical model with fMRI weighting 20. d) spherical model with weighting 80.

8 Tables

Sources	Mean FDM/SPH						Max FDM/SPH						FWHM (mm) FDM/SPH						SPH-FDM diff FWHM (mm)		
	x		y		z		x		y		z		x		y		z		x	y	z
	FDM	SPH	FDM	SPH	FDM	SPH	FDM	SPH	FDM	SPH	FDM	SPH	FDM	SPH	FDM	SPH	FDM	SPH	diff	diff	diff
1	79.97	97.06	77.64	90.18	78.46	95.16	523.50	359.49	258.68	327.80	418.74	445.70	23.3	23.9	14.0	49.0	26.1	52.8	0.6	35.0	26.7
2	78.54	114.72	80.50	118.75	86.51	128.55	199.98	413.05	177.61	494.52	300.37	681.60	8.4	35.5	5.4	18.9	31.5	20.1	27.1	13.5	-11.4
3	98.22	82.25	82.67	95.74	128.71	84.87	493.47	145.56	161.71	194.90	657.70	183.92	22.5	11.7	14.0	12.0	24.4	11.6	-10.8	-2.1	-12.8
4	101.46	93.49	82.87	96.41	135.72	89.71	467.61	151.92	145.16	194.91	755.96	175.24	18.5	7.9	10.6	9.7	28.0	10.8	-10.6	-0.9	-17.2
5	75.71	126.70	79.53	134.24	85.90	142.78	187.53	460.59	188.05	591.77	310.72	764.98	7.3	34.6	4.8	35.7	4.3	36.2	27.3	30.9	31.9
6	74.57	82.05	73.70	80.38	85.81	83.65	432.86	251.26	228.85	250.33	503.77	295.25	17.8	31.5	15.8	28.1	15.5	28.5	13.7	12.3	13.0
7	90.89	84.18	90.79	86.85	97.67	86.94	433.15	136.04	251.82	145.29	476.18	162.86	17.6	10.6	19.3	35.7	15.0	11.6	-7.0	16.4	-3.4
8	94.28	79.44	101.64	83.36	97.06	83.38	480.36	159.95	292.34	159.94	515.83	210.74	17.0	13.0	20.0	12.7	16.2	13.2	-4.0	-7.3	-3.0
9	91.09	87.26	82.87	95.80	113.55	90.56	569.39	282.08	240.94	375.57	684.98	418.90	16.5	38.8	18.2	35.2	17.5	85.1	22.3	17.0	67.6
10	93.68	90.23	79.74	99.14	99.44	93.24	591.23	307.11	247.99	404.77	549.58	446.86	15.5	54.7	18.0	82.0	16.0	42.3	39.2	64.0	26.3
11	79.19	97.56	77.53	95.33	86.32	94.16	521.88	346.10	266.14	384.77	504.67	433.28	17.3	12.7	19.1	32.8	18.5	11.3	-4.6	13.7	-7.2
12	80.46	82.37	78.73	83.24	93.92	83.22	522.16	247.95	258.70	274.96	534.53	281.64	19.5	37.6	18.0	10.6	17.2	11.2	18.1	-7.4	-6.0
13	82.01	99.18	82.48	93.06	81.05	103.48	504.31	375.18	268.98	368.75	460.74	531.97	15.2	35.1	16.1	86.8	13.2	79.3	19.9	70.7	66.1
14	83.39	102.42	81.31	94.69	79.11	106.13	547.80	393.93	270.38	372.07	443.27	557.37	15.0	34.3	15.1	35.2	15.9	42.5	19.3	20.1	26.6
15	81.61	102.92	81.75	94.91	76.11	102.56	542.20	394.29	285.86	368.20	373.31	520.02	12.4	54.7	11.0	37.7	14.9	38.2	42.3	26.7	23.3
16	69.10	150.24	77.56	139.30	78.59	149.75	353.14	590.95	257.30	634.56	445.17	813.46	11.0	62.0	10.3	35.6	10.1	47.1	51.0	25.3	37.0
17	80.67	176.84	81.81	215.17	124.64	219.54	300.49	658.12	246.58	979.40	602.43	1189.84	8.7	35.0	9.6	35.2	7.8	36.5	26.3	25.6	28.7
18	76.56	275.93	78.64	313.20	97.62	334.82	350.09	1049.63	234.51	1385.78	486.72	1777.55	8.0	31.5	5.6	32.1	6.2	33.1	23.5	26.5	26.9
19	72.68	135.75	77.26	135.50	85.90	133.92	394.75	517.06	253.24	616.80	502.53	720.33	11.8	28.7	9.3	36.8	9.3	30.2	16.9	27.5	20.9
20	74.51	106.19	79.26	104.99	87.05	103.76	432.94	391.71	254.01	439.92	494.86	511.42	12.1	15.4	10.0	15.2	10.4	16.1	3.3	5.2	5.7
21	82.86	130.39	88.39	128.53	91.77	147.19	503.64	507.76	282.24	565.09	541.05	811.35	11.1	39.9	13.2	42.0	11.0	41.7	28.8	28.8	30.7
22	79.94	146.21	87.99	142.72	98.50	160.64	438.88	575.20	284.83	645.78	559.82	886.40	10.0	40.6	12.0	42.6	8.4	41.8	30.6	30.6	33.4
23	80.84	84.73	74.66	80.84	84.14	87.21	504.90	293.59	224.58	273.59	500.39	377.65	17.5	29.9	20.2	29.6	21.0	30.1	12.4	9.4	9.1
24	80.36	78.22	82.29	76.51	83.29	81.35	487.29	246.25	283.19	224.99	467.37	310.08	17.3	34.4	22.7	22.9	17.5	34.9	17.1	0.2	17.4
25	93.52	82.19	82.99	92.48	149.86	86.68	519.70	219.37	233.86	315.02	885.94	355.56	16.5	37.6	19.2	35.7	20.3	39.4	21.1	16.5	19.1
26	94.67	81.36	87.31	90.76	124.46	83.27	479.78	158.86	252.73	229.60	684.28	244.28	15.2	10.4	18.1	37.8	16.1	38.4	-4.8	19.7	22.3

Table 8-1PSF(rdm)parameters

Sources	Mean FDM/SPH						Min FDM/SPH						FWHM (mm) FDM/SPH						SPH – FDM diff FWHM (mm)		
	x		y		z		x		y		z		x		y		z		x	y	z
	FDM	SPH	FDM	SPH	FDM	SPH	FDM	SPH	FDM	SPH	FDM	SPH	FDM	SPH	FDM	SPH	FDM	SPH	diff	diff	diff
1	0.76	0.82	0.74	0.83	0.65	0.71	0.40	0.42	0.38	0.28	-0.16	0.20	66.3	75.7	55.0	80.0	73.1	71.6	9.4	25.0	-1.5
2	0.66	0.75	0.61	0.78	0.52	0.65	0.26	0.30	0.23	0.29	0.00	0.17	68.2	81.1	59.0	82.4	61.2	80.2	12.9	23.4	19.0
3	0.57	0.69	0.55	0.46	0.46	0.49	0.23	0.31	0.11	0.06	-0.24	-0.07	65.0	97.6	77.2	54.8	92.5	73.9	32.6	-22.4	-18.6
4	0.51	0.46	0.55	0.44	0.52	0.35	0.21	0.23	0.11	0.08	-0.26	-0.11	60.1	41.9	81.5	40.4	105.7	54.5	-18.2	-41.1	-51.2
5	0.67	0.77	0.64	0.80	0.55	0.65	0.27	0.30	0.23	0.16	-0.26	0.14	63.0	78.4	58.7	79.4	57.3	73.8	15.4	20.7	16.5
6	0.75	0.80	0.74	0.82	0.64	0.70	0.37	0.39	0.37	0.24	-0.28	0.18	70.4	70.3	59.5	69.9	61.6	73.3	-0.1	10.4	11.7
7	0.60	0.66	0.58	0.62	0.52	0.44	0.23	0.24	0.17	-0.02	-0.12	-0.11	67.4	71.3	75.4	79.6	60.3	63.4	3.9	4.2	3.1
8	0.61	0.74	0.55	0.68	0.56	0.53	0.23	0.28	0.14	0.06	-0.14	-0.07	68.5	95.3	68.8	85.8	66.7	86.2	26.8	17.0	19.5
9	0.70	0.80	0.65	0.81	0.61	0.68	0.32	0.42	0.09	0.38	0.02	0.09	71.8	77.7	83.2	99.6	64.1	87.2	5.9	16.4	23.1
10	0.72	0.81	0.66	0.81	0.59	0.70	0.36	0.43	0.11	0.38	-0.22	0.13	68.3	80.7	72.5	96.1	67.5	80.1	12.4	23.6	12.6
11	0.77	0.80	0.75	0.83	0.65	0.69	0.38	0.46	0.32	0.39	-0.09	0.14	70.5	64.5	75.2	88.5	66.9	75.7	-6.0	13.3	8.8
12	0.76	0.79	0.72	0.81	0.60	0.66	0.44	0.44	0.26	0.38	-0.32	0.13	65.0	68.6	75.3	91.3	61.8	76.8	3.6	16.0	15.0
13	0.74	0.83	0.69	0.83	0.66	0.73	0.31	0.37	0.23	0.22	-0.16	0.13	72.2	90.6	66.9	100.4	63.2	86.9	18.4	33.5	23.7
14	0.75	0.83	0.70	0.83	0.66	0.73	0.33	0.38	0.23	0.23	-0.06	0.15	74.1	89.5	66.1	99.0	68.3	85.6	15.4	32.9	17.3
15	0.76	0.82	0.73	0.84	0.66	0.72	0.35	0.39	0.31	0.26	-0.01	0.19	72.1	82.5	63.0	87.1	70.5	77.8	10.4	24.1	7.3
16	0.76	0.83	0.74	0.85	0.66	0.73	0.38	0.38	0.33	0.26	-0.40	0.19	67.8	76.5	60.2	77.5	58.1	73.2	8.7	17.3	15.1
17	0.63	0.77	0.70	0.83	0.47	0.63	0.31	0.32	0.27	0.28	-0.11	0.18	50.9	78.9	62.7	68.5	63.0	74.2	28.0	5.8	11.2
18	0.68	0.78	0.70	0.83	0.53	0.67	0.32	0.34	0.33	0.30	-0.02	0.22	60.2	75.1	58.4	79.3	58.2	73.7	14.9	20.9	15.5
19	0.74	0.82	0.73	0.83	0.66	0.71	0.40	0.39	0.31	0.36	-0.28	0.18	58.3	79.4	70.3	82.1	60.4	74.3	21.1	11.8	13.9
20	0.74	0.80	0.72	0.82	0.64	0.68	0.34	0.40	0.29	0.36	0.02	0.14	64.6	80.0	71.2	81.6	65.8	76.2	15.4	10.4	10.4
21	0.72	0.80	0.65	0.82	0.63	0.68	0.29	0.34	0.08	0.28	-0.06	0.13	73.7	89.7	64.1	98.7	68.7	83.4	16.0	34.6	14.7
22	0.72	0.82	0.68	0.83	0.63	0.69	0.30	0.35	0.15	0.19	-0.08	0.12	71.8	87.6	66.8	95.2	58.4	82.0	15.8	28.4	23.6
23	0.75	0.83	0.71	0.84	0.65	0.74	0.39	0.39	0.23	0.22	-0.26	0.16	71.1	85.6	65.9	95.6	69.6	84.0	14.5	29.7	14.4
24	0.73	0.82	0.73	0.83	0.63	0.73	0.34	0.39	0.32	0.18	-0.17	0.15	69.2	88.2	71.4	98.3	66.1	84.6	19.0	26.9	18.5
25	0.64	0.77	0.64	0.76	0.57	0.62	0.24	0.39	0.11	0.34	-0.01	0.05	69.1	96.3	79.5	81.5	71.2	81.0	27.2	2.0	9.8
26	0.60	0.72	0.59	0.64	0.52	0.55	0.27	0.35	-0.05	0.23	-0.33	0.00	62.0	89.3	68.1	63.7	60.4	76.5	27.3	-4.4	16.1

Table 8-2PSF(corr) parameters

	Mean PSF											
	x			y			z			RMS		
	FDM	BEM	SPH	FDM	BEM	SPH	FDM	BEM	SPH	FDM	BEM	SPH
1	0.76	0.74	0.82	0.74	0.76	0.83	0.65	0.75	0.71	0.71	0.75	0.79
2	0.66	0.67	0.75	0.61	0.64	0.78	0.52	0.77	0.65	0.58	0.70	0.73
3	0.57	0.66	0.69	0.55	0.57	0.46	0.46	0.80	0.49	0.48	0.69	0.56
4	0.51	0.61	0.46	0.55	0.56	0.44	0.52	0.78	0.35	0.47	0.66	0.42
5	0.67	0.71	0.77	0.64	0.71	0.8	0.55	0.80	0.65	0.60	0.74	0.74
6	0.75	0.74	0.8	0.74	0.74	0.82	0.64	0.77	0.7	0.70	0.75	0.78
7	0.6	0.57	0.66	0.58	0.63	0.62	0.52	0.69	0.44	0.56	0.64	0.58
8	0.61	0.56	0.74	0.55	0.62	0.68	0.56	0.70	0.53	0.57	0.63	0.66
9	0.7	0.73	0.8	0.65	0.65	0.81	0.61	0.78	0.68	0.64	0.72	0.77
10	0.72	0.71	0.81	0.66	0.69	0.81	0.59	0.81	0.7	0.64	0.74	0.78
11	0.77	0.75	0.8	0.75	0.76	0.83	0.65	0.79	0.69	0.71	0.77	0.78
12	0.76	0.73	0.79	0.72	0.74	0.81	0.6	0.81	0.66	0.70	0.76	0.76
13	0.74	0.72	0.83	0.69	0.72	0.83	0.66	0.81	0.73	0.69	0.75	0.80
14	0.75	0.69	0.83	0.7	0.72	0.83	0.66	0.78	0.73	0.69	0.74	0.80
15	0.76	0.72	0.82	0.73	0.74	0.84	0.66	0.78	0.72	0.70	0.75	0.80
16	0.76	0.76	0.83	0.74	0.77	0.85	0.66	0.83	0.73	0.70	0.79	0.81
17	0.63	0.72	0.77	0.7	0.54	0.83	0.47	0.81	0.63	0.58	0.70	0.75
18	0.68	0.74	0.78	0.7	0.57	0.83	0.53	0.81	0.67	0.62	0.72	0.76
19	0.74	0.74	0.82	0.73	0.75	0.83	0.66	0.82	0.71	0.70	0.77	0.79
20	0.74	0.75	0.8	0.72	0.71	0.82	0.64	0.74	0.68	0.69	0.73	0.77
21	0.72	0.68	0.8	0.65	0.70	0.82	0.63	0.80	0.68	0.65	0.73	0.77
22	0.72	0.72	0.82	0.68	0.70	0.83	0.63	0.80	0.69	0.66	0.75	0.79
23	0.75	0.72	0.83	0.71	0.74	0.84	0.65	0.79	0.74	0.68	0.76	0.80
24	0.73	0.66	0.82	0.73	0.74	0.83	0.63	0.77	0.73	0.68	0.73	0.80
25	0.64	0.70	0.77	0.64	0.64	0.76	0.57	0.70	0.62	0.59	0.68	0.73
26	0.6	0.64	0.72	0.59	0.65	0.64	0.52	0.77	0.55	0.55	0.69	0.64
Mean	0.69	0.70	0.77	0.67	0.68	0.77	0.59	0.78	0.65	0.64	0.72	0.74
± SD	± 0.07	± 0.05	± 0.08	± 0.07	± 0.07	± 0.11	± 0.06	± 0.04	± 0.10	± 0.07	± 0.04	± 0.09

Table 8-3Summary of the mean PSF values for the realistic (BEM and FDM) and the sensor-fitted spherical (SPH) models, for sources 1÷26 parallel to x, y, and z orientations and for the RMS maps.

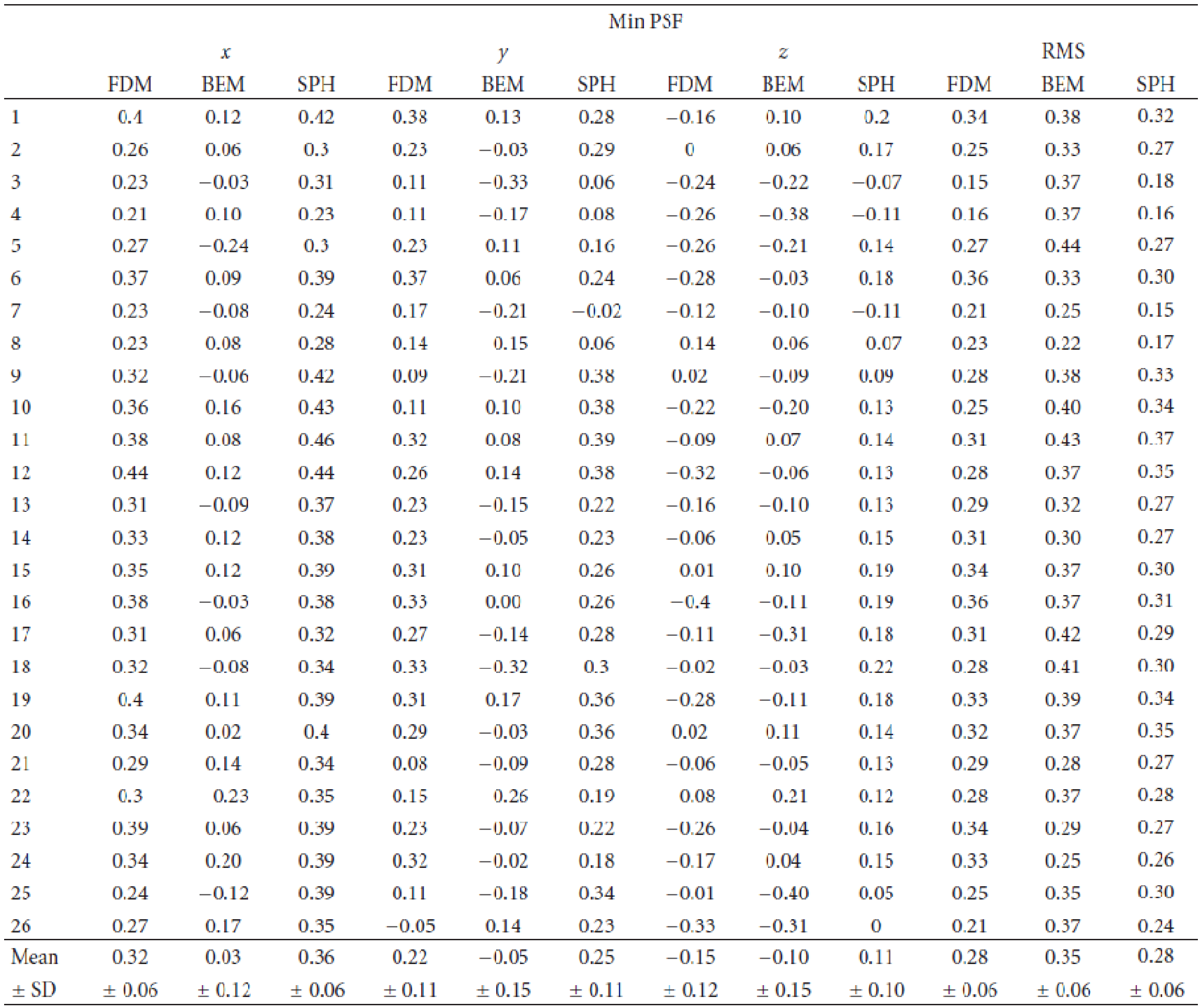

	Min PSF											
	x			*y*			*z*			RMS		
	FDM	BEM	SPH	FDM	BEM	SPH	FDM	BEM	SPH	FDM	BEM	SPH
1	0.4	0.12	0.42	0.38	0.13	0.28	−0.16	0.10	0.2	0.34	0.38	0.32
2	0.26	0.06	0.3	0.23	−0.03	0.29	0	0.06	0.17	0.25	0.33	0.27
3	0.23	−0.03	0.31	0.11	−0.33	0.06	−0.24	−0.22	−0.07	0.15	0.37	0.18
4	0.21	0.10	0.23	0.11	−0.17	0.08	−0.26	−0.38	−0.11	0.16	0.37	0.16
5	0.27	−0.24	0.3	0.23	0.11	0.16	−0.26	−0.21	0.14	0.27	0.44	0.27
6	0.37	0.09	0.39	0.37	0.06	0.24	−0.28	−0.03	0.18	0.36	0.33	0.30
7	0.23	−0.08	0.24	0.17	−0.21	−0.02	−0.12	−0.10	−0.11	0.21	0.25	0.15
8	0.23	0.08	0.28	0.14	0.15	0.06	0.14	0.06	0.07	0.23	0.22	0.17
9	0.32	−0.06	0.42	0.09	−0.21	0.38	0.02	−0.09	0.09	0.28	0.38	0.33
10	0.36	0.16	0.43	0.11	0.10	0.38	−0.22	−0.20	0.13	0.25	0.40	0.34
11	0.38	0.08	0.46	0.32	0.08	0.39	−0.09	0.07	0.14	0.31	0.43	0.37
12	0.44	0.12	0.44	0.26	0.14	0.38	−0.32	−0.06	0.13	0.28	0.37	0.35
13	0.31	−0.09	0.37	0.23	−0.15	0.22	−0.16	−0.10	0.13	0.29	0.32	0.27
14	0.33	0.12	0.38	0.23	−0.05	0.23	−0.06	0.05	0.15	0.31	0.30	0.27
15	0.35	0.12	0.39	0.31	0.10	0.26	0.01	0.10	0.19	0.34	0.37	0.30
16	0.38	−0.03	0.38	0.33	0.00	0.26	−0.4	−0.11	0.19	0.36	0.37	0.31
17	0.31	0.06	0.32	0.27	−0.14	0.28	−0.11	−0.31	0.18	0.31	0.42	0.29
18	0.32	−0.08	0.34	0.33	−0.32	0.3	−0.02	−0.03	0.22	0.28	0.41	0.30
19	0.4	0.11	0.39	0.31	0.17	0.36	−0.28	−0.11	0.18	0.33	0.39	0.34
20	0.34	0.02	0.4	0.29	−0.03	0.36	0.02	0.11	0.14	0.32	0.37	0.35
21	0.29	0.14	0.34	0.08	−0.09	0.28	−0.06	−0.05	0.13	0.29	0.28	0.27
22	0.3	0.23	0.35	0.15	0.26	0.19	0.08	0.21	0.12	0.28	0.37	0.28
23	0.39	0.06	0.39	0.23	−0.07	0.22	−0.26	−0.04	0.16	0.34	0.29	0.27
24	0.34	0.20	0.39	0.32	−0.02	0.18	−0.17	0.04	0.15	0.33	0.25	0.26
25	0.24	−0.12	0.39	0.11	−0.18	0.34	−0.01	−0.40	0.05	0.25	0.35	0.30
26	0.27	0.17	0.35	−0.05	0.14	0.23	−0.33	−0.31	0	0.21	0.37	0.24
Mean	0.32	0.03	0.36	0.22	−0.05	0.25	−0.15	−0.10	0.11	0.28	0.35	0.28
± SD	± 0.06	± 0.12	± 0.06	± 0.11	± 0.15	± 0.11	± 0.12	± 0.15	± 0.10	± 0.06	± 0.06	± 0.06

Table 8-4Summary of the minimum PSF values for the realistic (BEM and FDM) and the sensor-fitted spherical (SPH) models, for sources 1÷26 parallel to x, y and z orientations and for the RMS maps.

	FWHM											
	x			*y*			*z*			RMS		
	FDM	BEM	SPH	FDM	BEM	SPH	FDM	BEM	SPH	FDM	BEM	SPH
1	66.3	57.7	75.7	55	73.7	80	73.1	61.8	71.6	72.23	61.38	68.81
2	68.2	54.1	81.1	59	76.8	82.4	61.2	81.1	80.2	62.20	54.62	80.19
3	65	97.6	97.6	77.2	70.3	54.8	92.5	114.4	73.9	69.90	100.41	66.67
4	60.1	87.5	41.9	81.5	72.1	40.4	105.7	109.3	54.5	72.49	78.09	46.02
5	63	77.5	78.4	58.7	77.6	79.4	57.3	83.0	73.8	57.89	78.81	77.27
6	70.4	59.9	70.3	59.5	78.7	69.9	61.6	54.1	73.3	65.92	62.26	67.84
7	67.4	57.4	71.3	75.4	91.5	79.6	60.3	63.6	63.4	69.29	65.59	68.98
8	68.5	61.9	95.3	68.8	90.5	85.8	66.7	60.0	86.2	84.33	63.71	77.90
9	71.8	89.0	77.7	83.2	85.3	99.6	64.1	76.8	87.2	85.64	71.69	80.72
10	68.3	86.6	80.7	72.5	84.0	96.1	67.5	90.3	80.1	83.16	73.22	82.23
11	70.5	71.4	64.5	75.2	78.5	88.5	66.9	82.4	75.7	77.09	69.65	69.81
12	65	79.6	68.6	75.3	79.3	91.3	61.8	60.9	76.8	77.88	71.24	66.83
13	72.2	49.6	90.6	66.9	76.0	100.4	63.2	90.3	86.9	68.47	86.60	94.13
14	74.1	58.9	89.5	66.1	83.2	99.0	68.3	59.4	85.6	81.90	61.44	91.65
15	72.1	58.4	82.5	63	78.3	87.1	70.5	63.1	77.8	78.16	61.56	81.94
16	67.8	62.0	76.5	60.2	78.4	77.5	58.1	77.6	73.2	75.18	63.60	76.06
17	50.9	89.3	78.9	62.7	33.7	68.5	63	84.0	74.2	51.55	82.72	67.74
18	60.2	74.4	75.1	58.4	70.1	79.3	58.2	77.6	73.7	56.99	74.41	75.06
19	58.3	67.2	79.4	70.3	75.9	82.1	60.4	78.8	74.3	63.52	77.17	78.88
20	64.6	78.8	80	71.2	77.1	81.6	65.8	78.5	76.2	76.17	72.64	79.15
21	73.7	64.0	89.7	64.1	86.2	98.7	68.7	89.9	83.4	68.56	60.98	88.92
22	71.8	52.5	87.6	66.8	85.6	95.2	58.4	87.7	82	67.03	85.39	87.55
23	71.1	58.8	85.6	65.9	80.1	95.6	69.6	86.1	84	79.21	63.48	89.28
24	69.2	79.1	88.2	71.4	81.9	98.3	66.1	58.2	84.6	69.02	63.07	88.12
25	69.1	92.1	96.3	79.5	66.8	81.5	71.2	69.4	81	69.41	73.55	93.01
26	62.0	79.0	89.3	68.1	66.1	63.7	60.4	97.2	76.5	61.55	76.10	73.57
Mean	67.0	70.9	80.5	68.3	76.8	82.9	66.9	78.3	77.3	71.0	71.3	77.6
± SD	± 5.4	± 14.0	± 11.7	± 7.7	± 10.9	± 14.6	± 10.6	± 15.6	± 7.4	± 8.8	± 10.3	± 10.8

Table 8-5Summary of the FWHM PSF values for the realistic (BEM and FDM) and the sensor-fitted spherical (SPH) models, for sources 1÷26 parallel to x, y and z orientations and for the RMS maps.